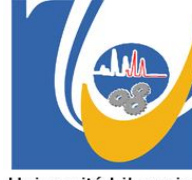**University of Genova**

DITEN

Université Libanaise

École Doctorale
Sciences et Technologies

CO-SUPERVISION THESIS

FOR THE DEGREE OF DOCTOR

UNIVERSITY OF GENOVA (DITEN) – ITALY

&

LEBANESE UNIVERSITY (EDST) – LEBANON

SPECIALTY : Science and Technology for Electronic and Telecommunication Engineering

TITLE:

Wind Energy Harvester Interface for Sensor Nodes

PRESENTED AND DEFENDED BY

Mohamad Haidar

25 February 2021

Acknowlodgemnt

List of Tables

List of Figures

Abstract

The research topic is developping a power converting interface for the novel FLEHAP wind energy harvester allowing the produced energy to be used for powering small wireless nodes. The harvester's electrical characteristics were studied and a strategy was developed to control and mainting a maximum power transfer. The electronic power converter interface was designed, containing an AC/DC Buck-Boost converter and controlled with a low power microcontroller. Different prototypes were developped that evolved by reducing the sources of power loss and rendering the system more efficient. The validation of the system was done through simulations in the COSMIC/DITEN lab using generated signals, and then follow-up experiments were conducted with a controllable wind tunnel in the DIFI department University of Genoa. The experiment results proved the functionality of the control algorithm as well as the efficiency that was ramped up by the hardware solutions that were implemented, and generally met the requirement to provide a power source for low-power sensor nodes.

Keywords: Energy harvesting; WSN; IoT; power converters; MPPT; MCU.

Table of Content

Chapter 1. Introduction

This research falls within the sensor networks domain in the wide picture. Where many challenges, applications and opportunities are present and can be studied. In this introduction, the description and importance of this domain is discussed, highlighting the key aspects that fall within the scope and the interest of this research.

To begin with, the objectives and structure of this thesis is presented.

1.1. Objectives and structure

This thesis compromises the research to develop a power converting interface for the novel FLEHAP wind energy harvester, which is the main contribution of this thesis work,   as a power source for sensor nodes. The objectives of the research are:

- Designing a power transfer system that is able to interface the novel energy harvester and meet the sensor node requirements.
- Optimizing the power transfer with an accurate, fast and stable MPPT control algorithm.
- Reducing the power loss in the system to ensure a high efficiency performance.
- Implementing and testing the proposed concepts and methods to test and validate the system.

To meet these objectives, I have used the following methodology: 1- study the literature review and the state of the art; 2- software used…; 3- hardware used ….; 4-conclusion and future work…

In order to show that clearly, the thesis is organized as follows: Chapter 1 provides an introduction and description of the target application as well as the energy harvesting methods that are available. Chapter 2 discusses the DC/DC converters that are commonly used in such systems, providing study and simulation results. Chapter 3 discusses the control MPPT algorithms that are used in the literature and showcases the proposed algorithm that is developed

for this problem. Chapter 4 shows implementation issues regarding the power monitoring in the MPPT algorithm, with solutions to deal with these issues. Chapter 5 describes the proposed system and the developed prototypes that were tested and validated to ensure the viability of the proposal. Conclusion are drawn in chapter 6.

1.2.   WSN and IoT

Wireless sensor networks have gained considerable popularity due to their flexibility in solving problems in different application domains and have the potential to change our lives in many different ways. And they continue to attract a lot of attention from the academia and industry among researchers, industrials, equipment and chip manufacturers and service providers for promoting large-scale deployments in many application domains[1]–[7], such as:

- Military applications: Wireless sensor networks will be likely an integral part of military command, control, communications, computing, intelligence, battlefield surveillance, reconnaissance and targeting systems. Especially with the increase of use of Unmanned Armed Vehicles UAVs and the shift towards automation in various operation fields.

- Area monitoring: It is one of the most common applications of WSN around the world, where he sensor nodes are deployed over a region where some phenomenon is to be monitored. When the sensors detect the event being monitored (heat, pressure etc), the event is reported to one of the base stations, which then takes appropriate action.

- Transportation: Real-time traffic information is collected by WSNs to later feed transportation models and alert drivers of congestion and traffic problems. And this is one example of a large-scale domestic use of the WSN.

- Health applications: Some of the health applications for sensor networks are supporting interfaces for the disabled, integrated patient monitoring, diagnostics, and drug administration in hospitals, tele-monitoring of human physiological data, and tracking & monitoring doctors or patients inside a hospital.

- Environmental sensing: The term Environmental Sensor Networks has developed to cover many applications of WSNs to earth science research. This includes sensing volcanoes, oceans, glaciers, forests etc.

- Structural monitoring: Wireless sensors can be utilized to monitor the movement within buildings and infrastructure such as bridges, flyovers, embankments, tunnels etc enabling Engineering practices to monitor assets remotely without the need for costly site visits.

- Industrial monitoring: Wireless sensor networks have been developed for machinery condition-based maintenance (CBM) as they offer significant cost savings and enable new functionalities. In wired systems, the installation of enough sensors is often limited by the cost of wiring.

- Agricultural sector: using a wireless network frees the farmer from the maintenance of wiring in a difficult environment. Irrigation automation enables more efficient water use and reduces waste.

In the other hand, Internet of Things (IoT) is a promising research topic with prosperous industrial trend. In addition to the basic idea of bringing things or objects into the Internet, there are various approaches that are based on WSN. With the advancement in wearable devices industry, the increasing potential of smart homes and environments and the continuous requirement for personalization and context-aware applications, WSNs enter a new technological era and contribute to several new sensing products and applications (e.g. body sensors for medical surveillance, wireless visual sensors for environmental monitoring, WSNs in smart roads for intelligent traffic management and roads safety, wireless sensors in wearable devices, speed and motion sensors in personal devices, light and noise sensors in smart phones and tablets). In parallel, WSN will be used in the wider context of IoT. Thus, new architectures spanning the interactions between cloud services, smart devices and distributed sensors are evolving, which enable new business models and deployments of sensors to enhance user benefit. While continuous improvements are addressing specific WSN issues including hardware, new devices, network protocols, WSNs deployment architectures, operating systems, and applications, several research areas are still emerging from new needs and challenges. Integration of low powered WSN sensors into IoT will be a major evolution of WSNs.

There are a lot of challenges placed by the deployment of sensor networks which are a superset of those found in wireless ad hoc networks. Sensor nodes communicate over wireless, lossy lines with no infrastructure. An additional challenge is related to the limited, usually non-renewable or

battery-based energy supply of the sensor nodes [1]. The size of the nodes limits the size of the battery. The software and hardware design needs to carefully consider the issues of efficient energy use. For instance, data compression might reduce the amount of energy used for radio transmission, but uses additional energy for computation and/or filtering. The energy policy also depends on the application; in some applications, it might be acceptable to turn off a subset of nodes in order to conserve energy while other applications require all nodes operating simultaneously.

A sensor node usually consists of four sub-systems:

1. Computing subsystem: It consists of a microprocessor (microcontroller unit, MCU) which is responsible for the control of the sensors and implementation of communication protocols. MCUs usually operate under various modes for power management purposes. As these operating modes involves consumption of power, the energy consumption levels of the various modes should be considered while looking at the battery lifetime of each node.

2. Communication subsystem: It consists of a short-range radio which communicate with neighboring nodes and the outside world. Radios can operate under the different modes. It is important to completely shut down the radio rather than putting it in the Idle mode when it is not transmitting or receiving for saving power.

3. Sensing subsystem: It consists of a group of sensors and actuators and link the node to the outside world. Energy consumption can be reduced by using low power components and saving power at the cost of performance which is not required.

4. Power supply subsystem: It consists of a battery which supplies power to the node. It should be seen that the amount of power drawn from a battery is checked because if high current is drawn from a battery for a long time, the battery will die faster even though it could have gone on for a longer time. Usually the rated current capacity of a battery being

used for a sensor node is less than the minimum energy consumption. The lifetime of a battery can be increased by reducing the current drastically or even turning it off often.

To minimize the overall energy consumption of the sensor network, different types of protocols and algorithms have been studied so far all over the world. The lifetime of a sensor network can be increased significantly if the operating system, the application layer and the network protocols are designed to be energy aware. These protocols and algorithms have to be aware of the hardware and able to use special features of the micro-processors and transceivers to minimize the sensor node's energy consumption. This may push toward a custom solution for different types of sensor node design. Different types of sensor nodes deployed also lead to different types of sensor networks. This may also lead to the different types of collaborative algorithms in wireless sensor networks arena.

1.3.　　Power management

Energy consumption is the most important factor to determine the life of a sensor network because usually sensor nodes are driven by battery. Sometimes energy optimization is more complicated in sensor networks because it involved not only reduction of energy consumption but also prolonging the life of the network as much as possible. The optimization can be done by having energy awareness in every aspect of design and operation including the operation schedule and the communication protocols. This ensures that energy awareness is also incorporated into groups of communicating sensor nodes and the entire network and not only in the individual nodes. Listing few of the energy-aware protocols that are suggested in literature:

- Low-Energy Adaptive Clustering Hierarchy (LEACH):

Low-energy adaptive clustering hierarchy (LEACH) is a routing algorithm designed to collect and deliver data to the data sink, typically a base station [8]. The main objectives of LEACH are:

- Extension of the network lifetime
- Reduced energy consumption by each network sensor node
- Use of data aggregation to reduce the number of communication messages

To achieve these objectives, LEACH adopts a hierarchical approach to organize the network into a set of clusters. Each cluster is managed by a selected cluster head. The cluster head assumes the responsibility to carry out multiple tasks. The first task consists of periodic collection of data from the members of the cluster. Upon gathering the data, the cluster head aggregates it in an effort to remove redundancy among correlated values. The second main task of a cluster head is to transmit the aggregated data directly to the base station over single hop. The third main task of the cluster head is to create a TDMA-based schedule whereby each node of the cluster is assigned a time slot that it can use for transmission. The cluster head announces the schedule to its cluster members through broadcasting. To reduce the likelihood of collisions among sensors within and outside the cluster, LEACH nodes use a code-division multiple access–based scheme for communication.

The basic operations of LEACH are organized in two distinct phases. The first phase, the setup phase, consists of two steps, cluster-head selection and cluster formation. The second phase, the steady-state phase, focuses on data collection, aggregation, and delivery to the base station. The duration of the setup is assumed to be relatively shorter than the steady-state phase to minimize the protocol overhead.

At the beginning of the setup phase, a round of cluster-head selection starts. To decide whether a node to become cluster head or not a threshold T(s) is addressed in [8] which is as follows:

$$T(s) = \begin{cases} \dfrac{P_{opt}}{1 - P_{opt} \cdot \left(r.mod.\dfrac{1}{P_{opt}} \right)}, if\ s \in G' \\ 0, otherwise \end{cases} \tag{1}$$

Where r is the current round number and G is the set of nodes that have not become cluster head within the last 1/popt rounds. At the beginning of each round, each node which belongs to the set G selects a random number 0 or 1. If the random number is less than the threshold T(s) then the node becomes a cluster head in the current round.

- <u>Threshold-sensitive Energy Efficient Protocols (TEEN and APTEEN):</u>

Two hierarchical routing protocols called TEEN (Threshold-sensitive Energy Efficient sensor Network protocol), and APTEEN (Adaptive Periodic Threshold-sensitive Energy Efficient sensor Network protocol) are proposed in [9], [10] respectively. These protocols were proposed for time-critical applications. In TEEN, sensor nodes sense the medium continuously, but the data transmission is done less frequently. A cluster head sensor sends its members a hard threshold, which is the threshold value of the sensed attribute and a soft threshold, which is a small change in the value of the sensed attribute that triggers the node to switch on its transmitter and transmit. Thus, the hard threshold tries to reduce the number of transmissions by allowing the nodes to transmit only when the sensed attribute is in the range of interest. The soft threshold further reduces the number of transmissions that might have otherwise occurred when there is little or no change in the sensed attribute. A smaller value of the soft threshold gives a more accurate picture of the network, at the expense of increased energy consumption. Thus, the user can control the trade-off between energy efficiency and data accuracy. When cluster-heads are to change, new values for the above parameters are broadcast. The main drawback of this scheme is that, if the thresholds are not received, the nodes will never communicate, and the user will not get any data from the network at all.

- <u>Power-Efficient Gathering in Sensor Information Systems (PEGASIS):</u>

Power-efficient gathering in sensor information systems (PEGASIS) [11] and its extension, hierarchical PEGASIS, are a family of routing and information-gathering protocols for WSNs. The main objectives of PEGASIS are twofold. First, the protocol aims at extending the lifetime of a network by achieving a high level of energy efficiency and uniform energy consumption across all network nodes. Second, the protocol strives to reduce the delay that data incur on their way to the sink.

The network model considered by PEGASIS assumes a homogeneous set of nodes deployed across a geographical area. Nodes are assumed to have global knowledge about other sensors' positions. Furthermore, they have the ability to control their power to cover arbitrary ranges. The nodes may also be equipped with CDMA-capable radio transceivers. The nodes' responsibility is to gather and deliver data to a sink, typically a wireless base station. The goal is to develop a routing structure and an aggregation scheme to reduce energy consumption and deliver the aggregated data to the base station with minimal delay while balancing energy consumption among the sensor nodes. Contrary to other protocols, which rely on a tree structure or a cluster-based hierarchical organization of the network for data gathering and dissemination, PEGASIS uses a chain structure.

- Directed Diffusion:

Directed diffusion [12] is a data-centric routing protocol for information gathering and dissemination in WSNs. The main objective of the protocol is to achieve substantial energy savings in order to extend the lifetime of the network. To achieve this objective, directed diffusion keeps interactions between nodes, in terms of message exchanges, localized within limited network vicinity. Using localized interaction, direct diffusion can still realize robust multi-path delivery and adapt to a minimal subset of network paths. This unique feature of the protocol, combined with the ability of the nodes to aggregate response to queries, results into significant energy savings.

The main elements of direct diffusion include interests, data messages, gradients, and reinforcements. Directed diffusion uses a publish-and-subscribe information model in which an inquirer expresses an interest using attribute–value pairs. An interest can be viewed as a query or an interrogation that specifies what the inquirer wants.

- Geographic Adaptive Fidelity (GAF):

GAF [13] is an energy-aware location-based routing algorithm designed mainly for mobile ad hoc networks, but may be applicable to sensor networks as well. The network area is first divided into fixed zones and forms a virtual grid. Inside each zone, nodes collaborate with each other to play different roles. For example, nodes will elect one sensor node to stay awake for a certain period of time and then they go to sleep. This node is responsible for monitoring and reporting data to the BS on behalf of the nodes in the zone. Hence, GAF conserves energy by turning off unnecessary nodes in the network without affecting the level of routing fidelity.

The power management in this research:

The strategy adopted in our system is highly dependent on the communication protocol. It is implemented in the energy harvester's electronic interface, and it takes advantage of increasing the charging time and accumulating energy in the super capacitor to compensate for the lack of energy available for the harvester. This requires the node to be able to schedule its transmission/listening/Idle cycles in a periodic manner that gives a time window for the harvesting system to acquire the needed amount of energy. Low power communication protocols are the most suitable for our system such as SigFox and LoraWAN for the reason of having low transmission payloads and the ability to rely on scheduled data broadcasting since the usual network configuration is a star topology.

1.4.   Energy harvesting

Light, thermal gradients, motion or vibration, and radio frequency (RF) electromagnetic radioactivity comprise the four main forms of waste energy sources accessible for collecting. As alternate power supplies presenting different levels of efficacy depending on the application, all have gained notice [14].
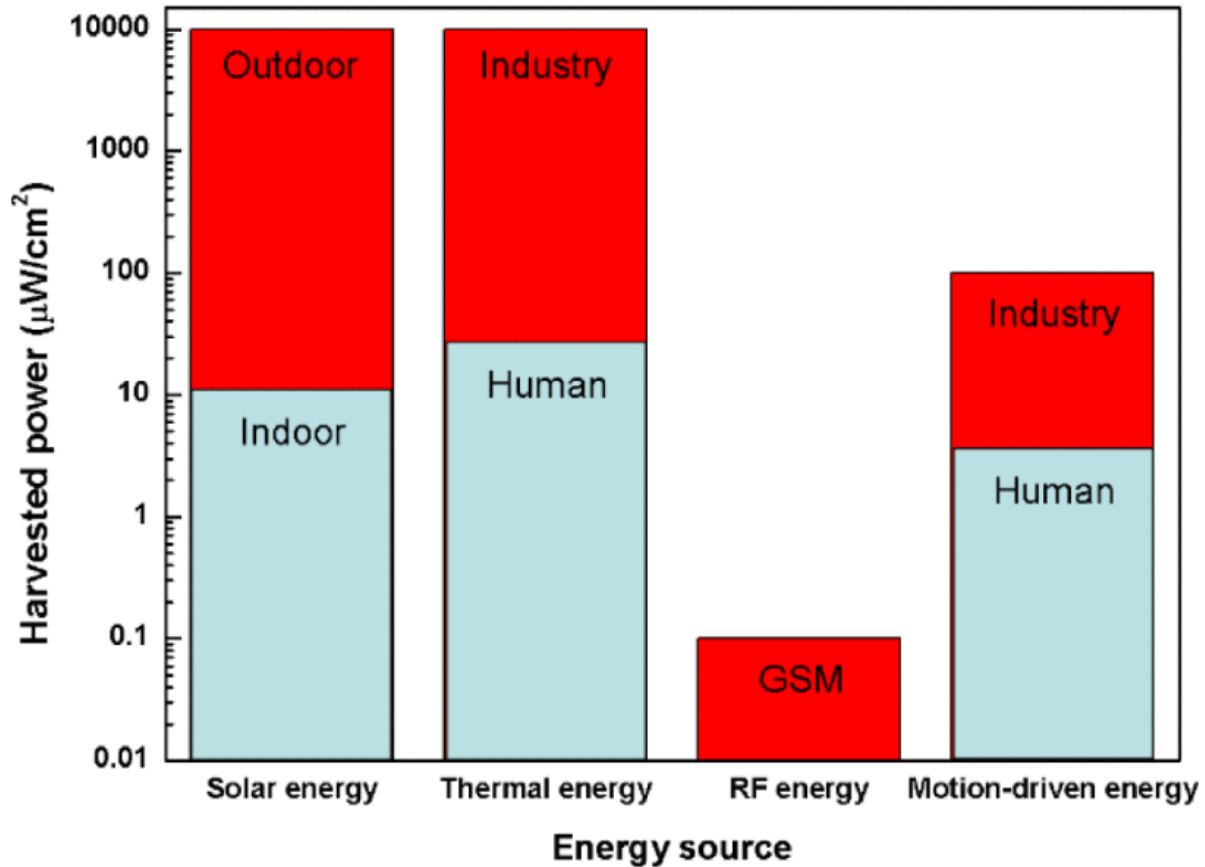
Figure 1. Estimation of the amount of available energy, with the associated application fields[15].

The most popular is likely solar energy. Solar cells provide outstanding power output in direct sunlight but are constrained in dim light. These are obviously undesirable in electrical appliances or structures where no illumination can be detected. Thermal energy can be easily converted into electricity by the Seebeck effect. A higher density of energy than solar cells is possible using thermoelectric transfer of body heat. Thermoelectric generators operate at all hours. Surrounding RF energy also is a potential source of energy storage. This is accessible via public phone networks, e.g., GSM, cellular channels. Environmental motion is one of the most important sources of energy extraction. Motion-driven energy is generally available as vibrations, random separations or forces and is usually changed to electrical energy by electromagnetic, piezoelectric or electrostatic transduction. Appropriate pulses can be found in many implementations.

Figure 1 shows the approximate amount of energy available for all four energy sources [15].

1.3.1 Motion-driven energy

Manipulating ambient motion or mechanical vibration is one of the best methods for applying an energy collection system. Motion-driven or vibration-driven energy recovery requires the conversion of mechanical energy into electrical energy via an electromechanical transducer. Mechanical-to-electrical energy transfer consists of two mechanisms: the direct use of force and employment of inertia operating on proof mass. For a direct-force device, the force f(t) operates directly on the mass m provided by the tension with the spring constant k and the damping factor c, leading to the displacement z(t). Energy is transformed from mechanical to electrical if the correct transduction system is used as a damping device. The working theory of the inertial engine is centered on a check mass m backed by a suspension with a spring constant k. The inertial mass of the evidence allows the mass to shift due to the frame with relative displacement z(t), while the frame with displacement y(t) encounters momentum. The energy of the inertial engine is transferred by means of a damping attribute that inhibit the activity of the proof mass in the frame.

Especially at the microscale, numerous motion-powered energy collectors have been shown. The production of devices capable of translating kinetic energy from movements, forces or displacements to electrical performance has progressed steadily over the last few years. For example, energy can be employed in a wide range of applications, including manufacturing equipment, shipping, household products, civil engineering systems, and portable electronics. The amount of energy generated by the external mechanical excitations depends specifically on the amplitude of the vibration or force, the frequency of the source, and the efficiency of the transducer. Including electromagnetic, electrostatic, and piezoelectric transduction, many types of transduction may be useful in energy storage devices. The preference of transduction methods relies largely on the implementations since there is no consensus as to the most desired transduction methods.

A. Electromagnetic transduction

The production of electric current i(t) in a conductor within a magnetic field B, according to Faraday's law is called electromagnetic power transfer. Electricity is produced by either relative motion z(t) of the magnet and the coil or by a shift in the magnetic flux (Figure 2). The velocity of the relative motion, the number of turns of the coil, and the strength of the magnetic field decide the sum of energy provided. Electromagnetic systems are commonly used for large-scale power generation owing to the highly powerful transfer of mechanical to electrical resources. The usage of this transduction method in small-scale energy storage applications has also been well documented.
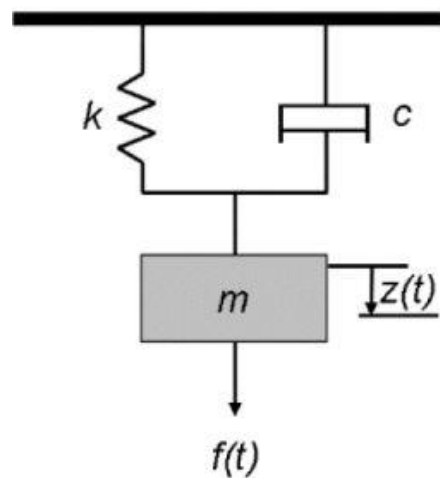
Figure 2. Direct-force generator

B. Electrostatic transduction

As shown in Figure 3, electrostatic devices use two conductive plates electrically separated by liquid, vacuum or an insulator. The acceleration or motion of a single adjustable conductive plate z(t) induces a shift in voltage through the plate, causing an i(t) current flow in an open circuit. These devices need a preload voltage from an outside voltage source, such as a battery for activity. Charging plates produce equivalent and opposite charges q(t) on plates, leading to a deposited

charge when the voltage source is removed. Typically, the power efficiency of electrostatic devices is improved by lowering the surface region or the volume of the plate. For this reason, the electrostatic generators are efficient at smaller scales and well suited to MEMS fabrication. However, there are two main challenges for practical realization of electrostatic generators: the generators require the input charge and extensive power circuitry to operate; and they produce low amounts of current due to high output impedance.
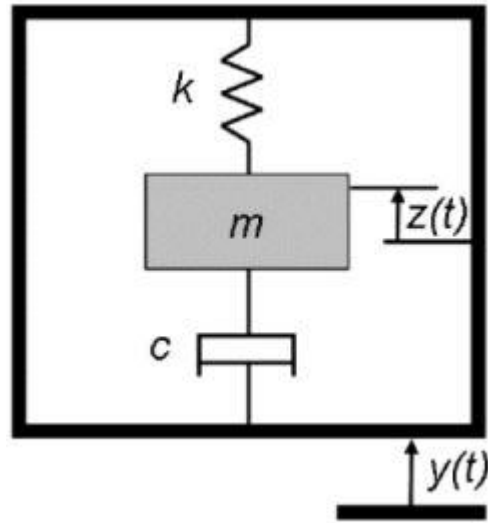
Figure 3. Inertial generator

C. Piezoelectric transduction

To change mechanical strain f(t) into electrical charge i(t), piezoelectric generators utilize the direct piezoelectric effect of a piezoelectric material. This transduction theory provides the easiest solution, wherein kinetic energy from structural movements or displacements is immediately changed to an electrical output with a fairly high-power density and no need for complicated geometries or various external parts. The most used piezoelectric materials for energy harvesting are aluminum nitride (AlN) and ferroelectric lead zirconate titanate (PZT). One key benefit is that piezoelectric transduction is especially well adapted for miniaturization utilizing micromanufacturing methods, as many methods are possible for the filing of thin and thick piezoelectric films. Piezoelectric materials are expected to be specifically strained, and thereby

their mechanical properties can decrease output, productivity, and lifespan. The preference of transduction methods relies largely on the implementations, as there is no proof as to the favored transduction methods.

Piezoelectric transducers in energy collection are more beneficial than electromagnetic devices, which have several practical restrictions in empowering micro-scale electromagnetic energy harvesters. Because of proven bulk and thin-film production methods and ease of use, piezoelectric devices can be produced on a macro-scale and micro-scale. Voltage outputs in electromagnetic energy collection are usually small, and multi-stage post-processing is often needed to achieve a level of voltage that can power a storage device. Conversely, functioning voltage outputs can be gained straight from the piezoelectric material during piezoelectric energy collection. An input voltage or charge must be used during electrostatic energy collection so that the comparative vibratory motion of the capacitor elements produces an alternating electrical output. In contrast, the voltage contribution of the piezoelectric energy collection is extracted from the constitutive action of the device, which prevents the need for external voltage input. Further, piezoelectric energy collectors have a wide range of activity at low frequencies, enabling them to be easily used to collect energy from various environmental frequencies.

1.3.2 Solar energy

Solar or light energy is the most popular energy source. Solar power systems are among the most widely accepted electricity-saving options. Solar cell energy is the product of the photovoltaic (PV) process of transforming received light into electricity. Individual PV cells (also defined as "solar cells") are electrically attached to create PV modules, which are the foundations of PV systems. The module is the smallest PV unit that is used to produce a large amount of PV electricity. While only small quantities of electricity are generated by individual PV cells, PV modules are developed with differing electrical outputs varying from a few watts to more than 100 watts of direct current (DC) electricity. Modules are linked to PV arrays to power a diverse variety of electrical devices. Two main types of widely viable PV technologies are crystalline silicon and thin film. In crystalline silicone architectures, individual PV cells are cut from large single crystals

or crystalline silicone ingots. For thin film technology, the PV substrate is mounted on glass or thin metal that physically protects the cell or frame. Thin-film-based modules are manufactured in sheets which are designed for prescribed electrical outputs. Both provide outstanding power efficiency in direct sunshine, but the usable indoor solar energy is greatly decreased relative to the surrounding environment.

1.3.3 Thermal energy

Temperature gradients existing in nature and the human body have the ability to generate electricity. The simplest thermoelectric generator is a thermocouple consisting of two legs comprised of various elements, as well as a metallic strip (Figure 4). A voltage V generation results from the temperature difference Δ T between the bottom and top of the legs. The voltage is fixed by:

$$V = (\alpha_1 - \alpha_2)\Delta T \qquad (2)$$

Where:

α_1 is Seebeck coefficient of material 1

α_2 is Seebeck coefficient of material 2.

The foundation of thermoelectric generation is an occurrence called the Seebeck effect. Normally, the legs comprise heavily doped p-type and n-type semiconductors for the best performance. Practically, a thermoelectric energy harvester is a thermopile, which is usually formed by many thermocouples linked electrically in sequence and thermally in parallel, as revealed in Figure 4. A good example of commercial realization of thermoelectric generators is the thermoelectric wristwatch that demonstrates the generation of electrical power from body heat to drive the watch. The main benefits of thermoelectric energy collectors include being solid-state, dependable, and size adaptable, meaning they are suitable for small portable applications. Including for wireless sensor networks, medical appliances, and mobile devices, their scalability to small sizes through micromachining allows the opportunity to collect minute amounts of heat for low power functions. Recently, micro thermoelectric devices utilizing thin thermoelectric materials have received a lot

of attention for powering microfabricated devices. Typically, power produced from the micro thermoelectric devices is muted in the microwatt to milliwatt range. Thus, much of the work has centered on refining thin film, and nanostructured thermoelectric materials and their configurations in order to generate adequate power and voltage from temperature variations as small as 5–10 ° C. Preserving the temperature grade between the hot and cold region at such a small scale is a significant challenge.
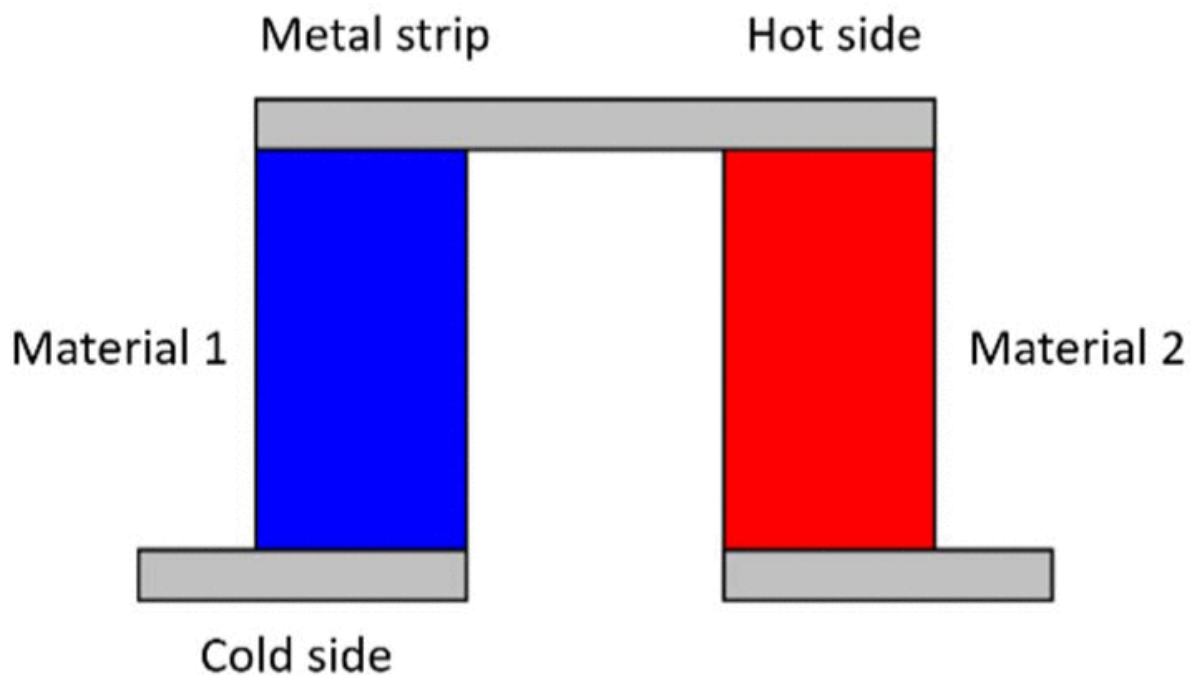
Figure 4. Schematic of thermocouple

1.3.4 Radio frequency energy

Collecting power from reproducing RF signals that are discharged by high electromagnetic fields such as TV signals, cell phone towers, and wireless radio wave networks (GSM, WIFI) is one energy collecting method for inactively powered devices. Using a power conversion circuit built into a receiving antenna, RF energy may be collected from the environment and transformed into a functional DC voltage. Intel has recently built a UHF antenna attached to a 4-stage charging system, which is capable of collecting 60 microwatts of electricity from a TV station 4 km away.

Still, the usable power level in the RF energy collection device is a subject of concern because the distribution of RF energy declines steadily as the distance from the source grows. The key technical innovation that will enable this technology to produce enough power is through the production of receivers with a wide frequency band and highly sensitive and effective power conversion solutions.

1.5.   Energy harvesting for sensor nodes

Conversion efficiency metrics are typically used as a measure of the performance of the energy harvesting interface circuits. The two most commonly used metrics are power conversion efficiency and voltage conversion efficiency. The latter is typically used for rectifier topologies and describes the ratio between the output and the input voltage amplitudes. Power conversion efficiency shows the ratio between the average output and input power levels in steady state conditions, and is affected by the magnitudes of the input voltage and of the output current. The application of this metric in low power applications such as WSN and IoT is severely limited by factors such as the several orders of magnitude difference in reported generated power levels compared to high power energy harvesters, different load assumptions, consideration of control circuit overheads, and the coupled effects of electrical damping on the harvester's performance. When power electronic interface circuits are considered as part of energy harvesting systems, the priority shifts from optimizing the power transfer into ensuring the functionality of the circuit in addition. more application-oriented metrics are desirable, describing, for example, the minimum operating power level or the ability of a circuit to operate a harvesting system close to the theoretical maximum obtainable power output. Harvester utilization describes the ability of a particular load to extract power; this factor is defined as the ratio between the output power at the generator's terminals and the maximum power that could be achieved with an optimal load [16]. When comparing different approaches, both the utilization of the harvester and the efficiency of the power conditioning components must be taken into account [17]. High-power conversion efficiency does not imply maximum power, as evidenced by the well-known peak power transfer theorem. Overall harvesting system efficiency can be considered as the product of the harvester utilization and the power conversion efficiency of the interface circuitry.

1.6.   Conclusion

In this chapter the importance of Wireless Sensor Networks was discussed from the application and design point of view. The recent interests in technology and the advancement of the internet infrastructure makes the Internet of Things IoT and WSN closer than ever. Both sharing multiple goals and challenges, one of the biggest design constraints is the power consumption. The energy efficiency issue is tackled in different design phases, namely the telecommunication protocol, the system design, the software and task scheduling and the power sourcing.

One of the most prominent is renewable energy, which is being increasingly integrated in modern IoT systems. Ambient energy harvesting technology has been studied based on its working principles, types of energy harvester, optimization techniques, and their potential in practical application. The four primary forms of ambient energy sources are presented. The motion-driven energy was selected as the energy target in this thesis because it has advantages with respect to others:

1- The motion-driven energy is the third higher available power density form, and most appear in human motion and industry. Besides, the technology is used to harvest this energy, including electromagnetic transduction, electrostatic transduction, and piezoelectric transduction, and they have high potential to harvest energy for use in the real application in the field of self-power electronic systems, wearable and portable devices, and the sensors for Internet of the Things.

2- Solar energy has gained interest as a solution to energy gathering because of its high accessibility outdoors but has the low power density in the dim ambient light condition, and the device is used to harvest solar energy usually be a solar cell.

3- Thermoelectric energy also has a high available power density as solar energy. The human heat, and ambient temperature are the most common use for harvesting energy.

4- Finally, the RF energy has the lowest available power density and unstable for harvesting energy depend on the distance from the RF energy source, the climate condition, and other issues.

Chapter 2.   Switching Converters

2.1.   Introduction

The switching converters are a very essential type of power converters and are widely used for regulation and power transfer applications. What makes this type of converters unique is the integration of transistors that operate in saturation mode to play the role of voltage-controlled switches. Regulators based on switching converters have proven to have the highest efficiency among other forms of voltage regulators. This efficiency depends on the configuration and the application the switching converter is being used with. These converters come in three main configurations, *Buck, Boost* and *Buck-Boost.* As the name explains, the buck converter is a step-down converter that gives an output voltage with a lower value than the input voltage, the boost converter is a step-up, and the buck-boost can be configured to wither be a step-up or a step-down converter.

In this chapter, a brief explanation of the different switching converters type is given, as well as their importance and how they are used in energy harvesting applications. Simulations were also made to study the behavior of different components inside the converter circuits and methods have been investigated to solve some power consumption issues and give a higher efficiency on the hardware level [18].

2.1.1 Buck converters

The fundamental circuit for an ideal step-down (buck) converter is shown in Figure 5. The output voltage is sensed and then regulated by the switch control circuit. There are several methods for controlling the switch, but for we assume that the switch is controlled by a pulse width modulator (PWM) operating at a fixed frequency f.

$$f = \frac{1}{t_{on} + t_{off}}$$
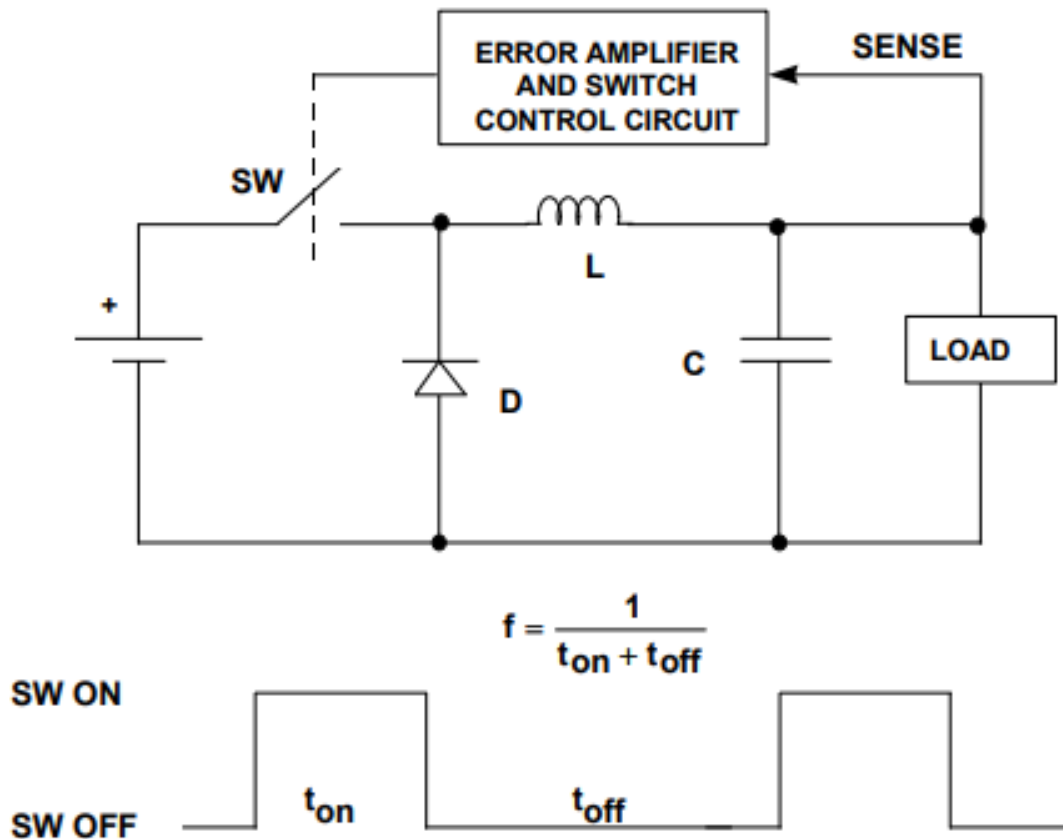
Figure 5. The basic Buck converter architecture, showing the driving PWM signal.

When the switch is on, the voltage VIN–VOUT appears across the inductor, and the inductor current increases with a slope equal to (VIN–VOUT)/L (see

$i_{IN} = i_{SW}$ $i_L = i_{OUT}$

I_{IN} I_{OUT}

V_{IN} V_D V_{OUT}

SW

L

i_D D

C

LOAD

Lower Case = Instantaneous Value
Upper Case = Average Value

V_D V_{IN} t_{on} t_{off} t_{on} A

0

$i_L = i_{OUT}$ I_{OUT} B

$\dfrac{V_{IN} - V_{OUT}}{L}$ $\dfrac{-V_{OUT}}{L}$ (SLOPES)

0

i_D I_{OUT} C

0

$i_{IN} = i_{SW}$ I_{OUT} D

I_{IN}

0
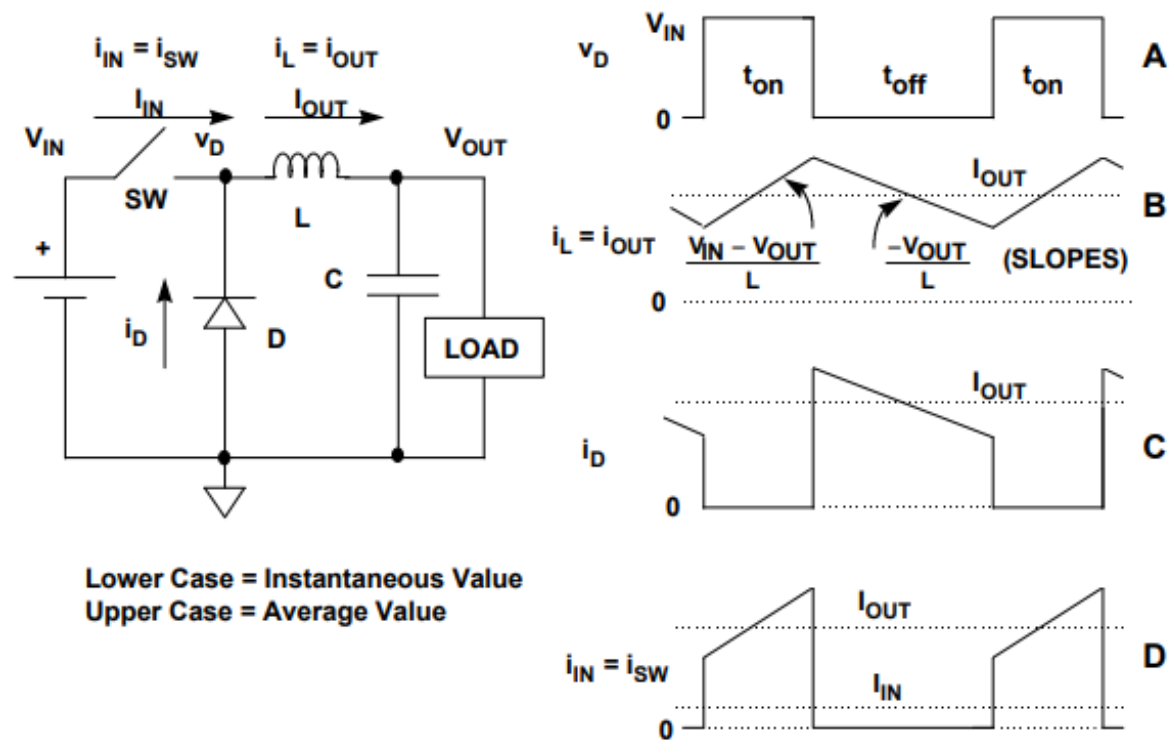
Figure 6). When the switch turns off, current continues to flow through the inductor and into the load for the reason that the current cannot change instantaneously in an inductor, with the diode providing the return current path. The voltage across the inductor is now VOUT, but the polarity has reversed. Therefore, the inductor current decreases with a slope equal to – VOUT/L. Note that the inductor current is equal to the output current in a buck converter. The diode and switch currents   are   shown   in

Lower Case = Instantaneous Value
Upper Case = Average Value
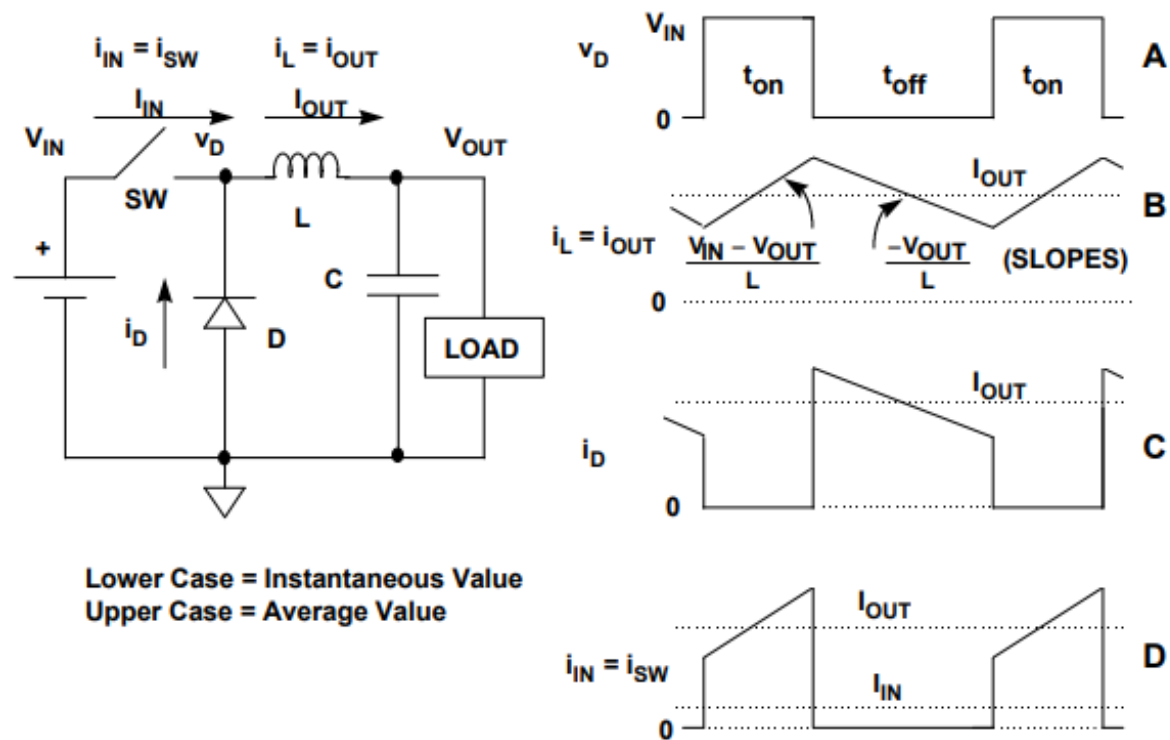
Figure 6, and the inductor current is the sum of these waveforms. Also note by inspection that the instantaneous input current equals the switch current. In practice, both the switch and the diode have voltage drops across them during their conduction which creates internal power dissipation and thus a loss of efficiency, but these voltages will be neglected for now. It is also assumed that the output capacitor, C, is large enough so that the output voltage does not change significantly during the switch on or off times.

Lower Case = Instantaneous Value
Upper Case = Average Value
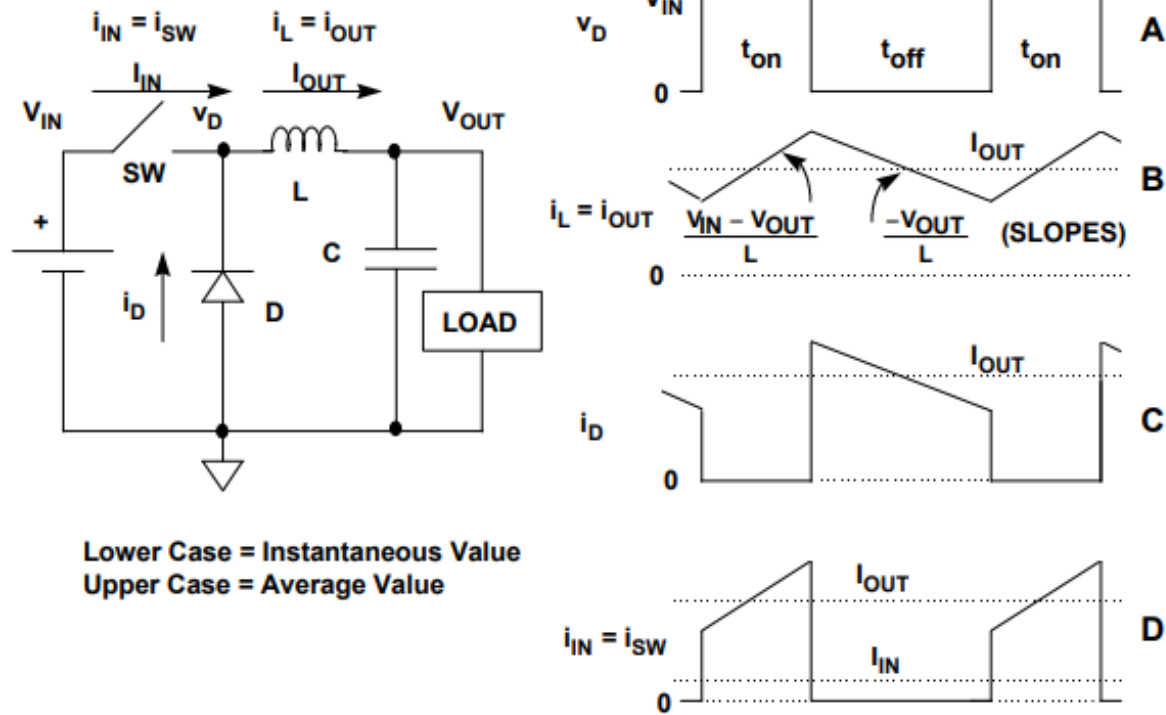
Figure 6), the basic relationship between the input and output voltage may be derived by inspecting the inductor current waveform and writing:

$$\frac{(V_{in} - V_{out})}{L} t_{on} = \frac{V_{out}}{L} t_{off} \tag{3}$$

Solving for VOUT:

$$V_{out} = V_{in} \frac{t_{on}}{t_{on} + t_{off}} = V_{in} \cdot D \tag{4}$$

where D is the switch duty cycle, defined as the ratio of the switch on-time (ton) to the total switch cycle time (ton + toff). This is the classic equation relating input and output voltage in a buck converter which is operating with continuous inductor current, defined by the fact that the inductor current never goes to zero.

There are several important things to note about these waveforms. The most important is that ideal components have been assumed, i.e., the input voltage source has zero impedance, the switch has
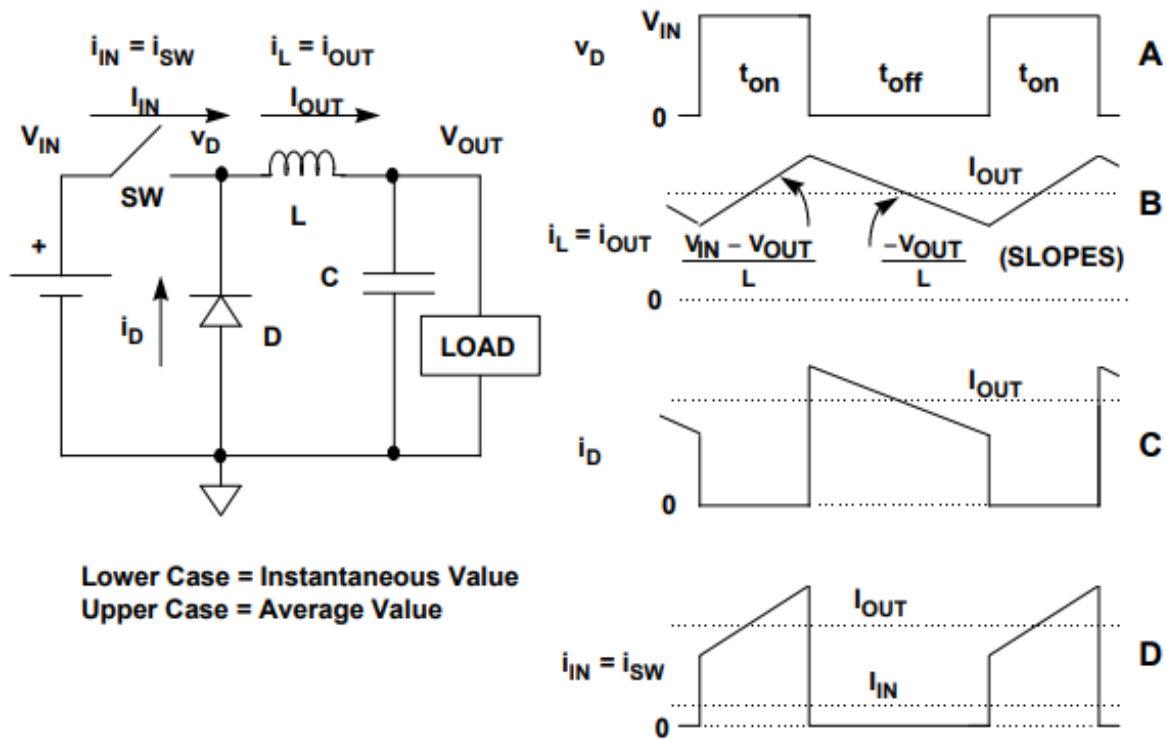
Figure 6. Functionality of the Buck converter, showing the signals in different nodes.

zero on-resistance and zero turn-on and turn-off times. It is also assumed that the inductor does not saturate and that the diode is ideal with no forward drop.

Also note that the output current is continuous, while the input current is pulsating. Obviously, this has implications regarding input and output filtering.

2.1.2 Boost converters

The basic step-up (boost) converter circuit is shown in Figure 7. During the switch on-time, the current builds up in the inductor. When the switch is opened, the energy stored in the inductor is transferred to the load through the diode.

When the switch is on, the voltage VIN appears across the inductor, and the inductor current increases at a rate equal to VIN/L. When the switch is opened, a voltage equal to VOUT – VIN
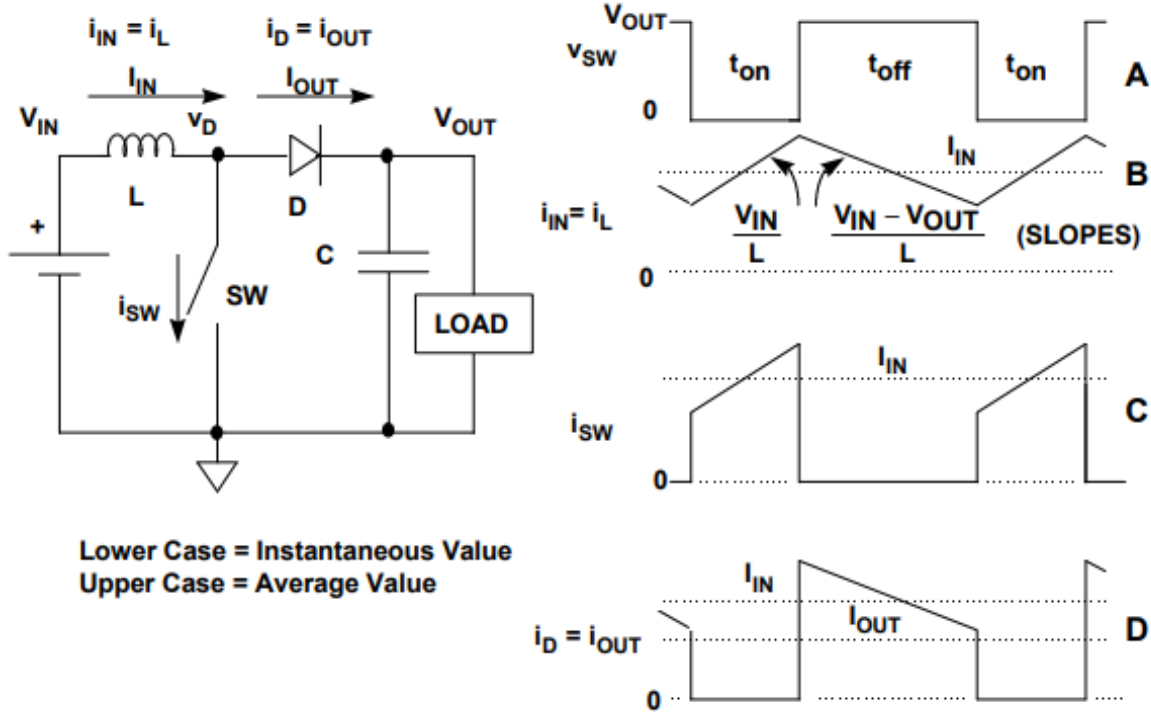
Figure 7. Architecture of the Boost converter, showing the signals in different nodes.

appears across the inductor, current is supplied to the load, and the current decays at a rate equal to (VOUT – VIN)/L. The inductor current waveform is shown in Figure 7.

Note that in the boost converter, the input current is continuous, while the output current is pulsating. This implies that filtering the output of a boost converter is more difficult than that of a buck converter. Also note that the input current is the sum of the switch and diode current. If a steady-state condition exists, the basic relationship between the input and output voltage may be derived by inspecting the inductor current waveform and writing:

$$\frac{V_{in}}{L} t_{on} = \frac{V_{out} - V_{in}}{L} t_{off} \tag{5}$$

Solving for VOUT:

$$V_{out} = V_{in}\frac{t_{on} + t_{off}}{t_{off}} = V_{in}\cdot\frac{1}{1 - D} \tag{6}$$

2.1.3 Buck-Boost converters

The simple buck converter can only produce an output voltage which is less than the input voltage, while the simple boost converter can only produce an output voltage greater than the input voltage. There are many applications where more flexibility is required. This is especially true in battery powered applications, where the fully charged battery voltage starts out greater than the desired output (the converter must operate in the buck mode), but as the battery discharges, its voltage becomes less than the desired output (the converter must then operate in the boost mode). A buck-boost converter can produce an output voltage which is either greater than or less than the absolute value of the input voltage. A simple buck-boost converter topology is shown in Figure 8. The input voltage is positive, and the output voltage is negative. When the switch is on, the inductor current builds up. When the switch is opened, the inductor supplies current to the load through the diode. Obviously, this circuit can be modified for a negative input and a positive output by reversing the polarity of the diode.
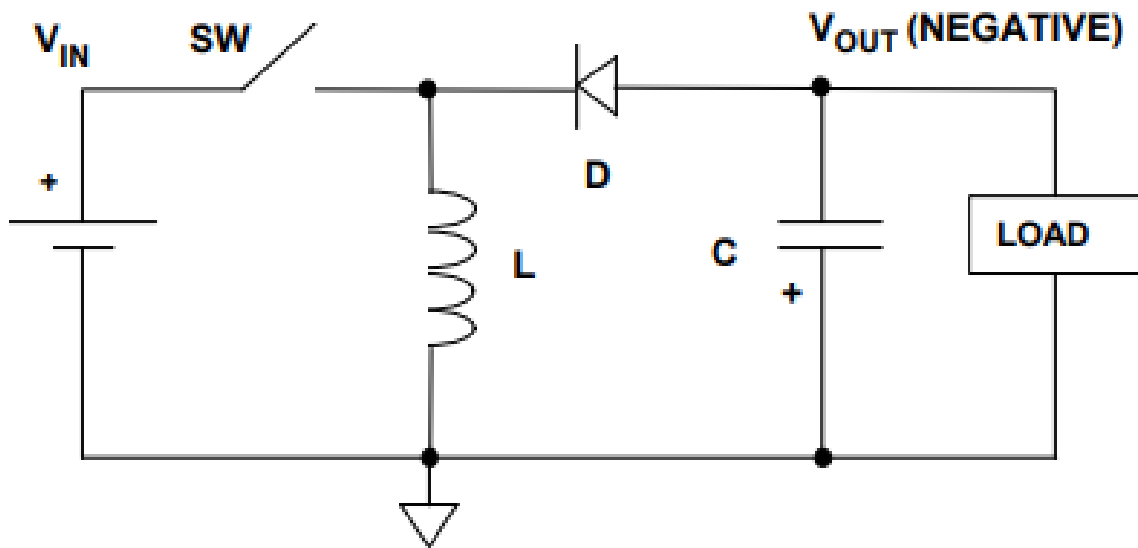
Figure 8. Architecture of an inverting Buck-Boost converter.

A second buck-boost converter topology is shown in Figure 9. This circuit allows both the input and output voltage to be positive. When the switches are closed, the inductor current builds up. When the switches open, the inductor current is supplied to the load through the current path provided by D1 and D2. A fundamental disadvantage to this circuit is that it requires two switches and two diodes. As in the previous circuits, the polarities of the diodes may be reversed to handle negative input and output voltages.
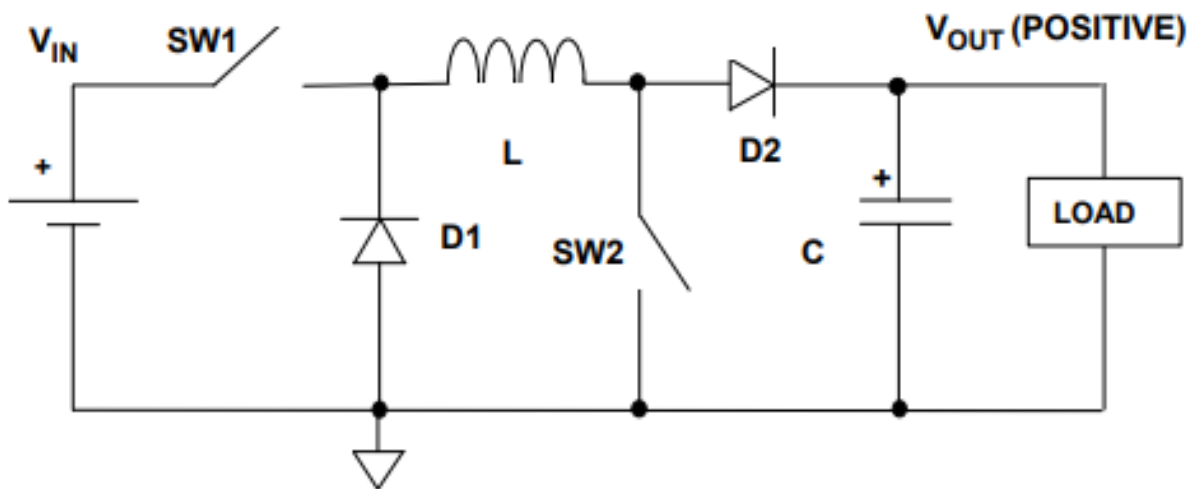
Figure 9. Architecture of a non-inverting Buck-Boost converter.

This topology is practically a cascade of a buck and a boost converter, and basically the relationship between the input and output voltage may be derived by multiplying the relations for both converters and writing:

$$V_{out} = \frac{D}{1-D} \cdot V_{in} \tag{7}$$

2.1.4 Discontinuous Conduction mode

This discussion so far has assumed the regulator is in the continuous mode of operation, defined by the fact that the inductor current never goes to zero. If, however, the output load current is decreased, there comes a point where the inductor current will go to zero between cycles, and the inductor current is said to be discontinuous. It is necessary to understand this operating mode as well, since many switchers must supply a wide dynamic range of output current, where this phenomenon is unavoidable. Waveforms for discontinuous operation for buck converter are shown in Figure 10(a).
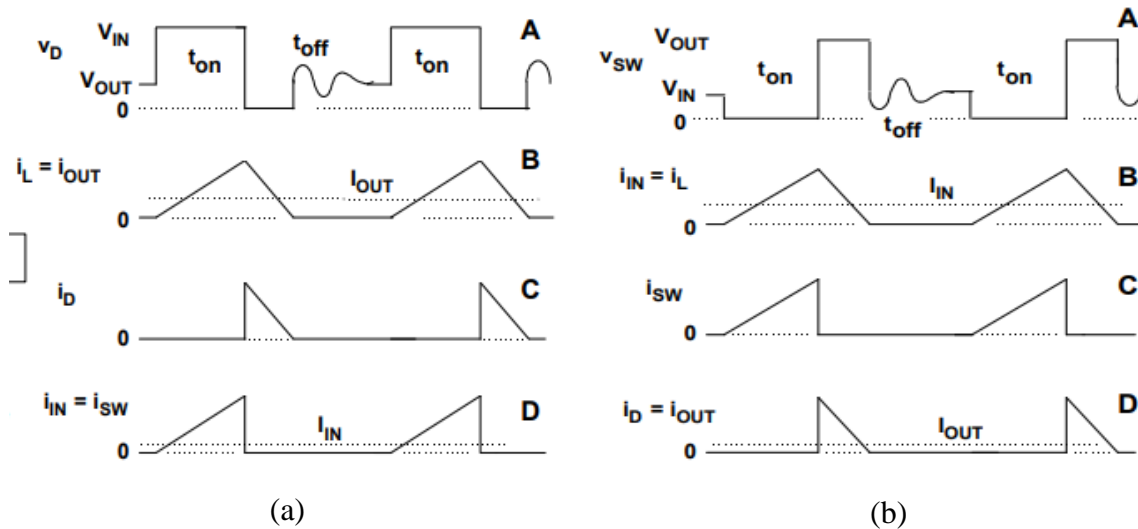
Figure 10. The signals in DCM mode for (a) Buck converter, (b) Boost converter.

Behavior during the switch on-time is identical to that of the continuous mode of operation. However, during the switch off-time, there are two regions of unique behavior. First, the inductor current ramps down at the same rate as it does during continuous mode, but then the inductor current goes to zero. When it reaches zero, the current tries to reverse but cannot find a path through

the diode any longer., so the voltage on the input side of the inductor (same as the diode and switch junction) jumps up to VOUT such that the inductor has no voltage across it, and the current can remain at zero. Same for the boost converter but the voltage on the diode and switch junction jumps to VIN.

Because the impedance at diode node (vD) is high, ringing occurs due to the inductor, L, resonating with the stray capacitance which is the sum of the diode capacitance, CD, and the switch capacitance, CSW. The oscillation is damped by stray resistances in the circuit, and occurs at a frequency given by:

$$f_0 = \frac{1}{2\pi\sqrt{L(C_D + C_{SW})}} \tag{8}$$

2.2.   AC/DC converters

The simplest AC/DC converters comprise of a rectifier followed by a filtering stage to smooth the rectified signal, into a DC/DC converter. If the input source is high voltage, rectification occurs after the transformer. The rectifiers are implemented using semiconductors, mainly diodes, or other devices such as transistors and varistors depending on the application. High efficiency converters can use active devices like MOSFETs as switches in such circuits. The reason for using topologies that are more complex is usually for efficiency improvement, to lower noise or to act as a power control. Diodes have an intrinsic voltage drop across them when they conduct. This causes power to be dissipated in them, but other active elements may have much lower drop and therefore lower power loss.

Another AC/DC topology is the bridgeless AC/DC converter [19], [20], it combines a boost converter and a buck-boost converter to condition the positive and negative half cycles of the input AC voltage (Figure 11). Only one inductor and capacitor are used in both circuitries to reduce the size of the converter. The principle of operation of this type of converters is a bit sophisticated, but simply put, the switch SW1 is always closed during the positive cycle of the input signal while the
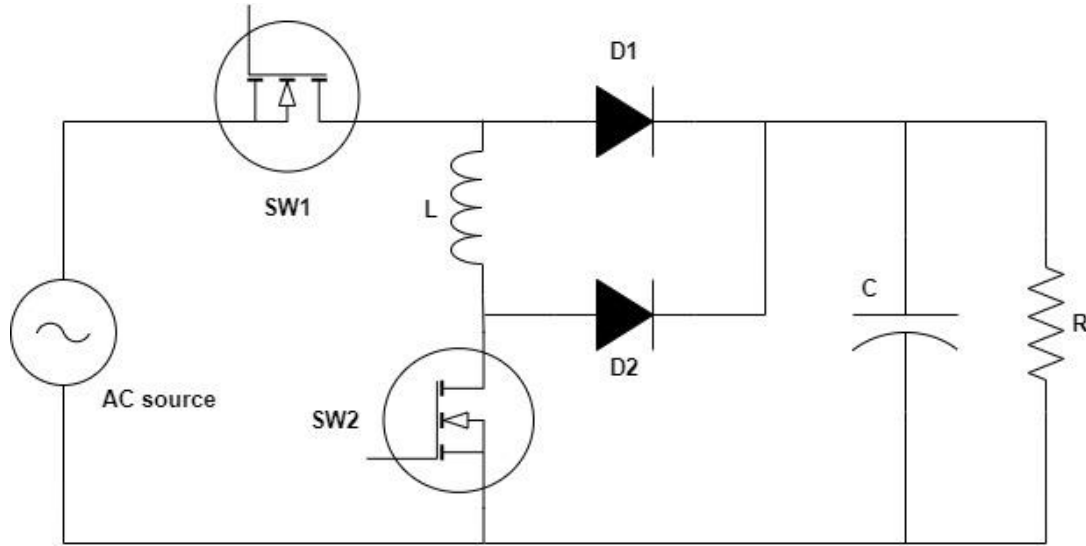
Figure 11. Architecture of the bridgeless converter.

switch SW2 is derived by the PWM signal, what makes D2 forward biased and the whole converter acts as a Boost converter. During the negative cycle of the input signal, the switch SW2 is always closed while the PWM signal drives the switch SW1, biasing the diode D1 forward and making the device act as a buck-boost converter.

2.3.   Switching converters in energy harvesting

Switching converters are mainly used as regulators and in power supply devices, where the goal is to wither step-up or step-down the output voltage, or even provide multiple levels for output voltage. This is achieved by controlling the duty cycle in addition to the control of the output voltage through a feedback loop that ensures the stability of the signal.

However, energy harvesting applications benefit from a different function of these converters. The interesting characteristic that is exploited is the ability to control the output resistance through the switching PWM duty cycle. This is important when dealing with energy harvesters due to the fact that the environment conditions keep changing randomly, and that changes the electrical characteristics of the harvesters, what requires the electrical circuit to dynamically adapt to these changes. An example of this would be the buck-boost converter running in DCM mode, where the equivalent input resistance is given by this equation [21][22]:

$$R_{EQ} = \frac{2L}{D^2 t_{CK}} \qquad (9)$$

The type and topology of the converter depends on the harvester, whether it is a wind turbine or solar energy harvester etc..

2.3.1 Hybrid harvesters

Hybrid harvesters have been studied frequently with the main goal to extract energy from multiple harvesters in synchronization. The energy harvesters can be the same or different types, and can have either AC or DC signal output. Many methods have been proposed to deal with the problem of multiple harvesters. Naming three of these methods from the literature [23], Figure 12 shows the configuration of the hybrid systems in block diagram.

The first method illustrated by Figure 12(a) is the most used method and it consists of using two different interface circuits that contain a switching converter to convert the signal into DC. And then combine the 2 output signals that were stored in a super capacitor. This method takes the most resources due to the usage of two different interface circuits.

The second method Figure 12(b) consists of using an intermediate interface circuit that transforms the voltage signal from AC to DC , mainly rectifier and filter, then combining the two rectified signals into a switching converter with one shared inductor and different input loops. The two input loops are controlled through a clock generator and control logic block that provides a controlled PWM signal to the input switches. This method is more efficient than the first one since it has shared parts of the circuit such as the inductor that is a physically a large component and it is better to avoid using many inductors in the same circuit.
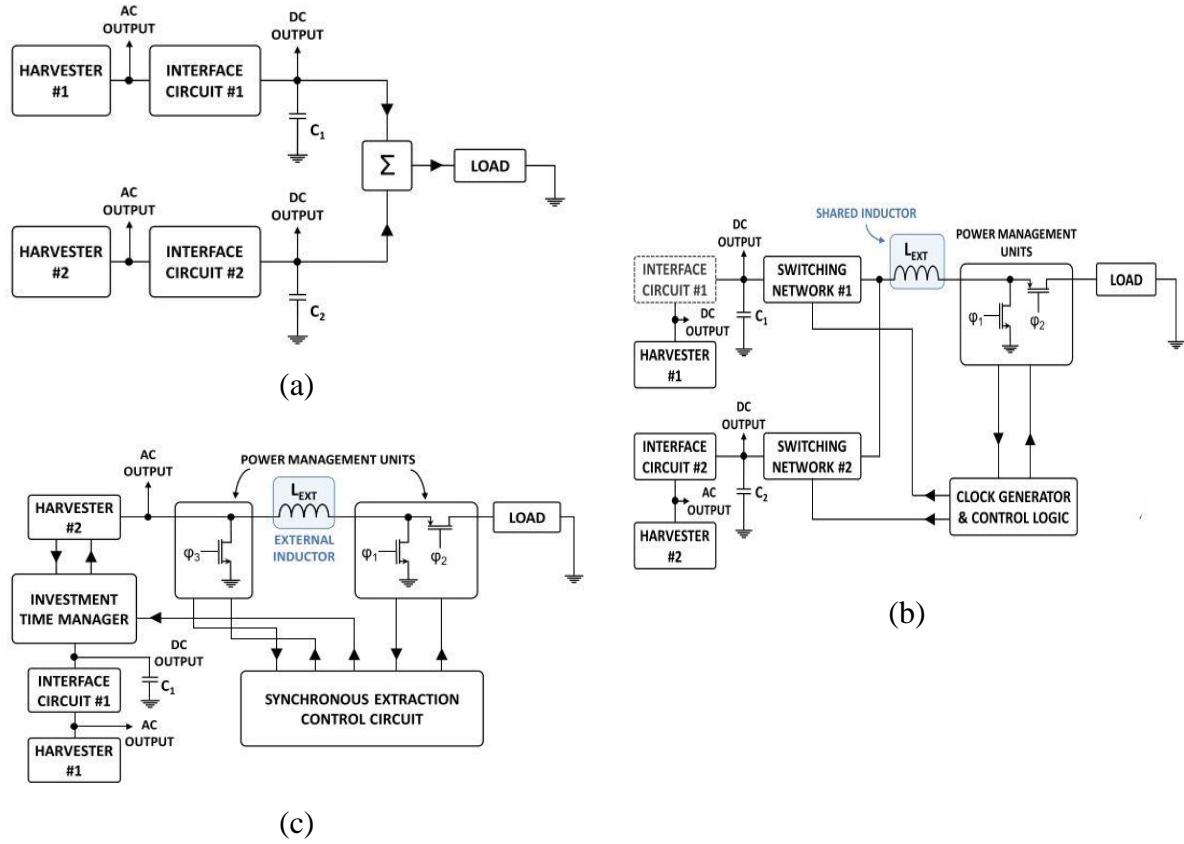
Figure 12. Different configurations for hybrid harvesters, (a) signal sum based, (b) shared inductor, (c) synchronized control.

The third method in Figure 12(c) introduces a new technique that uses a time manager circuit. The voltage signal from the first harvester is transformed into DC using an interface circuit, in this case the first harvester is an electromagnetic harvester that does not need the same input control as the other type of harvesters. The DC output goes then to the time manager that fills the gaps in the second harvester's output signal to ensure a compensation between one harvester and the other. The signal then goes to the second interface that contains a power management unit and a PWM generator and controller. This method proved to be more efficient than the first two when dealing with hybrid harvesters including an EM energy harvester [24], [25].

2.4. Efficiency model

For the sake of understanding the behavior of the non-inverting DC/DC buck-boost converter output (Figure 13), and what factors control the efficiency we described the circuit with an analytical model that can be used as a good estimation for the experimental results.
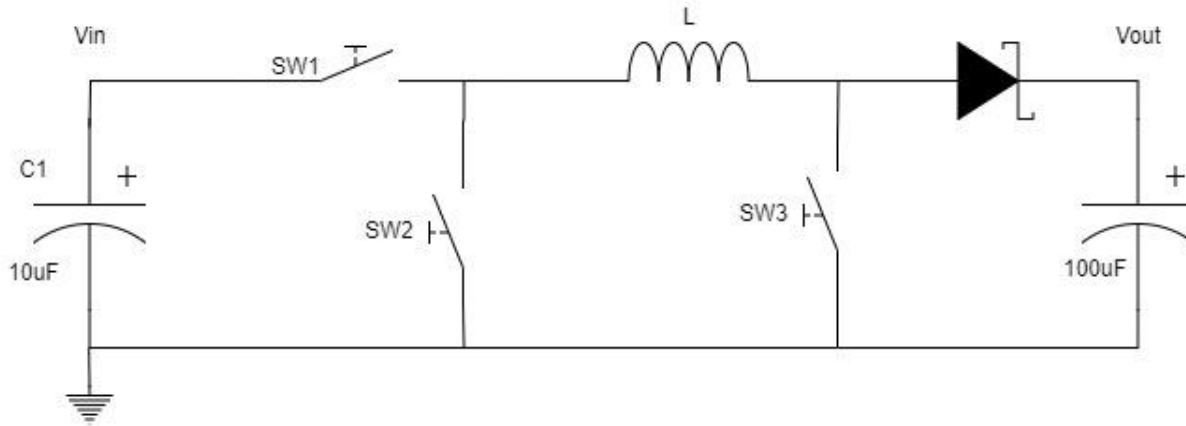
Figure 13. The non-inverting Buck-Boost converter that is used to derive the model.

In our circuit the boost converter is taking its input voltage as a full wave rectified sinusoidal signal, using a MOSFET bridge. The input voltage source is characterized with its internal inductance (20mH) and resistance (300Ω), which limit the power transfer to the boost converter to 50% at best. We then assume that the input voltage **Vin** across the **C1** capacitor is equal to $|3sin\,(20\pi t)|/_2$

The switches assumed ideal, are controlled with a PWM signal where the switches SW1 and SW3 are in phase and the switch SW2 is in opposite phase. The problem is analyzed considering two stages, during the ON time where the switches SW1 and Sw3 are closed while SW2 is open, and then during the OFF time where SW1 and SW3 are open and SW2 is closed. Respectively calling them the ON and OFF loops.

The switching frequency is higher in order of magnitude of the AC signal frequency, therefore we can assume that the input voltage is constant during each PWM period "Tck", allowing us to quantize its value, for instance $V_{in,k}$. The analysis is made for a single PWM period:

- $t \leq Ton$

During Ton, the current starts flowing through the inductor. The inductance L is assumed big enough so that the variation of iL,k is linear.

We get:

$$i_{L,k} = \frac{V_{in,k}}{L} t \tag{10}$$

The peak is reached when $t = TON$:

$$I_{p,k} = \frac{T_{ON}}{L} V_{in,k} \tag{11}$$

The inductor current is illustrated in Figure 14, at $t = Ton$ the inductor current iL,k has the value of Ip,k, and then it drops to 0 during TD the discharge time. This operation assumes that the converter is always in discontinuous conduction mode DCM.
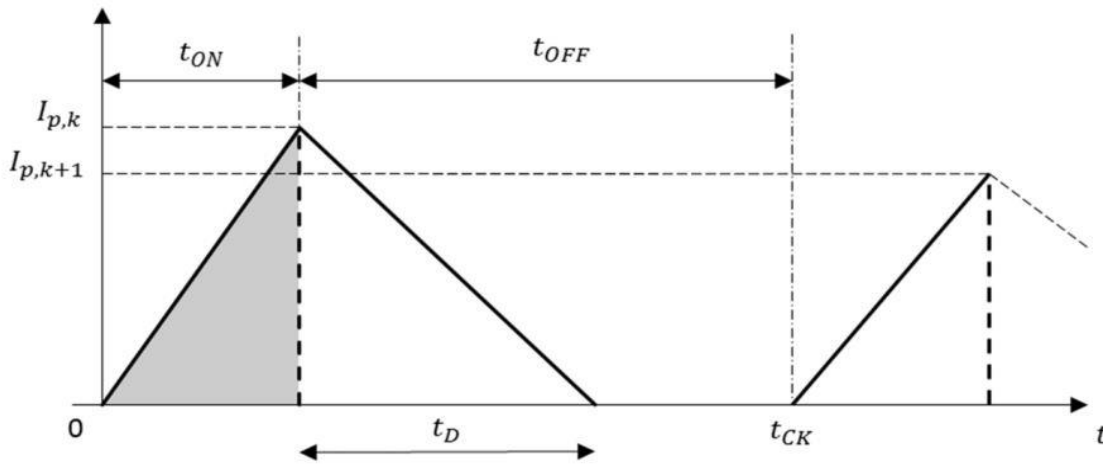
Figure 14. The inductor current.

- **$Ton < t \leq Tck$:**

The discharge of L is also linear, what gives this equation to describe iL during the OFF time:

$$i_{L,k}(t) = \begin{cases} I_{p,k} - \dfrac{V_{L,k}}{L} t & t \leq T_D \\ \\ 0 & t > T_D \end{cases} \tag{12}$$

Where VL,k is the voltage across the inductor and its equal to ($VD + Vo,k$)

TD can be found from Equation 12:

$$T_{D,k} = \frac{LI_{p,k}}{V_{L,k}} \tag{13}$$

From the current Equation 12 we can also retrieve the charge produced at the output capacitor **C2** as the following:

$$q_k(t) = \int i_{L,k}\ dt = \begin{cases} I_{p,k}t - \dfrac{V_{L,k}}{2L}t^2 + cte & t \leq T_D \\[3mm] cte & t > T_D \end{cases} \tag{14}$$

Replacing with Equation 13, during the period **TD,k** the charge at the capacitor increases by:

$$\Delta Q_k = q_k \bigg|_0^{T_{D,k}} = I_{p,k}T_{D,k} - \frac{V_{L,k}}{2L}\left(T_{D,k}\right)^2 = \frac{LI_{p,k}^2}{V_{L,k}} - \frac{LI_{p,k}^2}{2V_{L,k}} = \frac{LI_{p,k}^2}{2V_{L,k}} \tag{15}$$

C2 is big enough so that the charge remains constant during **TON**. Therefore, at any time **t**, the stored charge in the output capacitor **C2** is:

$$q_k = \frac{LI_{p,k}^2}{2V_{L,k}} + q_{k-1} \tag{16}$$

That gives us the output voltage:

$$V_{out,k} = \frac{q_k}{C} = \frac{LI_{p,k}^2}{2CV_{L,k}} + V_{out,k-1} \tag{17}$$

We can then derive the expression for the energy transferred to C2 at any time:

$$E_{out,k} = \frac{1}{2}C(V_{out,k})^2 \tag{18}$$

The efficiency is calculated through the ratio of the output power over the input power over time:

$$eff = \frac{P_{out}}{P_{in}} = \frac{E_{out}/t}{E_{in}/t} = \frac{E_{out}}{E_{in}} \tag{19}$$

Where:

$$E_{in,k} = \frac{LI_{p,k}^2}{2} = \frac{\left(T_{ON}V_{in,k}\right)^2}{2L} \tag{20}$$

These equations were simulated in MATLAB given the parameters below, for the duration of 2ms:

L = 470μH; C1 = 10μF; C2 = 10mF; Vin = |3sin (20πt)|/2 ; Vd = 300mV ; TON = 25μs ; TCK = 200μs; f = 10Hz / T = 0.1s

Figure 15 shows a plot of the input vs output voltage, and the efficiency growth for a DC input of 3V and a rectified AC signal with the formula mentioned above.
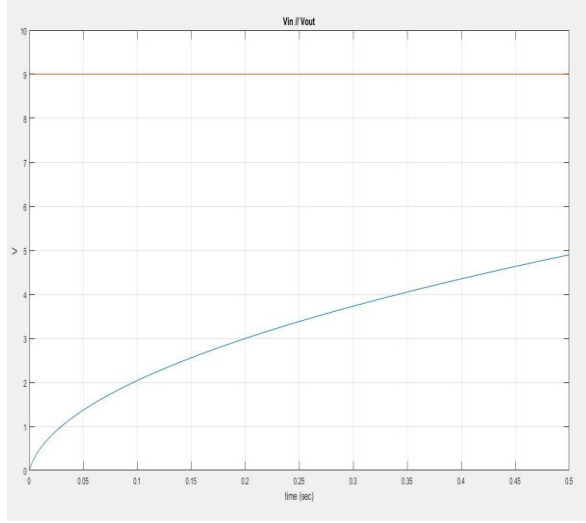
(a)
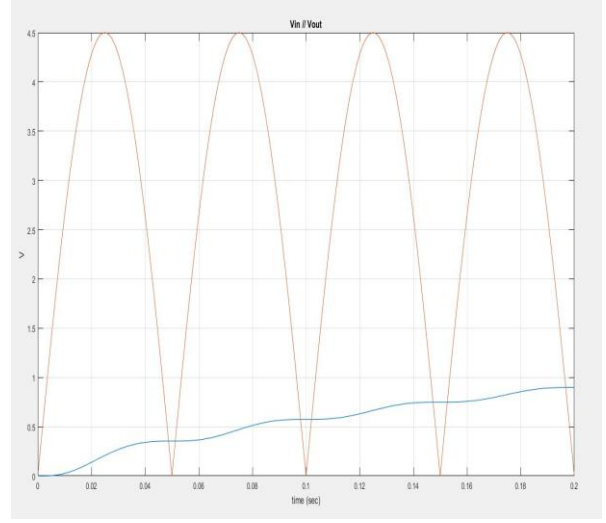
(b)
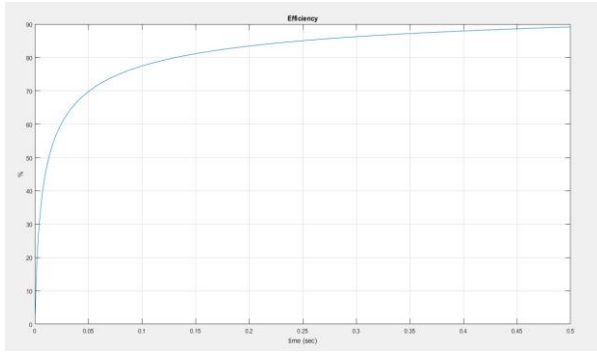
(c)
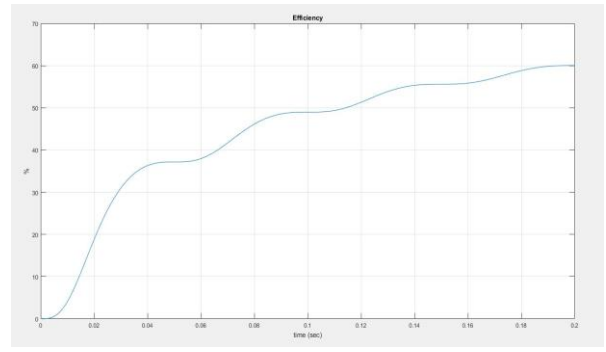
(d)

Figure 15. Simulation results showing the circuit efficiency for (a) AC input, (c) DC input, and the input vs output voltages for (b) AC input and (d) DC input.

If we evaluate the limit of *eff* as N goes to infinity we get:

$$\lim_{N\to\infty}\frac{\frac{1}{2}C\left(V_{out,N}\right)^2}{\sum_0^N E_{in,k}}=\lim_{N\to\infty}\frac{\frac{1}{2}C\left(V_{out,0}+\frac{T_{ON}^2}{2LC}\sum_1^N\frac{\left(V_{in,k}\right)^2}{V_D+V_{out,k-1}}\right)^2}{\frac{T_{ON}^2}{2L}\sum_0^N\left(V_{in,k}\right)^2} \tag{21}$$

If we consider **Vout,0 = 0V**, and at the infinity **Vk-1>>Vd**, and the input voltage **Vin** is purely DC we get:

$$\lim_{N\to\infty} \frac{\frac{1}{2}C\left(\frac{T_{ON}^2}{2LC}N(V_{in})^2\sum_1^N\frac{1}{V_{out,k-1}}\right)^2}{\frac{T_{ON}^2}{2L}(N+1)(V_{in})^2} = \lim_{N\to\infty}\frac{T_{ON}^2N(V_{in})^2}{4CL}\left(\sum_1^N\frac{1}{V_{out,k-1}}\right)^2 \qquad (22)$$

This limit shows that the efficiency can be potentially increased with the parameters **TON**, **N**, **Vin**, **1/C** and **1/L**.

The given duty cycle operated the device in buck conversion mode. In ideal case, the efficiency keeps asymptotically increasing under 100%. While in real applications, the absolute voltage ratings of the components in addition to the power consumption limit the output voltage and thus the efficiency. For this reason, a comparison can be made between the simulations and experiments on our prototype by evaluating the efficiency after the startup time of the converter (the time needed to reach the maximum output voltage). Table 1 shows the difference between simulation and experimental results.

	DC Startup time	DC efficiency	AC Startup time	AC efficiency
Simulation	∞	73 %	∞	60 %
Experiment	60 ms	67 %	200 ms	43.54 %

Table 1. A comparison between the simulation of the buck-boost converter analytical model, and the experiment made on the prototype produced in the lab.

2.5.   Power consumption model

Low power energy harvesting requires efficient circuitry to reduce the power loss as much as possible, due to the small amount of energy extracted by the harvester. For this purpose, we evaluate the power consumption of different components in the converter that is meant to be used. And optimization solutions can be built upon the results of this model.

The topology used in this work is a non-inverting buck-boost converter, with three ADG801 low power switches [26][27]. Two type of losses can be found in these switches, first is in the switching time that can introduce unwanted transient behaviors, and the other is in the ON resistance. The switching time according to the datasheet is 33ns and compared to T_{ON} which is 25µs we can ignore its effect. We can also find the ON resistance around 0.5Ω in the room temperature.
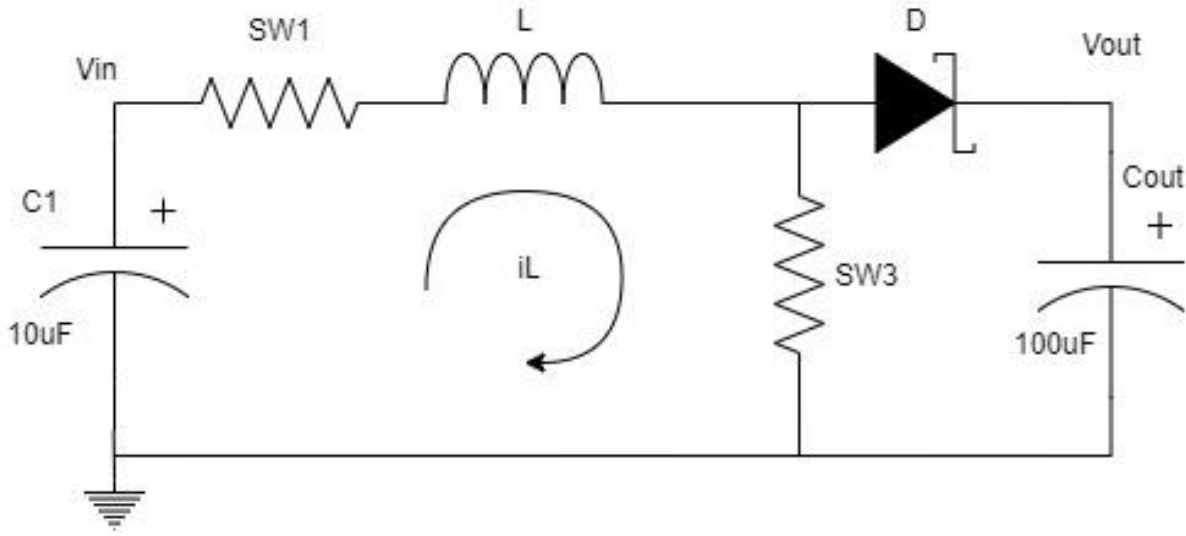
Figure 16. The current loop during ON time.

- At $t \leq T_{ON}$:

During the transient phase, Vout will start from zero and the diode D will be forward biased, thus the capacitor Cout is charging through a small portion of the input voltage. But in this study, we consider the system in the permanent phase where Vout>>0 allowing the diode D to be reverse biased, and then we end up with a single ON loop (see Figure 16).

Due to the presence of 2 resistances the voltage across the inductor $V_{L,k}$ won't be equal to $V_{in,k}$ and there will be a voltage drop equal to $2V_{sw,k}$.

The inductor current $i_{L,k}$ is assumed linear and equal to:

$$i_{L,k}(t) = \frac{V_{L,k}}{L}t \tag{23}$$

Where:

$$V_{L,k} = V_{in,k} - 2V_{sw,k} \tag{24}$$

So we will assume that $V_{sw,k}$ is constant and equal to:

$$V_{sw,k} = R_{sw}I_{avg,k} \tag{25}$$

Where:

$$I_{avg,k} = \frac{1}{T_{ON}}\int_0^{T_{ON}} \frac{V_{L,k}}{L}t\,dt = \frac{1}{T_{ON}}\left(\frac{V_{L,k}}{2L}T_{ON}{}^2\right) = \frac{I_{p,k}}{2} \tag{26}$$

And $I_{p,k}$ becomes:

$$I_{p,k} = \frac{V_{L,k}}{L}T_{ON} = \frac{V_{in,k}T_{ON}}{L + R_{sw}T_{ON}} \tag{27}$$

Thus, the energy stored in the inductor:

$$E_{l,k} = \frac{L}{2}\left(\frac{T_{ON}V_{in,k}}{L + R_{sw}T_{ON}}\right)^2 \tag{28}$$

And the power dissipated in the Switches:

$$P_{sw,k}(t) = 2V_{sw,k}i_{L,k}(t) \tag{29}$$
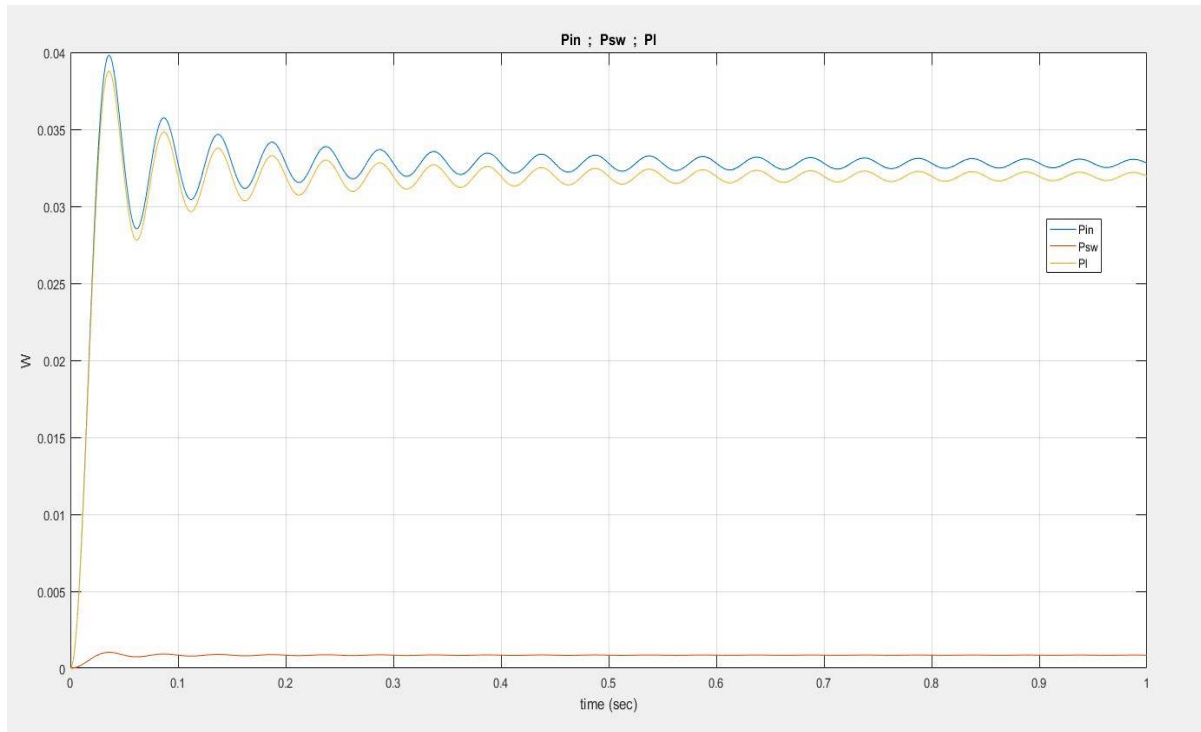
Figure 17. Plot showing the power consumed by different components of the circuit during ON time.

$$P_{sw_{avg},k} = \frac{1}{T_{ON}} \int_0^{T_{ON}} \frac{2V_{sw,k}V_{L,k}}{L} t\, dt = 2R_{sw}I_{avg,k}^2$$

And by analogy the average input power to the circuit is:

$$P_{in\_avg,k} = V_{in,k}I_{avg,k} \tag{30}$$

The plot in Figure 17 shows the power in different components of the circuit during the ON loop.

- At $T_{ON} < t \leq T_{CK}$

During the OFF loop, a single switch is present what gives a drop of $V_{sw,k}$ (see Figure 18). The inductor current takes the following value:
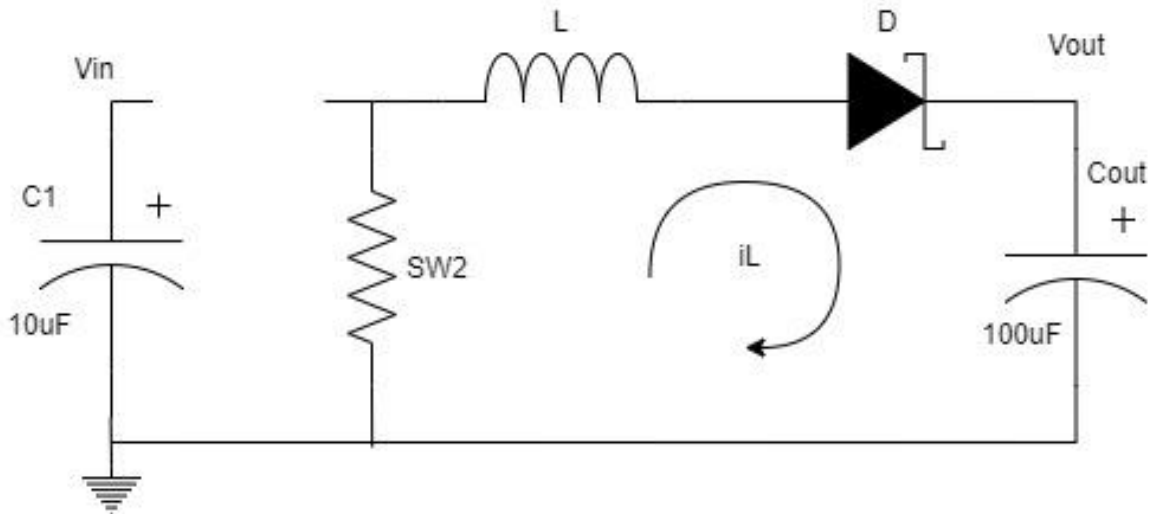
Figure 18. The current loop during OFF time.

$$i_{L,k}(t) = \begin{cases} I_{p,k} - \dfrac{V_{L,k}}{L}t & t \leq T_D \\ \\ 0 & t > T_D \end{cases} \tag{31}$$

Where:

$$V_{L,k} = V_{out,k} + V_{D,k} + V_{sw,k}$$

I_L is also linear here so we assume that $V_{D,k}$ and $V_{sw,k}$ are constant and dependent of $I_{avg,k}$.

$$V_{D,k} = V_T ln\left(1 + \frac{I_{avg,k}}{I_s}\right) \tag{32}$$

Where V_T is the thermal voltage and I_s is the reverse bias current (leakage current).

The power dissipated in the diode is:

$$P_{D,k}(t) = V_{D,k} i_{L,k}(t)$$
$$P_{D\_avg,k} = V_{D,k} I_{avg,k}$$

(33)

And the power dissipated in the switch is:

$$P_{sw\_avg,k} = V_{sw,k} I_{avg,k} = R_{sw,k} I_{avg,k}^2$$

(34)

The plot in Figure 19 shows the power consumption during T_{OFF} for the different components. It is remarkable that the diode consumes much more power than the switches resistance, what gives a space to use different techniques to reduce this consumption.
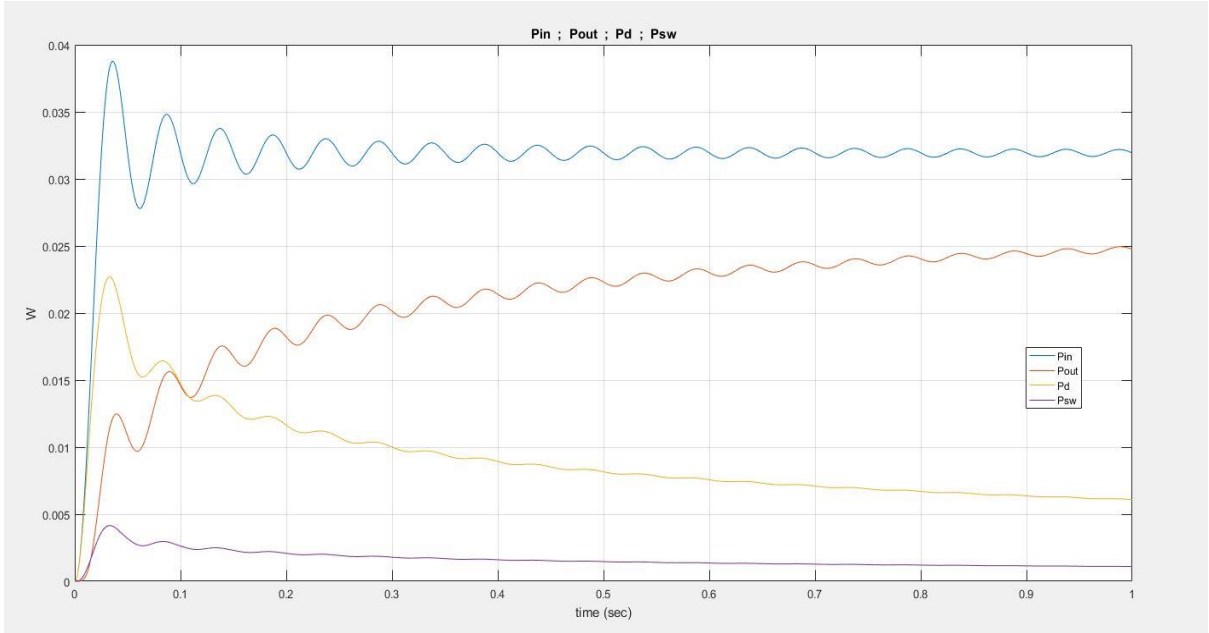
Figure 19. Plot showing the power consumption in different components during OFF time.

2.6.   Power optimization

The previous simulation shows clearly that the most power dissipated in the converter's circuit is in the diode, and that considering a Schottky diode which has a low voltage drop that normal PN diodes. This is true for different DC/DC converters configurations (Buck, Boost, etc..).
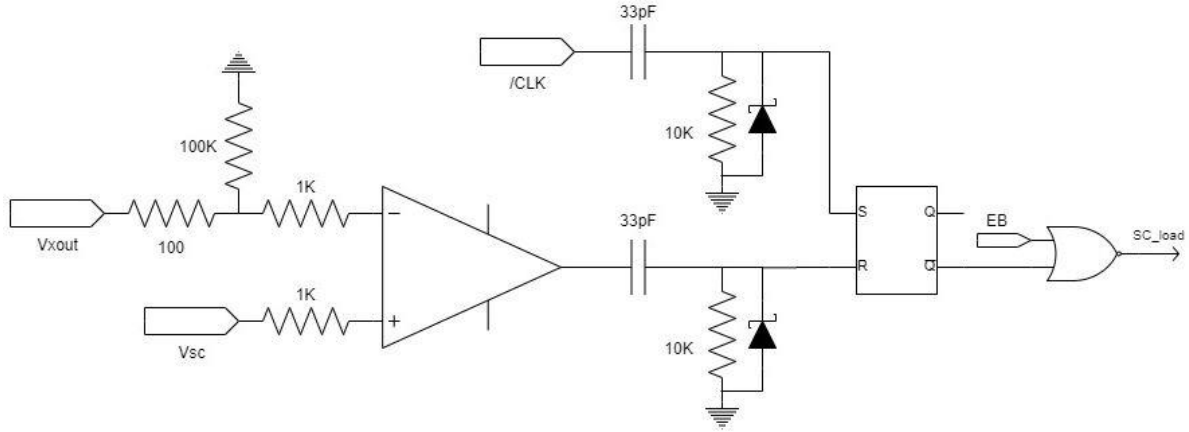
Figure 20. The used current direction sensing circuit.

Other alternatives for the diode were investigated, naming a method that uses a MOSFET switch driven by a current direction sensing circuit as shown in Figure 20. The nodes Vxout and Vsc are respectively sensing points on the anode and cathode of the active diode. The comparator senses the current direction and gives a signal that is high-pass filtered to enter an RS latch in synchronization with the PWM signal that ensures that the diode is not forward biased during the ON time, and therefore it can reduce the transient behavior of the converter when Vout starts from 0.

Another alternative is to use an integrated circuit that is designed to operate as a driver for the active diode such as TI LM74810Q. These ICs deal with some unwanted behaviors like the reverse polarity currents, and include integrated protection for the MOSFET that is used as a switch.

Either way the diode must be replaced with a MOSFET due to the high voltage drop across the diode in forward bias, and the flexibility of the MOSFETs DS resistance that can dictate the forward voltage drop. The bridge rectifier is another source of efficiency loss and can be considered a part of the AC/DC converter. Since the conventional rectifiers use diodes, the efficient design has to rely on MOSFETs. This substitution was investigated in literature [28]–[30] where different methods have been proposed. The 2 main methods consist of driving the MOSFETs from the opposing input node, or to drive them using comparators as current direction sensors.

In our work a configuration was adopted for the full wave bridge rectifier that is shown in Figure 21. Each side of the input is connected to a P-channel and an N-channel MOSFETS respectively substituting the in and out diodes, and the gates are fed by the opposite polarity node.
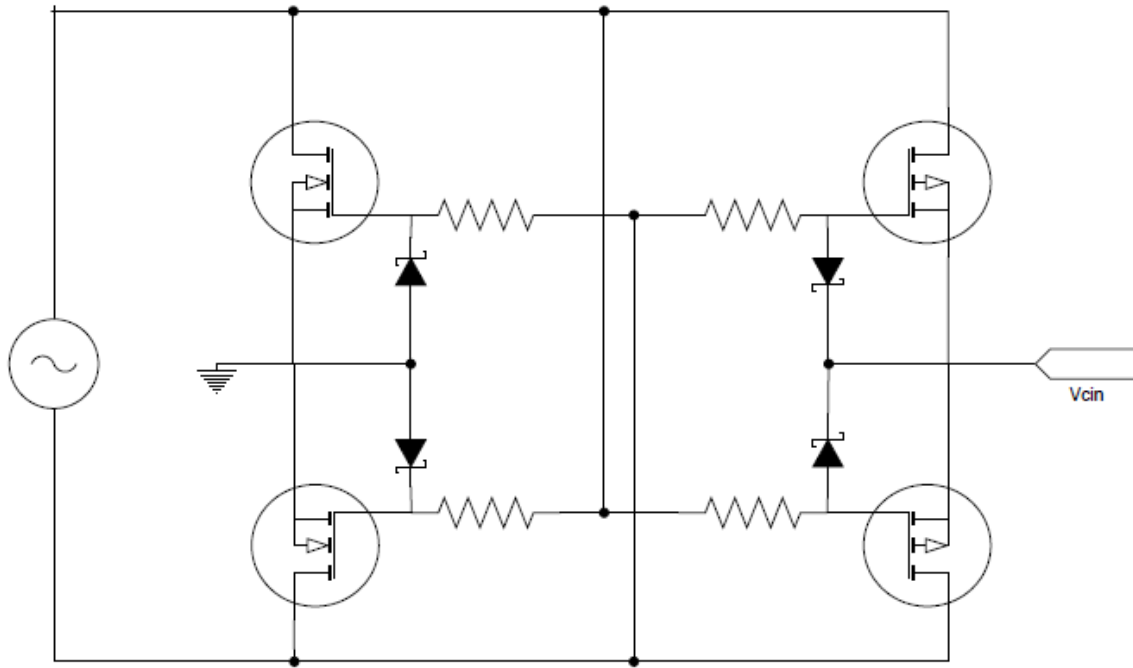
Figure 21. The architecture of the MOSFET full wave rectifier.

Zener diodes were placed for the protection of the gates, and high value resistors are also used to prevent resonance between the harvester's inductor and the internal capacitance of the MOSFETs.

2.7.   Conclusion

In this chapter, the importance of switching converters in the energy harvesting domain was highlighted. Different configurations of the converters were explained, with the characteristics and advantages of each, in addition to the techniques used to integrate these converters in the energy harvesting interface circuits.

The developed mathematical models allowed to simulate the behavior of different components within the converter's circuit, and then locate the sources of power loss with their respective contributions, what allows to deal with these components and find solution to substitute them and ensure a more efficient performance for the converters to be used in low power applications. The results of this chapter were built on to develop prototypes for a novel wind energy harvester that is mentioned in detail in chapter 5.

Chapter 3.   Maximum Power Point Tracking

3.1.   Introduction

In power systems, the most important characteristic is the efficiency, and this does not exclude energy harvester. Furthermore, it is crucial to maintain the highest efficiency possible with energy harvesting system due to the fact that the weather variations are random and power down times are not predictable, what requires the extraction of the most available power possible. Maximum Power Point Tracking algorithms are commonly used to optimize the power transferred from the harvester to the interface electronic system, and it functions using the monitor and control strategy. The power extracted from the harvester is monitored, and the control is done through control variables that affect the amount of power transferred. The characteristics of energy harvesters show an optimal power point that the system can operate at, given all different weather conditions. Exploiting this fact, many algorithms have been developed and used in the literature, ranging from very simple and inaccurate to complex and accurate algorithms. In this chapter we are listing a number of the commonly used MPPT algorithms with a brief explanation and discussion of the advantages and disadvantages, as well as the implementation methods that can be used. MPPT algorithms that are proposed and implemented in the laboratory are also presented, with simulations and experiments that were made to test the validity and the possibility of the integration of these algorithms in our energy harvesting system.

3.2.   Control variables

Control variables are the element defines the electric characteristics of every type of harvesters. The power produced from energy harvesters is a factor of many variables including the weather conditions, the mechanical elements and the electrical elements. The relation is not easily defined due to the high variability in all these elements, for instance different loads require imply a different behavior for the harvester and therefore a different produced power. An interesting characteristic for enemy harvesters is that an optimal output power exists under all weather

conditions, the problem is that the control variables need to be tuned accurately to operate in that Maximum Power Point MPP.

For wind turbines, control variables consist of blades pitch angle for the mechanical side, and rotor speed for the electrical side. While DC output voltage is the control variable for PV cells and thermal harvesters, and AC voltage is the control variable for Vibration based piezoelectric harvesters. Figure 22(a) shows the output power variation against the rotor speed for a wind turbine under different wind conditions [31]. Our work relies on a wind flattering energy harvester, where the load resistance is used as a control variable, the harvester's power characteristics are shown in Figure 22(b).

(a)   (b)
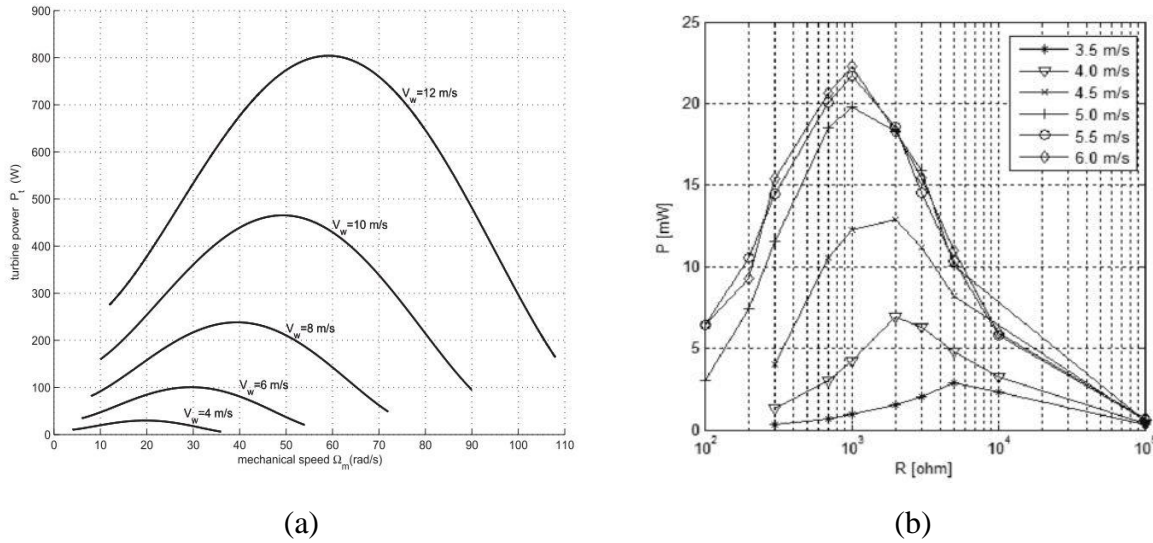
Figure 22. The variation of the output power of the harvesters affected by the changes of control variables. (a) for a wind turbine [31], (b) FLEHAP harvester [21].

The control strategy used in energy harvesting is mainly to design a switching converter that can be controlled through a PWM signal, and changing the duty cycle of that PWM will trigger a variation in the control variable associated with the harvester. This is done using a Maximum Power Point Tracking algorithm MPPT.

3.3. State of the art in MPPT algorithms

MPPT algorithm have been the main power trackers that energy harvesting systems rely on. A lot of different algorithms and methods were developed, meeting many system requirements and having their own advantages and disadvantages. Below, few popular algorithms are briefly described including Perturb and Observe P&O, Incremental Conductance INC, Lookup Tables, Fuzzy Logic and Neural Networks.

3.3.1 P&O

Among all the Hill Climb Search algorithms, the Perturb and Observe (P&O) happens to be the one that does not require any prior knowledge of the system and is absolutely independent of the harvester, generator and weather conditions. Thus, the P&O control naturally is the most popular choice for MPPT. [32]

The P&O MPPT algorithm is mostly used, due to its ease of implementation. It is based on the following criterion: if the input resistance of the interface circuit is perturbed in a given direction and if the power drawn from the harvester increases, this means that the operating point has moved toward the MPP and, therefore, the equivalent resistance must be further perturbed in the same direction. Otherwise, if the power drawn from the harvester decreases, the operating point has moved away from the MPP and, therefore, the direction of the equivalent resistance perturbation must be reversed.[33][34]

(a)   (b)
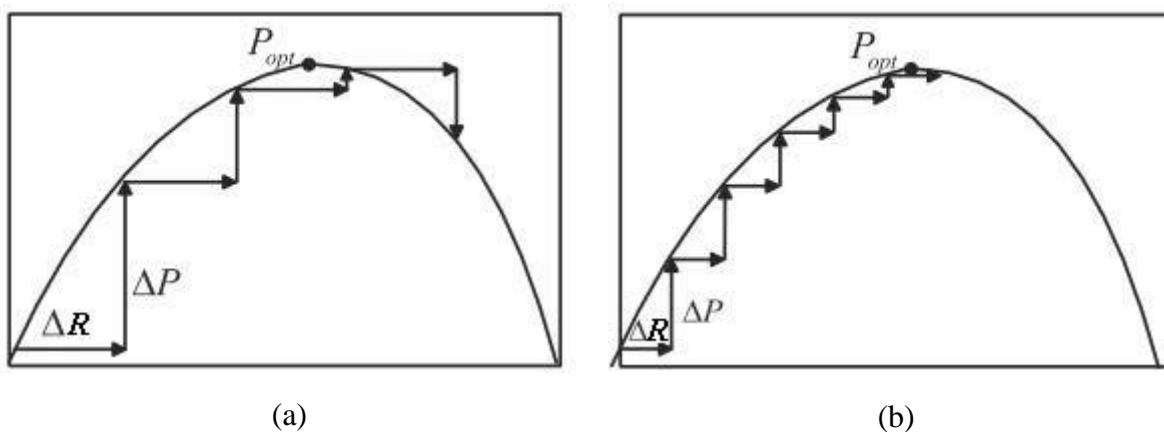
Figure 23. The steps of the P&O algorithm following the maximum point (a) large step size, (b) small step size [32].

As shown in Figure 23(a), a larger step size increases the speed of convergence but deteriorates the efficiency of the MPPT. Oscillations are an unavoidable attribute of the HCS control it is due

to the fact that HCS control cannot stop at Popt. Of course a smaller step size will boost the efficiency, but the controller will become very slow and may be deemed as incapable specially under rapidly varying wind conditions (Figure 23(b)). Therefore, in the normal HCS control there always exists a tradeoff between the tracking speed and the control efficiency.

In normal P&O control method the direction i.e. the sign of the next perturbation is decided by the increase or decrease in power due to the previous perturbation. Since the algorithm is blind to the atmospheric changes therefore the control law can be misleading in changing wind conditions as the sign might get dictated by the change in wind rather than the applied perturbation. This wrong decision leads to the failure in keeping track of MPP and the HCS control moves downhill. In
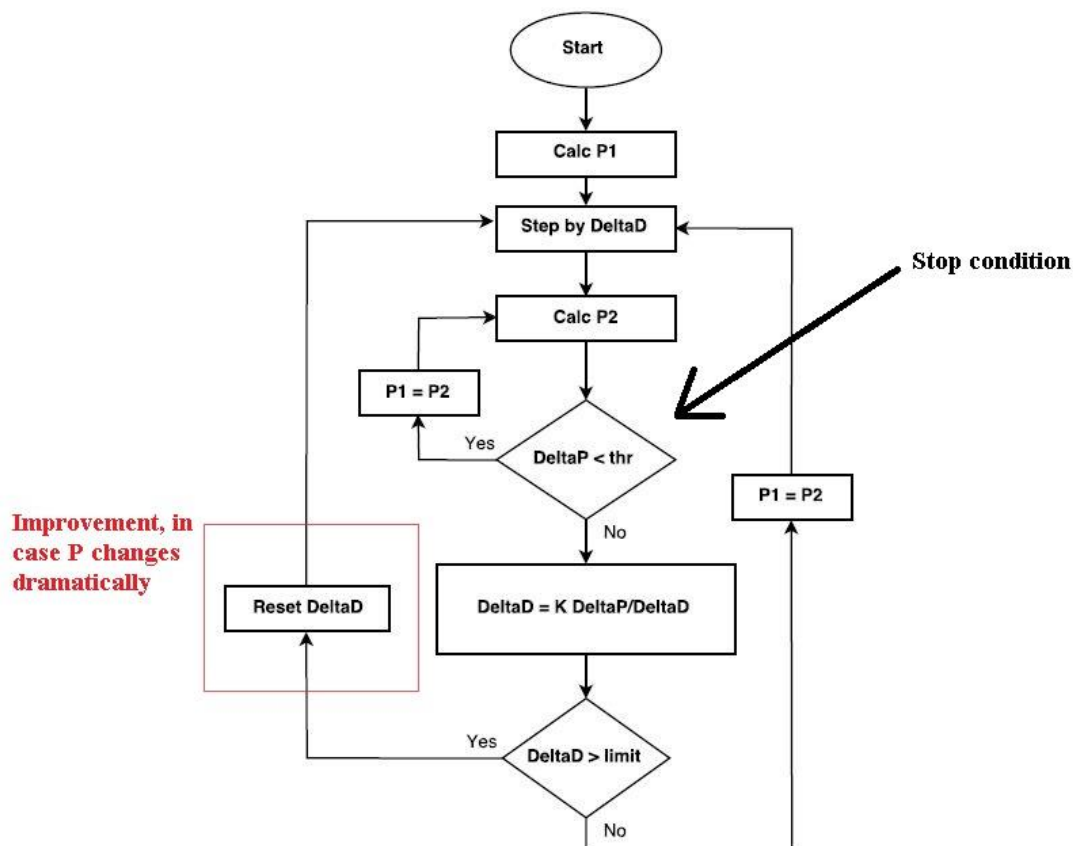
Figure 24. Flow chart of the modified P&O algorithm.

addition, a drawback of P&O MPPT technique is that, at steady state, the operating point oscillates around the MPP giving rise to the waste of some amount of available energy.

Several improvements of the P&O algorithm have been proposed in order to reduce the number of oscillations around the MPP in steady state. Modified MPPT algorithms with variable step size have been proposed for some techniques especially the modified Perturb and Observe method, in which the step size is automatically adapted according to the inherent harvester characteristics. Figure 24 shows the flow chart for a modified P&O algorithm where the step size ΔD is updated with a proportional value of the power gradient in order to follow the general power flow and not overshoot. By nature, the algorithm has a stop condition whenever the power gradient is null, but it is recommended to introduce a threshold to meet this condition.

3.3.2 Incremental Conductance INC

This algorithm is independent of requirement of sensors and specifications of turbine and generator, which improves the reliability and reduces the cost of the system [38,39,105,106]. The turbine output power can be represented as a function of DC link voltage (Vdc) [105,106]. There exists also an optimum Vdc (Vref) which maximizes output power of the generator by analyzing immediately using INC algorithm. As the power is equal to the product of current (Idc) and voltage (Vdc), the calculation of this slope is given by:

$$\frac{dP_{dc}}{dV_{dc}} = \frac{d(vi)_{dc}}{dV_{dc}} = i_{dc} + v_{dc}\frac{di_{dc}}{dv_{dc}} \tag{35}$$

The expansion of this derivative for MPP is given by:

$$\frac{i_{dc}}{v_{dc}} + \frac{di_{dc}}{dv_{dc}} = 0 \tag{36}$$

The basic principle is defined as the tangent slope $\left(i/v + di/dv\right)$ of power–voltage characteristic should be zero at MPP, positive on the left side, and negative on the right side of MPP as described in Figure 25. The above equations signify that instead of observing for weather dependent parameters like speed and direction of wind, the MPP can be tracked by looking for output power of the rectifier. The modified INC algorithm improves the performance of the INC algorithm by

considering a variable step for Vdc variations. It automatically adjusts the step size to track the MPP, which leads to enhancement of system accuracy and convergence speed. The implementation of Model Predictive control in wind turbine MPPT controller improves speed and reliability, and also mitigates the problem of oscillations around MPP. The range of Vdc variations (ΔVdc) has been limited, which changes depending on system design parameters and size of
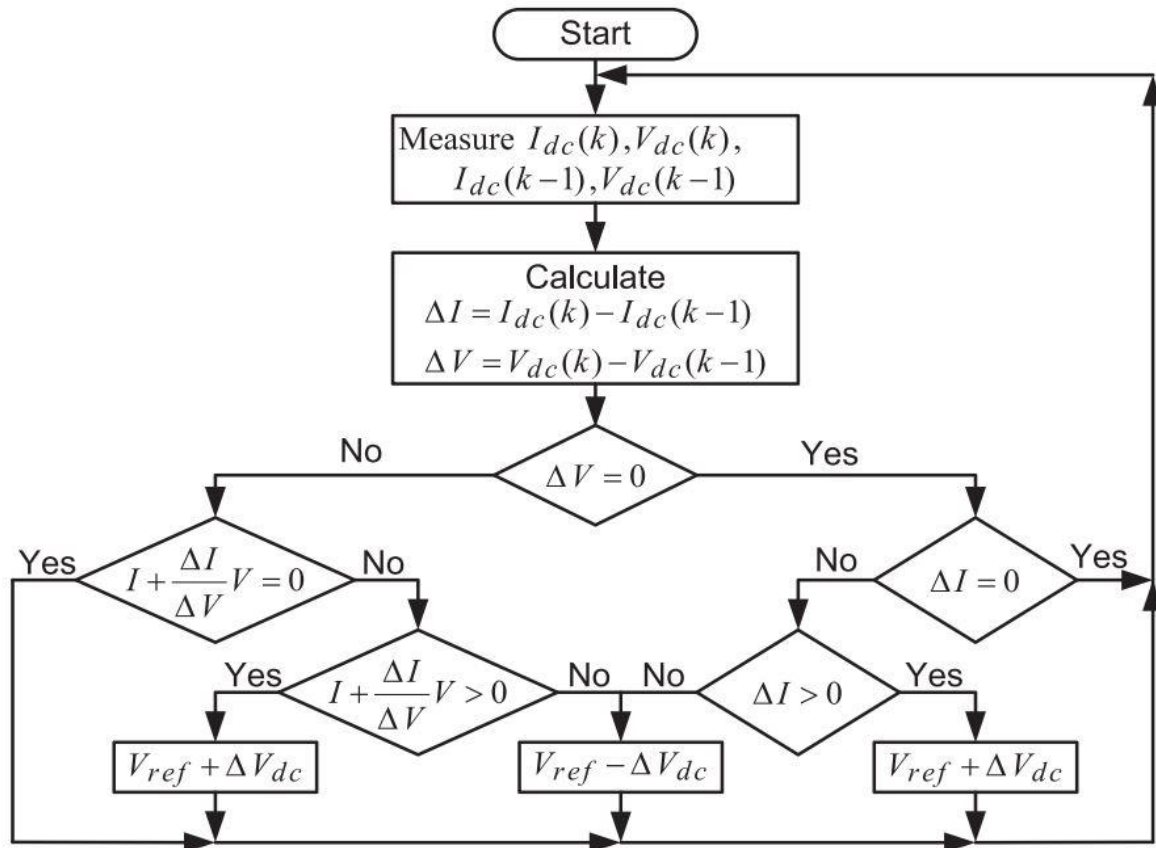
Figure 25. Flow chart of the INC algorithm.

generator. Introducing variable steps in this algorithm causes the operating point to reach the peak power more rapidly and reduction of power fluctuation around MPP.[35]

3.3.3 Lookup tables

This algorithm requires the knowledge of wind turbine's maximum power curve, which is tracked by its control variables. The maximum power curves can be obtained through simulations or
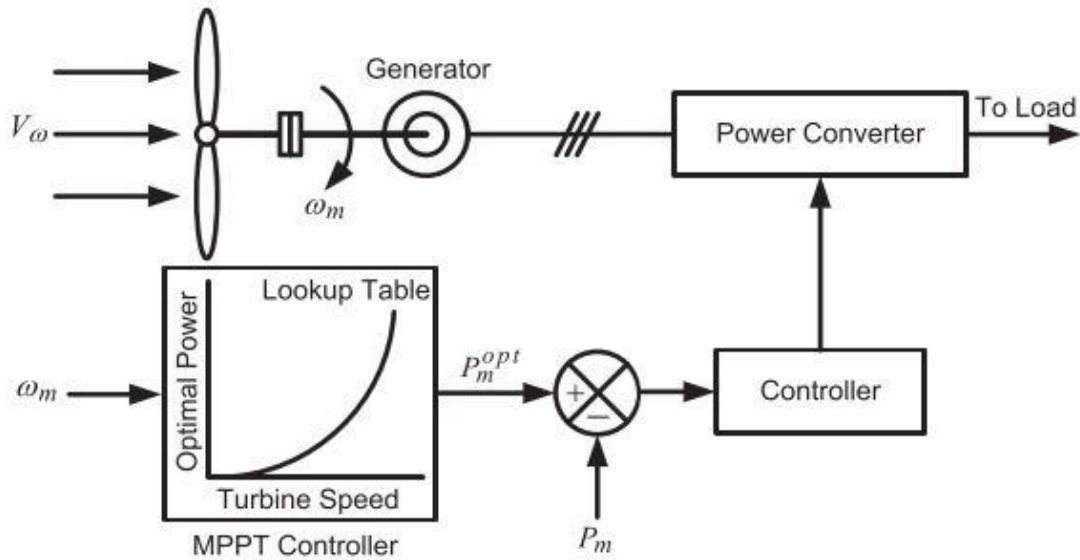
Figure 26. Control strategy using lookup tables [35].

experimental tests on individual wind turbines. The integrated memory records the system max-power points and the corresponding control variables at different operating conditions. Depending on the system structure, the control variables of a wind power generation system may include the inverter output current demand for output power control, generator excitation current for generator output voltage control, switching converter input equivalent resistance etc. If there is only one control variable for output power regulation and Vdc is the only index referring to operating condition as in the case of most small variable speed wind turbines, a lookup table can be used to construct the memory [36]. Figure 26 shows the block diagram of a Power Signal Feedback control, where wind speed or the turbine speed is used as the input. [37].

3.3.4 Fuzzy logic

Many control strategies have been proposed that use the Fuzzy Logic Control (FLC) for MPPT applications either independently or along with other methods. The main advantage of such controllers is that controller parameters can be changed very quickly in response to changes in the
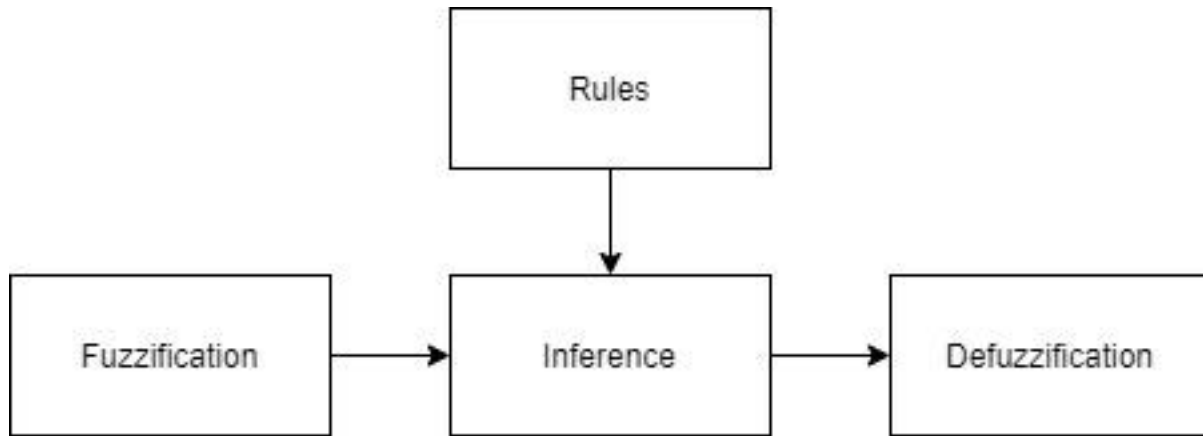
Figure 27. Followed steps in the Fuzzy Logic algorithm.

system dynamics without parameter estimation [35]. The algorithm consists of three main steps: Fuzzification, Inference and Defuzzification (Figure 27), where the inference is done following a rule table that relates membership functions with different fuzzy subsets that are defined for the problem [38]. When the climatic condition changes, the performance of a fuzzy based MPPT algorithm is strong, however, their strength depends a lot on the knowledge of the user in choosing the appropriate error, levels of membership functions and selection of rule base. In addition, this algorithm requires relatively high computational power and a relatively big memory what also poses limitations in its implementation, especially for low power application where limitations are imposed.

3.3.5 Neural Network

Similar to Fuzzy logic, the neural network (NN) has become popular and expanded with the development in soft computing technology [39]. The architecture of a Neural Network consists of three layers: input, hidden, and output layers and the number of nodes in each layer vary and are user dependent as shown in Figure 28. The input variables can be pitch angle, terminal voltage, output torque, wind speed, rotor speed, etc. or any combination of these variables. The output is generally a reference signal like reference power, rotor speed, reference torque, etc. that is used to drive the power electronic circuit of wind turbine close to the MPP.
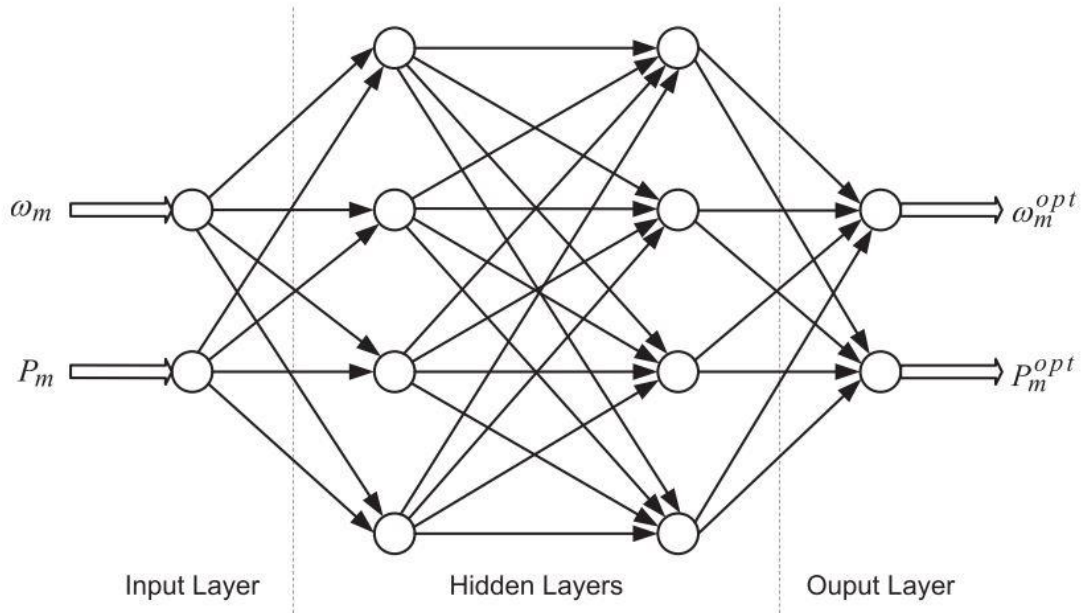
Figure 28. Structure of the artificial neural network [35].

The convergence of operating point to the peak point depends on the weights assigned to the layers, the type of algorithm used by the hidden layer and the training given to the neural network for a particular system for different input–output patterns. Figure 28shows NN-based [40][41] wind speed sensorless MPPT algorithm for wind turbines, in which it uses the rotor speed (ωm) and the output power (Pm) of the turbine as input variables. Due to the inertia of the system, rotor speed cannot change suddenly. Therefore, output of the NN is required to change gradually, from which the optimal rotor speed, $\omega_m{}^{opt}$ for the speed control mode is obtained and then it is set to control the generator to obtain the optimum power, $P_m{}^{opt}$ for the power control mode. From the above process, ω_m and Pm can be used to directly obtain ωoptm and $P_m{}^{opt}$. Such relationships are learned by the NN using the training data. The above procedure decreases the speed response time, so the system settles down to the steady state faster than the power control mode and provide a smoother power transition in the speed control mode during wind speed variations. Therefore, this MPPT control represents a better tradeoff in terms of the system dynamic speed and power responses.

3.4.   Algorithm implementation

The MPPT algorithm is usually implemented in the interface circuit for energy harvesters either by designing a dedicated circuit that performs the needed task, or by using a microcontroller. Both solutions have advantages and disadvantages mainly related to the overall efficiency.

The dedicated circuits differ depending on the task to perform, but they all follow a general flow illustrated in Figure 29. The circuit consists of sensing points that are located throughout the system and these sensor points monitor different variables that play into the MPPT decision, for instance the input power. The signals are fed either to a comparator block or a controller that take decisions on whether to increase or decrease the excitation on the control variables, the excitation that is
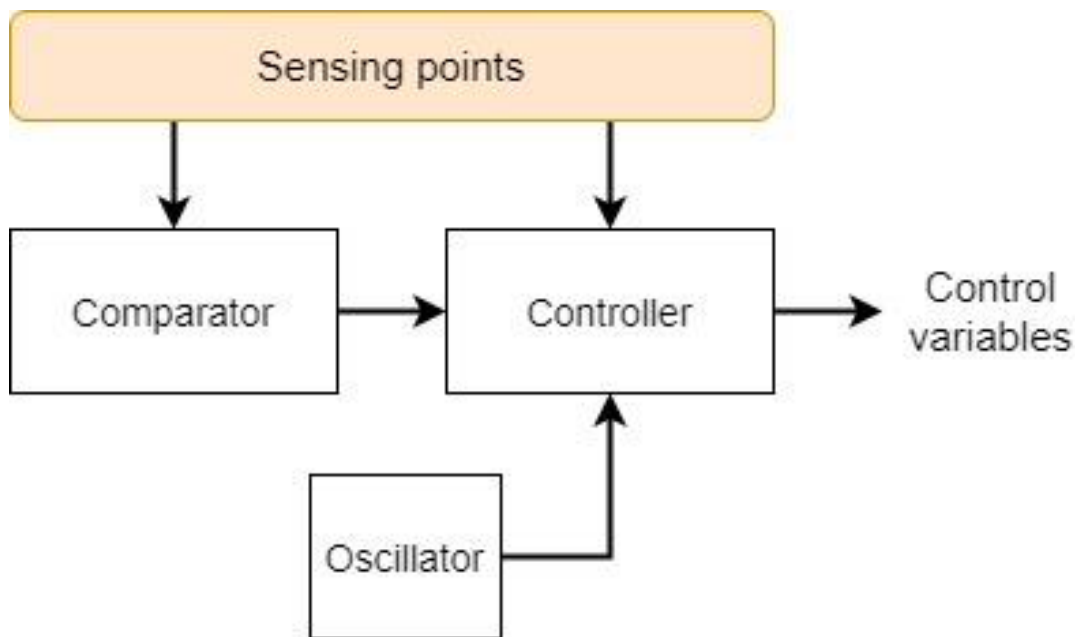
Figure 29. Block diagram of the dedicated circuit that performs the MPPT control.

usually in form of a PWM signal is generated using an oscillator [31], [42]–[46].

Figure 30 illustrates the microcontroller integration in the system where a power source is needed to provide the MCU with enough voltage and current to ensure a continuous operation, and it usually has to be allocated from within the harvester circuit. Different sensing points send their signals to input points in the MCU, and then the uploaded algorithm makes decisions to excite the control variables.
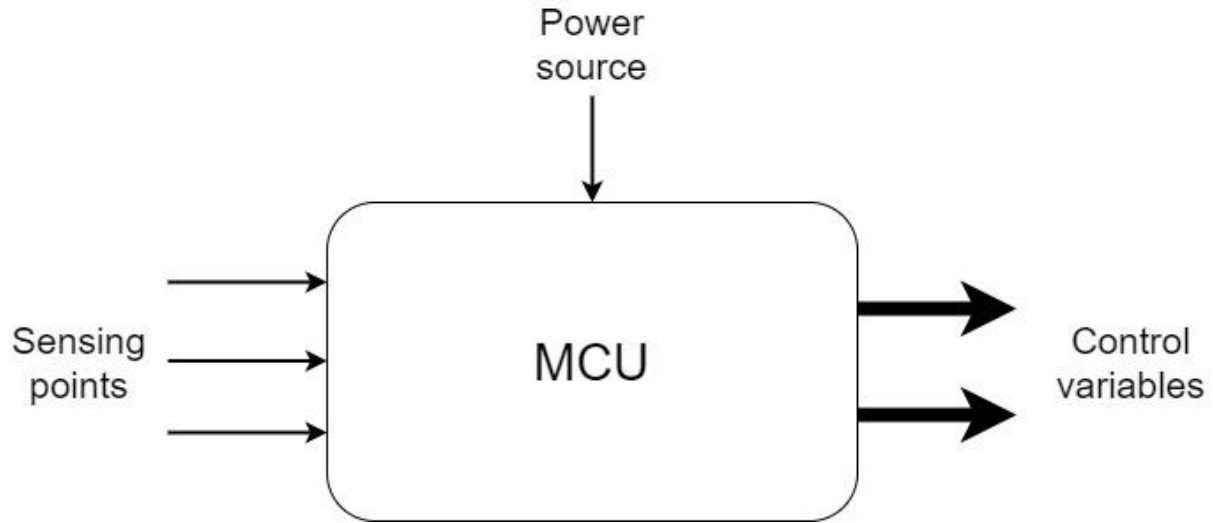
Figure 30. The usage context of an MCU.

The advantages and disadvantages of these solutions are shown in Table 2. The power consumption in the dedicated circuit is lower than MCU, and the algorithm runs faster, while sacrificing complexity, accuracy and non-flexibility. The other solution provides flexibility in writing and tuning the algorithm, this is useful in case of prototyping for the benefits of making

	Dedicated circuit	Microcontroller
Power consumption	Low	High
Speed	High	Tradeoff with power
Complexity	High	Low
Flexibility	Cannot be changed	flexible
Additional Utilities	-	-ADC synchronization -Debugging and operation monitoring -Serial communication

Table 2. The differences the dedicated circuit and the MCU for the implementation of MPPT control.

different decisions after seeing experiment results and circumstances. It is also a simpler solution in terms of producing the circuit and implementing the algorithm. It further allows for more advanced exploits of the MCU functions such as synchronizing the reading of the Analog-Digital Converter (ADC). Other utilities it provides are the ability to monitor different variables what allows for easy data collection and the possibility to debug the algorithm, in addition for the serial communication with other devices on board the target sensor nodes that can potentially open different opportunities for power management.

3.5.   MPPT Simulation

The P&O method is one of the simplest methods used for the maximum power tracking. The advantages it offers are low computational requirements and low cost due to the independence on mechanical sensors and measurements. The input resistance of the switching converter follows the switching duty cycle, and by applying small perturbations to it, the received power changes and therefore it could be controlled to reach the MPP. In Figure 31 a MATLAB simulation of the

(a)   (b)
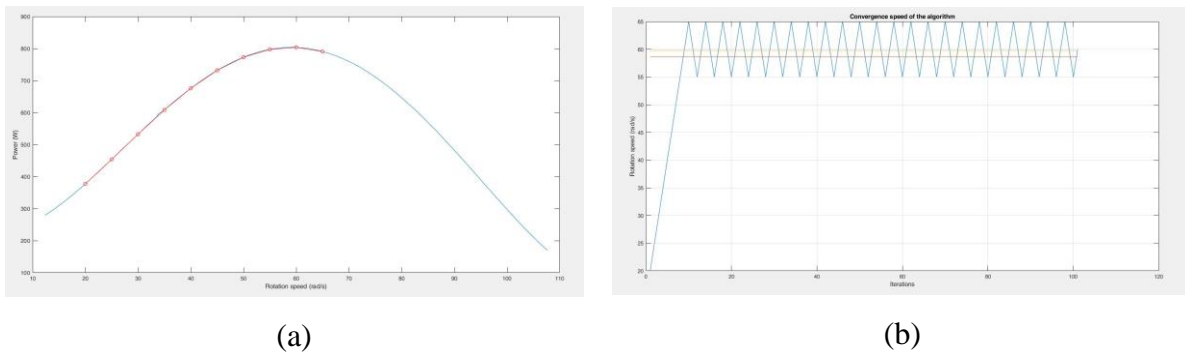
Figure 31. The fixed step P&O algorithm with a step of 5. (a) steps following the power curve, (b) control variable perturbations.

algorithm where the first plot shows the power curve with the algorithm tracking points, and the second plot shows the perturbation of the control variable in every iteration with the lines indicating the desired MPP margin. The used data is an interpolation of the plots from Figure 22(a).

 Using the P&O algorithm with fixed step shows a waste of efficiency around the MPP due to the oscillations and this where the benefits of the modified algorithm take place.

The next simulations in Figure 32 show the modified P&O algorithm where an adaptive step is used instead of the fixed step, the adaptive step is proportional to the discrete gradient of the power (see Figure 24).

(a)

(b)

(c)

(d)

(e)

(f)
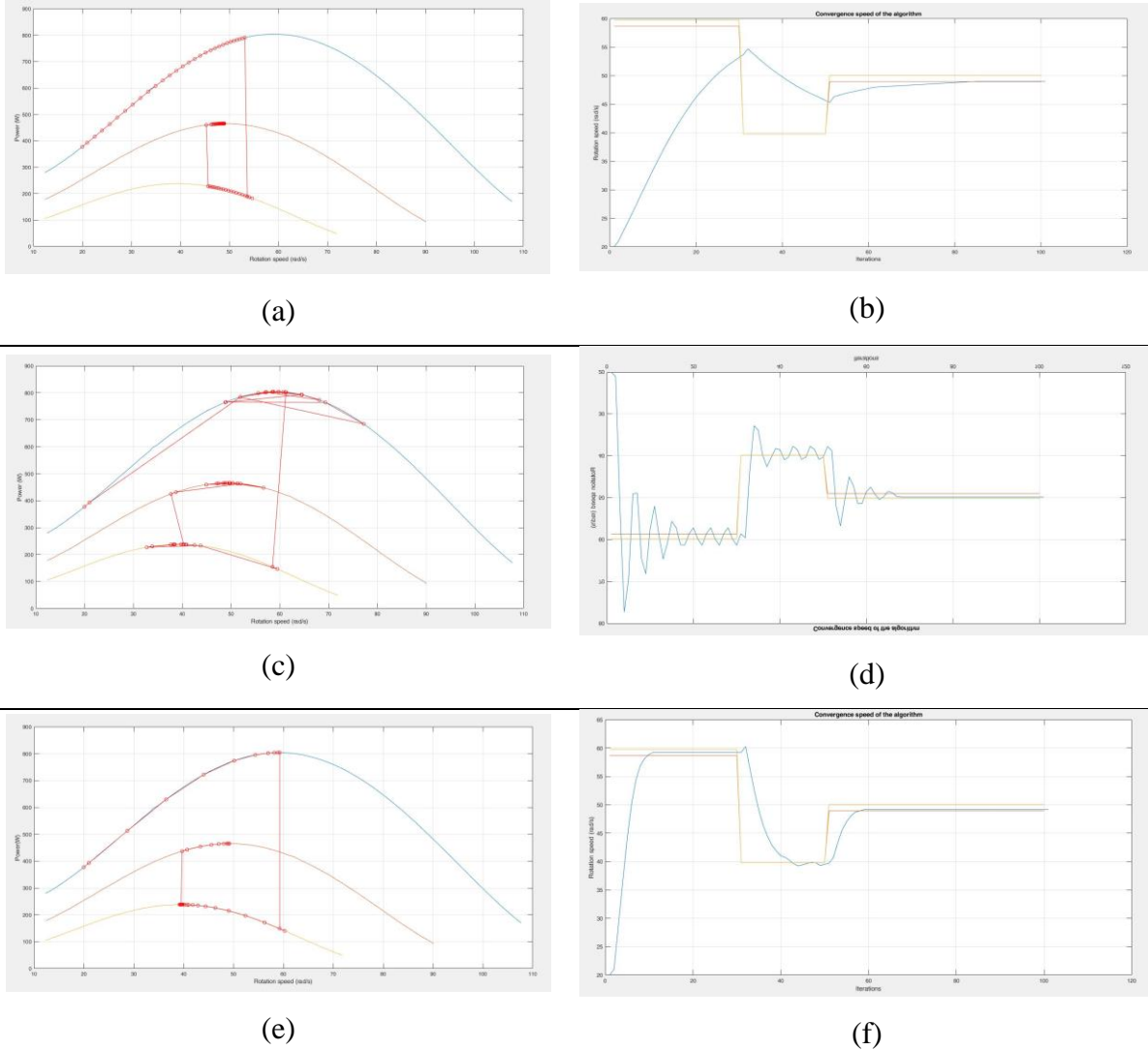
Figure 32. Comparison between the modified P&O performance for K = 0.1, 0.5, and 2 respectively (a),(e),(c). And the corresponding control variable perturbation on the right side plots (b),(f),(d) respectively.

A good tuning of the variable K plays a role in the convergence of the algorithm, as seen in Figure 32(b,d,f), a tradeoff exists between the speed and stability, with a low K value (K=0.1) the algorithm converges but slowly (>30 iterations), with a high value (K=2) the algorithm is fast but it oscillates around the MPP, while an fairly tuned value (K=0.5) a good response can be obtained (≈ 10 iterations).
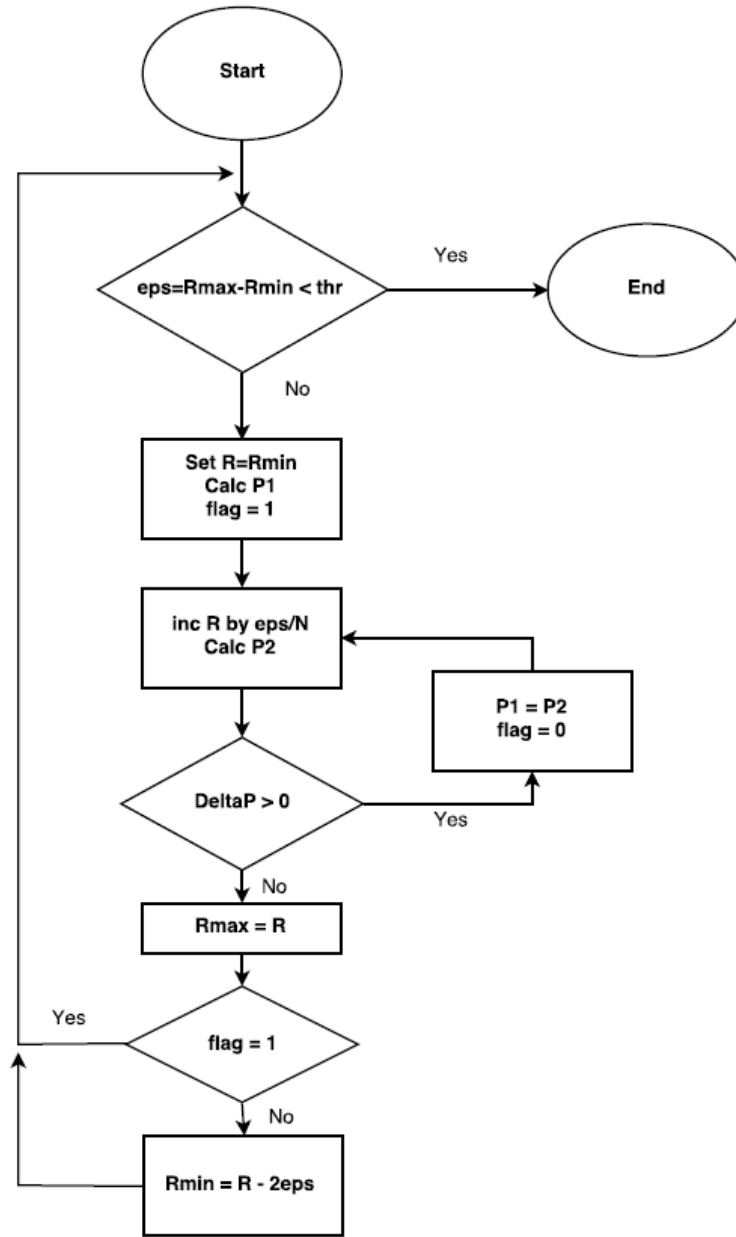
Figure 33. The proposed recursive algorithm.

An algorithm was proposed (Figure 33), and it works in a recursive way where an interval is specified and separated into N sub-intervals, the control variable is incremented by the length of the sub-interval and whenever the power sign changes, the sub-interval is considered the new interval for another iteration, and thus the MPP is truncated on each iteration until the stop condition is met. However, this algorithm also needs tuning of the variable N, but it does not show a big advantage compared to the modified P&O. Figure 34 shows the conversion speed for N=8, and it is roughly around 20 iterations.

(a)

(b)
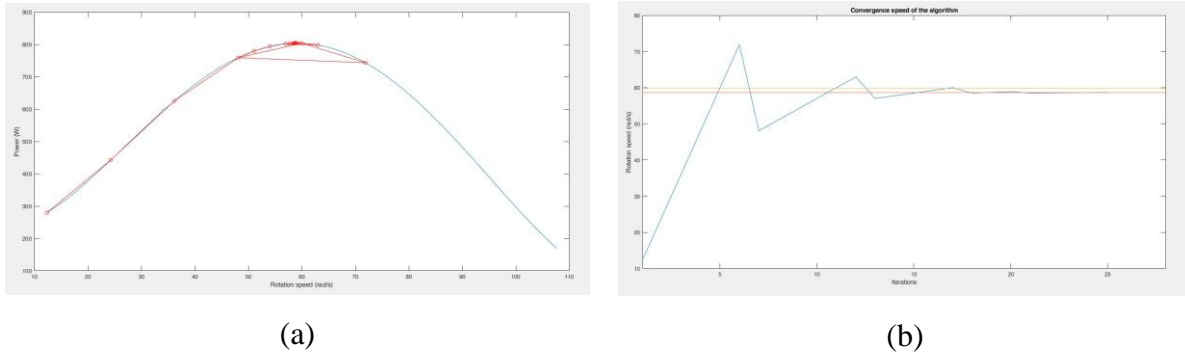
Figure 34.Simulation result of the recursive algorithm for N=8. (a) steps following the power curve, (b) control variable perturbations.

- **Important notes to consider:**

The P&O algorithm is not a general solution for the optimization of the Power transfer; it is instead fitted to work with certain applications in specific conditions. However, in order to keep the algorithm stable and avoid any divergence or abnormality we must specify conditions for each variable, and switch to a defined state or do a soft reset in case of abnormality.

The main variable that affecting the P&O algorithm is ΔD which is the duty cycle change that is effecting the control variables (R is our case), and some limits must be specified to prevent the wrong behaviors. First, any system cannot work in all weather conditions, and therefore an upper
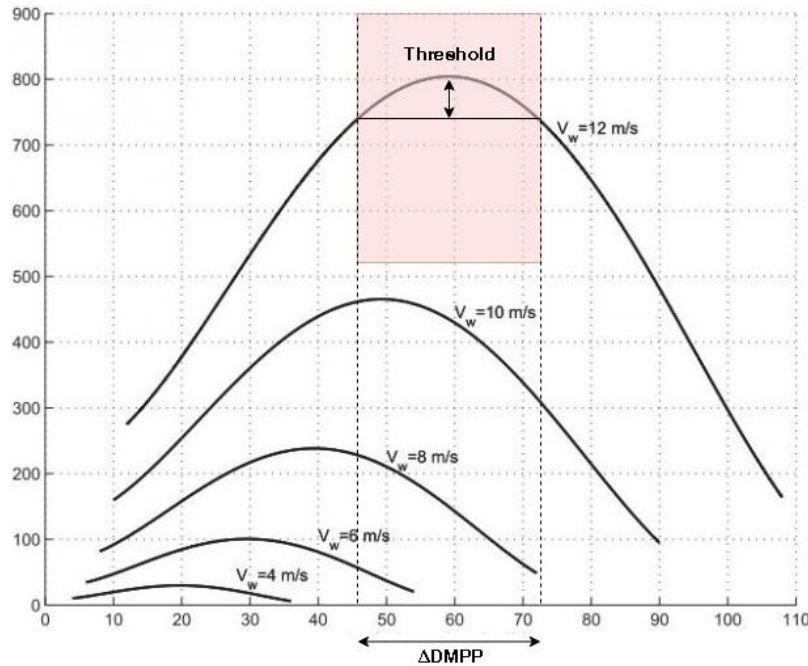
Figure 35. The range of the MPP zone considering a fixed power threshold.

and lower limit have to be specified. Second, reaching a null slope is not practical so it is advised to set a threshold for ΔP/ΔD to be considered stable and a stop condition for the MPPT search, this threshold must be smaller than the change rate of the power with wind speed, because the stop condition has to be broken once the wind speed changes again. In this consideration, we will be dealing with an MPP zone or interval ΔD$_{MPP}$ and not a single point (the red zone in Figure 35). The upper limit of ΔD is chosen in a way to keep maintain stability of the algorithm without oscillating around the MPP. This can be chosen as smaller than ΔD$_{MPP}$/2 and this prevents the algorithm from skipping the MPP zone, or from exiting it as soon as it enters for the first time. From the Power curve we can notice that the curvature becomes narrow as the wind speed increases and thus we can choose ΔD$_{max}$ as ΔD$_{MPP}$/2 that is corresponding to the maximum wind speed.

The algorithm is not able to distinguish the variations of the output power caused by the duty cycle modulation from those ones caused by the wind speed variations. In other words, this relation must be fulfilled $|\Delta \boldsymbol{P_d}| > |\Delta \boldsymbol{P_s}|$ [33]. Therefore, in order to choose the lower ΔD limit we can use the inequality where ΔP made by changing the duty cycle should be bigger than ΔP made by wind change.

For every period of the PWM:

$$|P(D + \Delta D) - P(D)| > |P(U + \Delta U) - P(U)| \tag{37}$$

Where U is the wind speed.

ΔD is fairly small so we can consider the zone we are working with as linear and

$$P(D) = aD + b \tag{38}$$

Then

$$|P(D + \Delta D) - P(D)| = |a\Delta D| \tag{39}$$

Where:

$$\Delta D = M \frac{\Delta P}{\Delta D} \tag{40}$$

$$a = \frac{\Delta P}{\Delta D} \tag{41}$$

In conclusion, we can choose M to satisfy this condition

$$M \left|\frac{\Delta P}{\Delta D}\right|^2_{min} > |P(U + \Delta U_{max}) - P(U)|_{max} \tag{42}$$

We can find ΔU$_{max}$ by studying the change rate of wind speed, and $\left|\frac{\Delta P}{\Delta D}\right|^2_{min}$ by taking the P/R curve for lowest wind speed then finding the minimum outside the ΔD$_{MPP}$ interval.

3.6.   Proposed algorithm

Due to the lack of accuracy and relatively high 200 noise in the voltage measurement, the modified P&O algorithm seems to be highly inconsistent and mislead by the slightest of perturbations in this application. The experiment showed in Figure 36 show the poor response of the algorithm with changing input conditions, what required another modification to make the algorithm more robust and fit the application with high voltage reading noises.

The P&O algorithm that is shown in Figure 37 is proposed, and it is modified for the ability to implement a functioning algorithm taking into account the high noise in the voltage rading. Dn and Dn-1 being the new and old duty cycle, Pn and Pn-1 the respective measured power and $dP = Pn - Pn-1$. The new algorithm goes back to a fixed step duty cycle due to the huge gradient steps that were caused by the noisy readings and resulted in overshooting and reverse tracking. The oscillation problem around the MPP is minimized by and taking case where dP is less than a specified threshold as a stop condition, this way the losses are minimized with the addition of a new rule in the algorithm. The convergence speed of the algorithm is decided by the duty cycle step, as well as variables in the microcontroller configuration such as oscillator frequency, number of calculations made in the algorithm, and the data acquisition frequency.
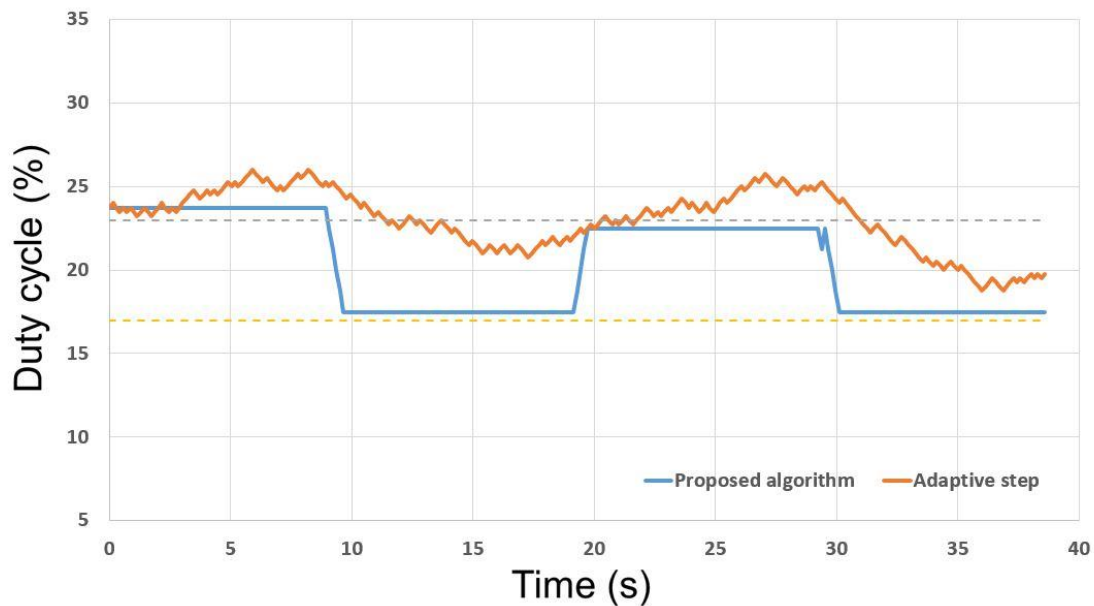
Figure 36. Experiment with the DC/DC converter prototype using the modified P&O algorithm.
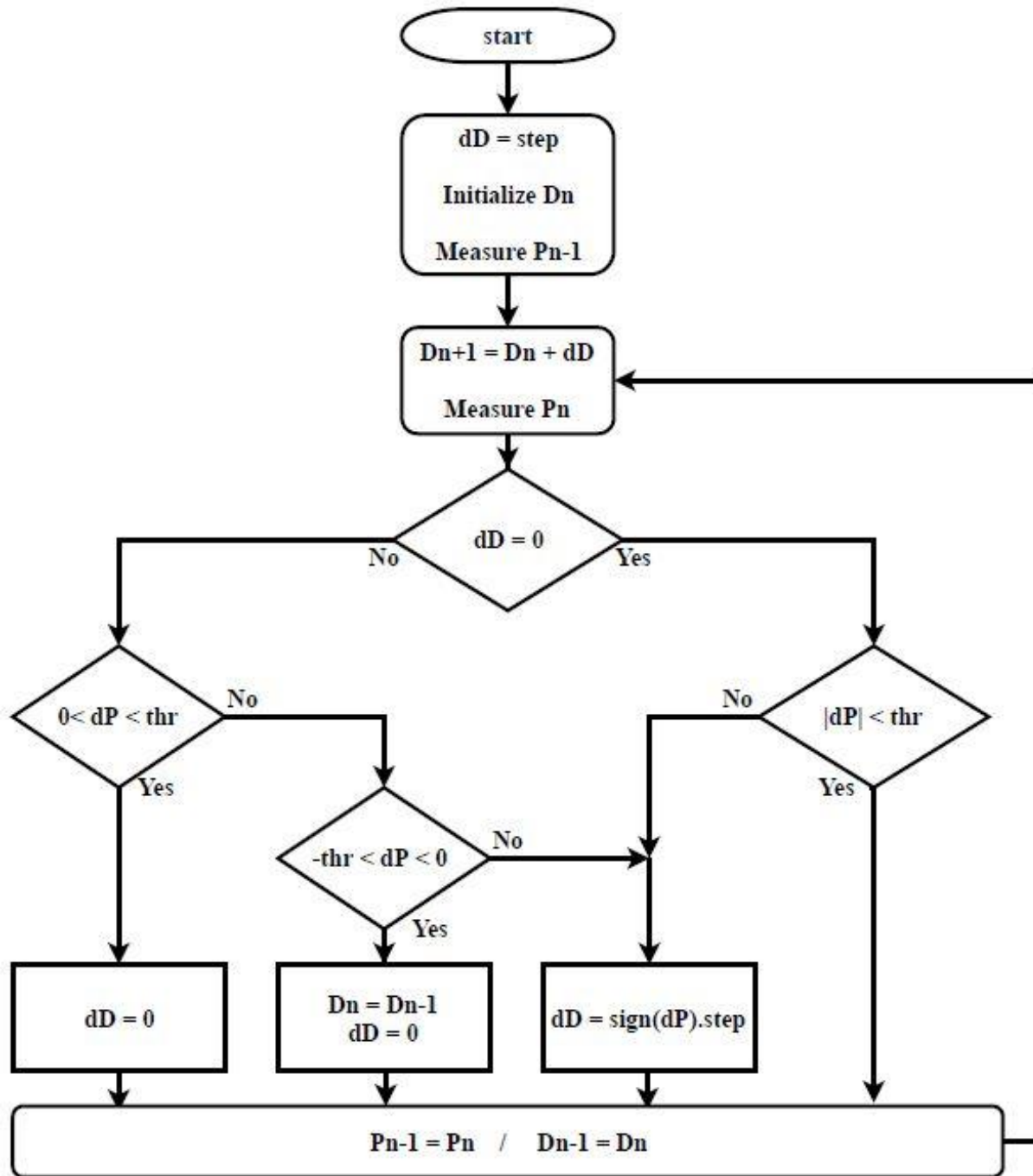
Figure 37. Flowchart of the proposed MPPT algorithm

3.6.1. Sampling error

The new algorithm prevents the ripples around the MPP, but in the cost of the accuracy of the target duty cycle, the stop condition halts the tracking when the power difference is under a specified threshold but it is not always on the MPP exactly, this means that an error on the equivalent resistance is present around the MPP that could be called sampling error This error can be calculated depending on the step size and the duty cycle by

$$\varepsilon_D(m) = \frac{\Delta R(m)}{R} = 1 - \left(\frac{D}{D+m}\right)^2 \tag{3}$$

Where m is the step size and D is the duty cycle

This relation can be visualized in Figure 38. Around a high equivalent resistance, a step of 10 which corresponds to 10/800=6.25% duty cycle- leads to 32% maximum error.
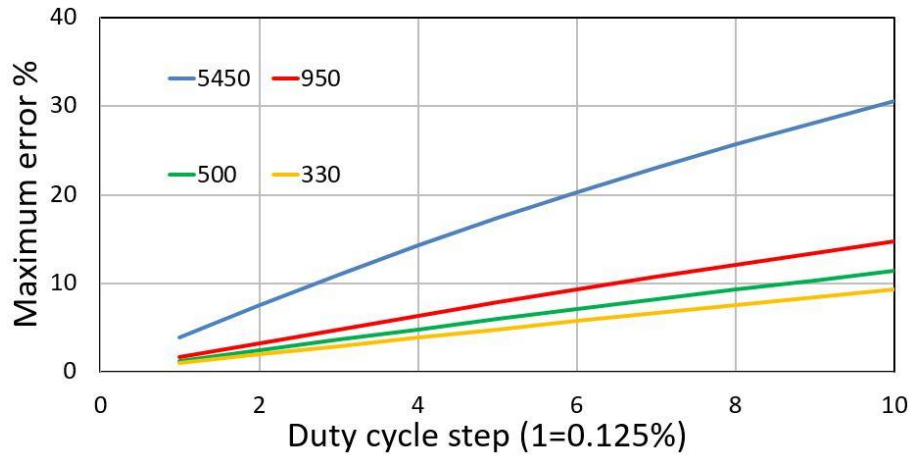
Figure 38. The relative maximum error (sampling error) with respect to the fixed step size of the duty cycle. The different plots represent different equivalent resistance values.

As previously discussed, the power curve shows that the resistance margin associated with a fixed error ΔP around the maximum, becomes wider as the wind speed decreases - thus the optimal resistance is higher-. Therefore, high error on the equivalent resistance can be tolerated, and the step size can be fixed in a way to achieve a bounded error on the input power Pin.

3.7.   Experiment

The proposed P&O algorithm was implemented on a low power MCU and tested with the harvester's interface prototypes developed in the lab. In Figure 39(a) the input voltage that is used is a generated DC signal using a power supply and it shows the response of the algorithm with a low stop threshold, the blue plot is the duty cycle perturbation, and the red plot is the target MPP, the orange plot shows the input power. The target MPP is manually changed to test how the
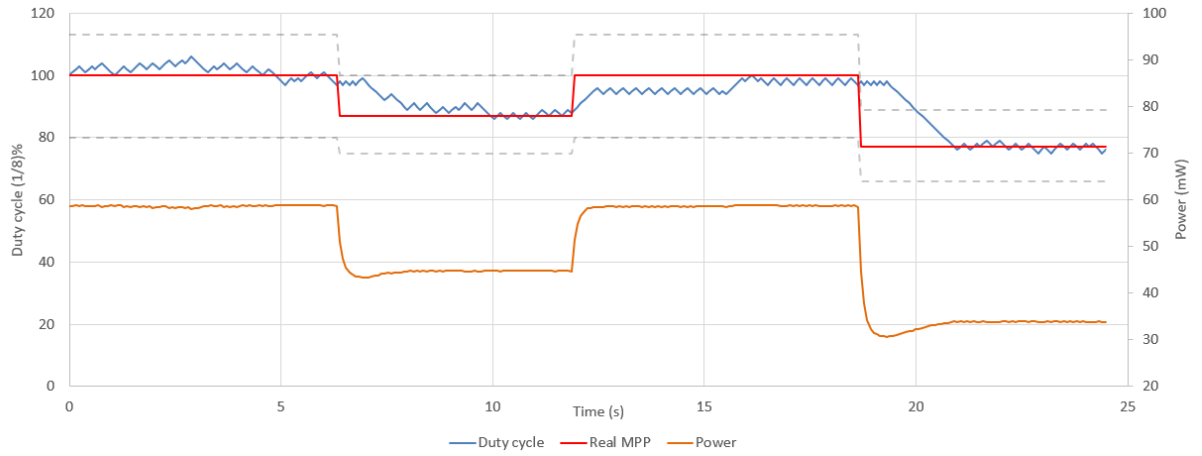
(a)
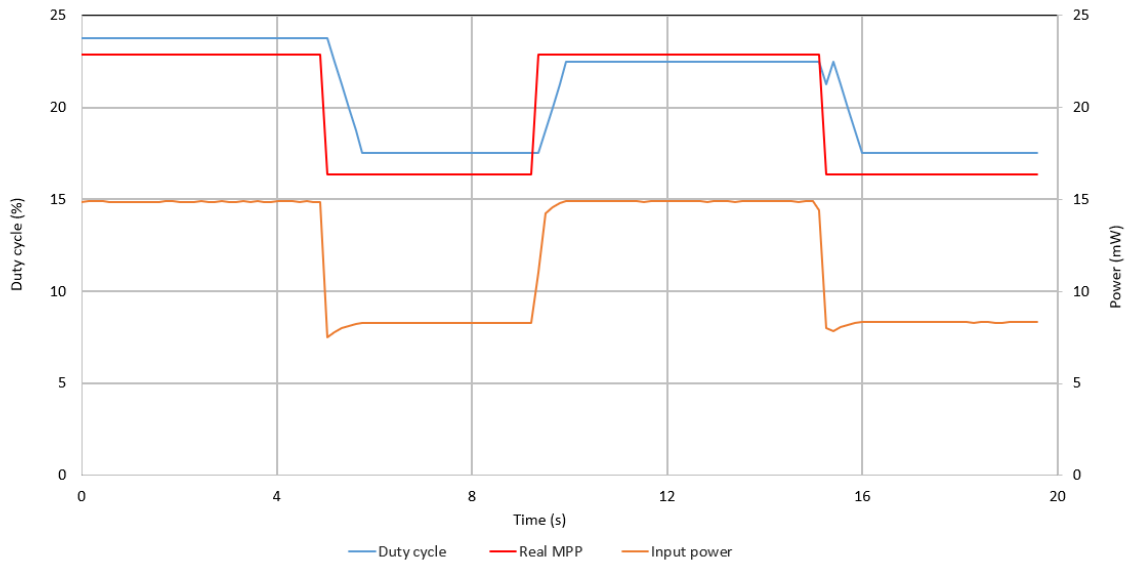
(b)

Figure 39. Experiment with the DC/DC converter prototype using the proposed algorithm. (a) with a low threshold, (b) with a high threshold.

algorithm adapts and tracks the maximum power point. I this example the oscillation exists around the MPP and this is caused when the power threshold to trigger the algorithm stop is not met, however, the resulting power fluctuations is negligeable. In Figure 39(b) the input voltage is a generated AC sinusoidal signal from a signal generator with a frequency of 15Hz. The threshold is set to a higher value, and it is clearly visible that the algorithm is meeting the stop conditions this time with the sampling error that is discussed previously in 3.6.1.

This algorithm is advantageous compared to the modified P&O since it contains less multiplication operations, and thus the microcontroller consumes less power. Comparing with the classic P&O, this algorithm contains more addition operations (1.5 in average), but in return the ripples around the MPP that cause a fluctuation in the equivalent resistance seen by the energy harvester are removed.

3.8.   Conclusion

In order to optimize the power transfer in the first stage of the energy harvesting system, an MPPT algorithm needs to be implemented with the goal of tracking the power produced by the harvester, and them controlling it through the control variables to reach a maximum transfer point. In this chapter these MPPT algorithms and their different variables were defined, and the most used algorithms were explained, namely Perturb and observe P&O, Incremental conductance INC, Lookup tables, Fuzzy Logic FL and Neural Networks NN. Additional notes on the implementation methods that are commonly used were discussed.

A simulation of the P&O algorithm was done in the laboratory and led to development of other algorithms derived from the original P&O to fit our application and compensate for some weak points that were eventually discovered. The new algorithm was discussed in detail and implemented on a low power MCU to test its validity. The experiments confirmed the goals that were required from the new algorithm, summarized into two points: speed and stability.

Chapter 4.   Power Monitoring

4.1.   Introduction

The power monitoring is important to run the MPPT algorithm that tracks the input power and optimizes the power transfer. The voltage to be tracked is alternative with changing frequency, what makes it impractical to randomly measure the voltage whenever the software calls it. Different harmonies exist in the input voltage, and that requires a knowledge of the origin of these harmonies and their frequencies. When a DC input voltage is applied to the interface circuit, the input capacitor voltage that is monitored contains some small high frequency ripples, and whenever the ADC in the microcontroller is prompted to read the voltage, it makes an inconsistent reading that cannot be relied on. Same goes for the AC signal, added to it the low frequency oscillation.

This chapter presents different techniques to solve these issues and ensure a reliable reading of the voltage, resulting in a power tracking that fulfills the MPPT algorithm requirements with small computational efforts.

4.2.   Voltage reading synchronization

In this study, the input voltage is the voltage produced by the novel wind harvester named "FLEHAP". The voltage signal is induced in the coils as a result of the oscillation movement of the wing. And due to the permanent magnets configurations and the nature of the oscillations, the signal contains different harmonies lying between 10 and 30 Hz. When the switching converter is connected to the harvester as a load, the input capacitor starts charging and discharging in synchronization with the switching frequency (Figure 40). This results in a capacitor voltage that contains low frequency and high frequency harmonies.
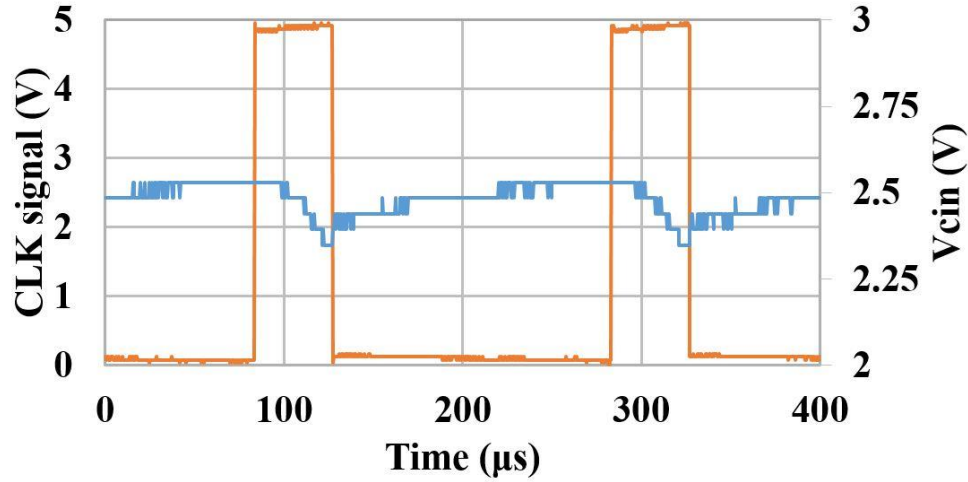
Figure 40. Plot showing the synchronized voltage with the PWM signal.

As the input voltage need to be monitored in order to run the optimization algorithm, the voltage reading can be very noisy if not managed properly due to the existence of these frequencies. To compensate for the high frequencies and obtain a consistent voltage reading, each ADC acquisition needs to be synchronized with the voltage ripples. This synchronization can be done by using the PWM signal that is driving the switching converter as an interrupt signal for the MCU, and acquiring the voltage inside the interrupt routine. The falling edge of the PWM was chosen as a trigger, this will allow the Analog-Digital Convertor to start the acquisition only with the beginning of charging cycles of the input capacitor.

To compensate for the low frequencies, other techniques must be used due to the lack of a reference. The goal is to assess the state of the input power at each iteration of the optimization algorithm, and thus there is a room to calculate the power once in every iteration. This limitation encourages the calculation of the average power in each period since the duration of iterations is close to the oscillations period, and therefore, the algorithm would be in synchronization with the low oscillation frequency of the voltage signal.

4.3.   Mean power monitoring

The lowest frequency is the fundamental and it describes the mechanical period of oscillations. The monitored power is the average power during each of the mechanical periods, but due to the lack of this knowledge, a simple algorithm is required to track the period and calculate the power. Given that the mechanical oscillation frequency is bounded depending on the accepted range of wind speeds, the proposed algorithm can track the oscillation period in the voltage signal before rectification as follows:

1. Search for the maximum peak during a time window of Tmax (yellow zone Figure 41).
2. Wait until the first occurrence of the peak with an accepted error (red zone).
3. Start adding the square for each voltage sample measured after the rectifier until Tmin time has passed.
4. Keep adding the voltage square but check for the first occurrence of the peak with an accepted error or for the end of Tmax as a stop condition (purple zone).
5. Calculate the average power (dividing the sum by the resistance R and the number of samples summed), update the peak, reset the variables, and jump to step three.
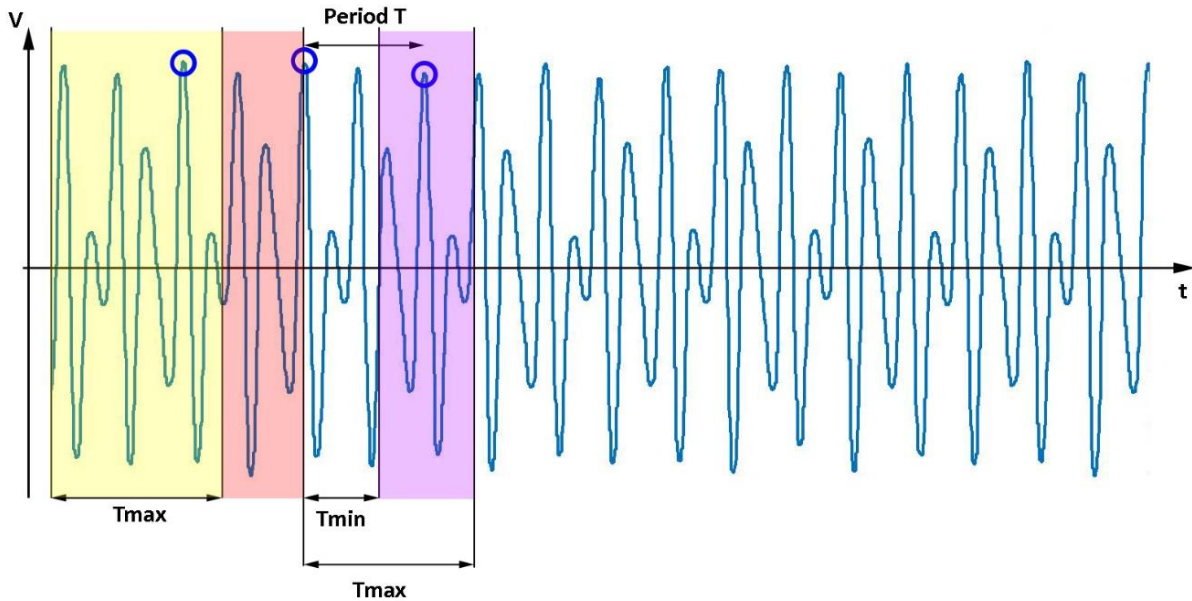
Figure 41. The method to track the voltage signal period and calculate the average power.
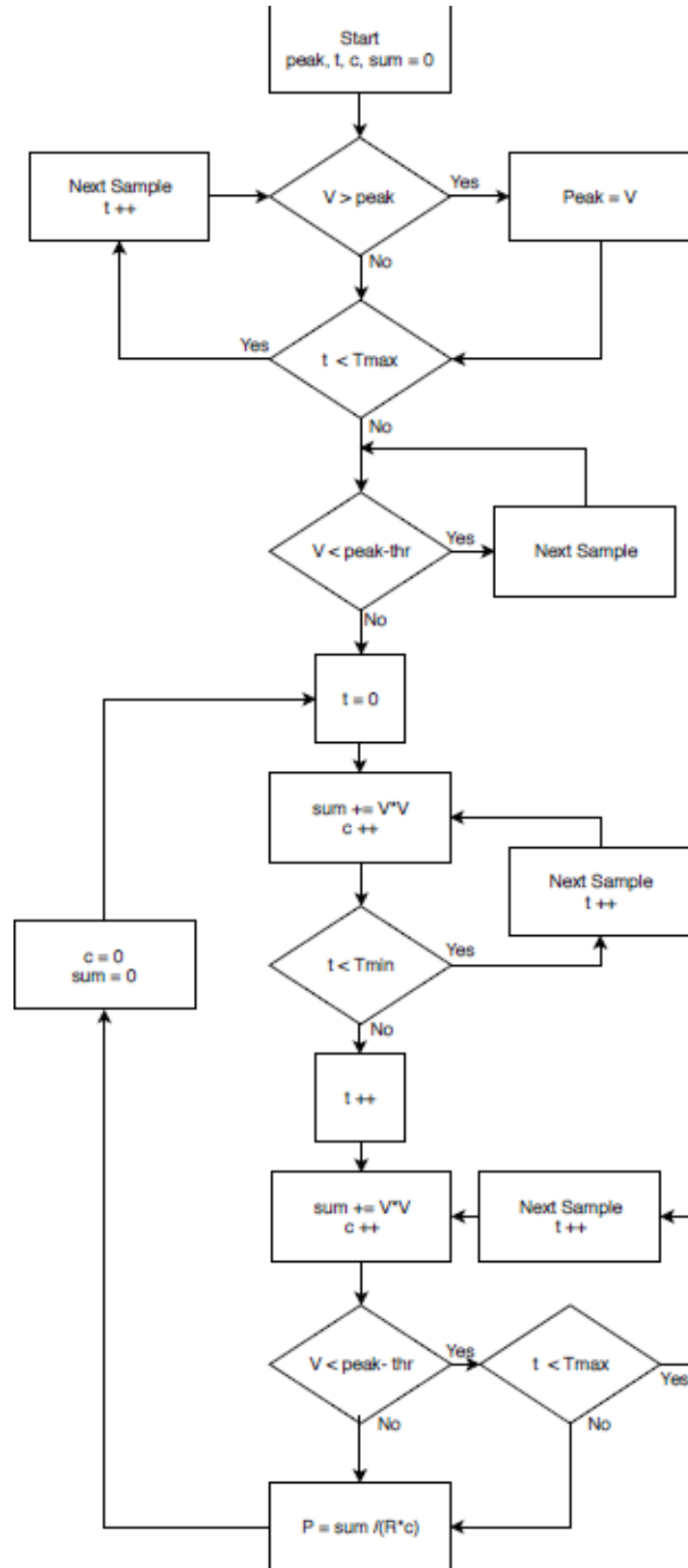
Figure 42. Flowchart of the period tracking, and average power calculation algorithm.

Figure 42 shows the algorithm where V in the voltage read from the ADC, peak is the recorded peak voltage, t is a counter for the time (samples) and c is a counter for the averaged voltage samples. The algorithm was tested in MATLAB and it has proven successful in tracking the frequency changes and calculating the average power as shown by the plot in Figure 43. Disadvantages of the algorithm include the ripples caused by the chosen thresholds and the slight variation in the peak input voltage, in addition to the computational effort that the MCU will need to run it. This depends on the microcontroller and the oscillator chosen to run it, although in this application the power consumption be not acceptable, but in different applications where a higher power is available and a fast microcontroller is used, this method can definitely serve the purpose.
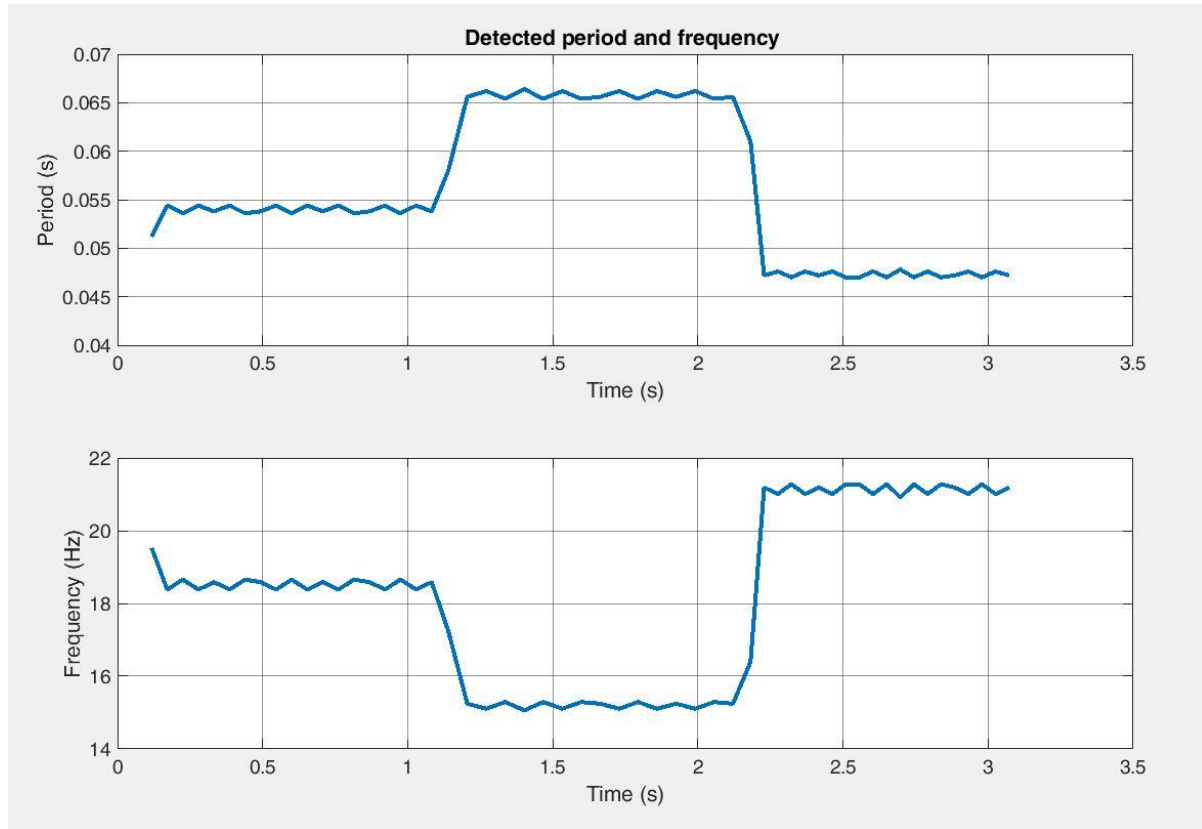
Figure 43. Simulation results of the algorithm, showing the tracking of the period and its corresponding frequency.

4.3.1 Average noise correction

A classical and simple method to correct the noise on the power reading is by taking the average of multiple consecutive samples. This helps eliminate the ripples in the power measurement but with a downside that it also eliminates any wanted small variations that are real change in power rather that noisy ripples. Since the power value is recorded in binary form in the microcontroller it would be more efficient to average the read signal in power of 2, what makes it sufficient to left-shift the sum instead of performing a division operation. The plot in Figure 44 shows the result of using this method on the mean power that is measured along the low frequency period. An average of 4 measurement samples is chosen and it shows a good level of ripple elimination, but a higher sample count needs to be used in order to eliminate the unwanted ripples.
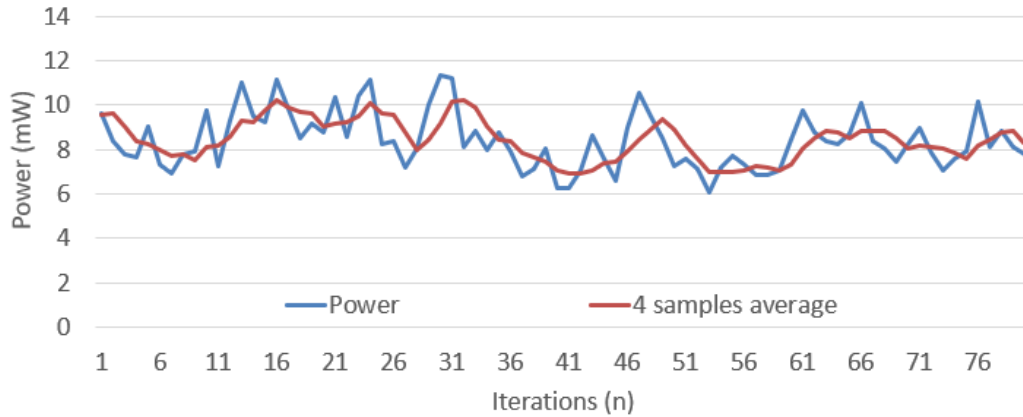
Figure 44. Noise elimination using the average window of 4 samples.

4.3.2 Kalman filter noise correction

Kalman filter is designed to predict the correct values for noisy measurements, using a probabilistic model. In this work, it is used to correct the ripples caused by the power monitoring algorithm, the method was presented in the paper [47]. Figure 45 shows the contribution where the Kalman filter is used on the input side of the MPPT block, in contrast to the literature where the filter is used to correct the output of the MPPT.

An important point to consider when implementing Kalman filter is that the chosen system model has a huge impact on the outcome of this algorithm, which makes it very important for the model to be as representative of the system as possible.
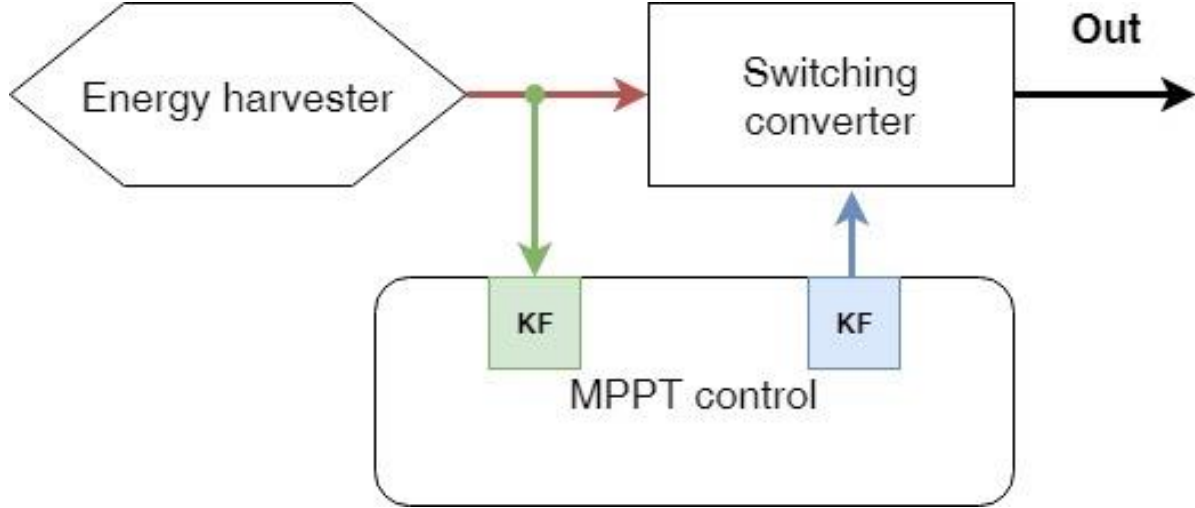
Figure 45. Block diagram showing the application of MPPT with Kalman filter, in green is the proposed implementation and in blue is the implementation in other literatures.

To tackle the power reading problems, all the parameter acting on changing the power value must be sorted, and can be classified into 2:

1. The wind speed change that affects the harvested power level as well as the harvesting device characteristics.
2. The well-defined duty cycle variation that is controlled by the MPPT algorithm.

The wind speed change has a random nature and thus its effect can be modeled as a probabilistic variable following a normal distribution with a previously defined mean and variance based on statistics. To model the power variation resulted from the MPPT algorithm, the duty cycle expression of the duty cycle step could be used. Considering the step small enough to give a linear variation, the next power value can be modeled as follows:

$$dP = \frac{\partial P}{\partial D} . dD \qquad (43)$$

For the variable step P&O, the duty cycle is incremented by a step of $M\frac{dP}{dD}$ on every iteration, and thus:

$$dD = M\frac{dP}{dD} \qquad (44)$$

$$dP = M \left(\frac{dP}{dD} \right)^2 \tag{45}$$

The signals in practice are discrete and in MPPT the slope is considered equal to the slope calculated from previous samples, what allows the power change to be expressed as follows:

$$P[k+1] - P[k] = M \left(\frac{P[k] - P[k-1]}{D[k] - D[k-1]} \right)^2 \tag{46}$$

Where P is a power measurement, M is a constant controlling the speed of the MPPT and D is the duty cycle value.

Kalman filter uses a state-space linear representation as follows:

$$x[k+1] = Ax[k] + Bu[k] + w[k] \tag{47}$$

$$z[k] = Cx[k] + v[k] \tag{48}$$

Where x[k] is the state, z[k] and u[k] are the output and input, w[k] and v[k] are the process and measurement noises that could be considered white Gaussian, represented with the wind speed and measurement variances.

Applying the previous model, the following state-space representation is obtained:

$$P[k+1] = P[k] + M \left(\frac{P[k] - P[k-1]}{D[k] - D[k-1]} \right)^2 + w[k] \tag{49}$$

$$z[k] = P[k] + v[k] \tag{50}$$

To validate the suggested model and have a rough estimation about the performance, MATLAB simulations were performed on a real case scenario, where an MPPT power measurement is done on a rectified AC signal with variable frequency, using an algorithm that detects the period and integrates over that period to output the mean power of the signal. This algorithm has a measurement error mainly caused from the noisy voltage measurement and thus it inherently outputs noisy results. In these simulations, the constants in the Kalman filter algorithm are chosen approximately in a way that matches the real world. These constants are summarized in M: the MPPT step rate that can be 1 in most cases, R the variance of input noise: that can be obtained by finding the corresponding values in average windspeed variations in the working area, and Q the variance of the measurement noise: it can be found in the noisy power measurement graph. Figure 46(a) shows a simple simulation that is ran without applying the MPPT, where the blue plot is the power measured with the integration algorithm and the green plot shows the corrected power using

Kalman filter. Applying the MPPT algorithm with variable step (Figure 46(b)), it can be seen how the filtered signal is more robust and follows the change in power with a 97% drop in the variance, and thus obtaining a more accurate measurements to ensure the stability and convergence of the algorithm.

(a)

(b)
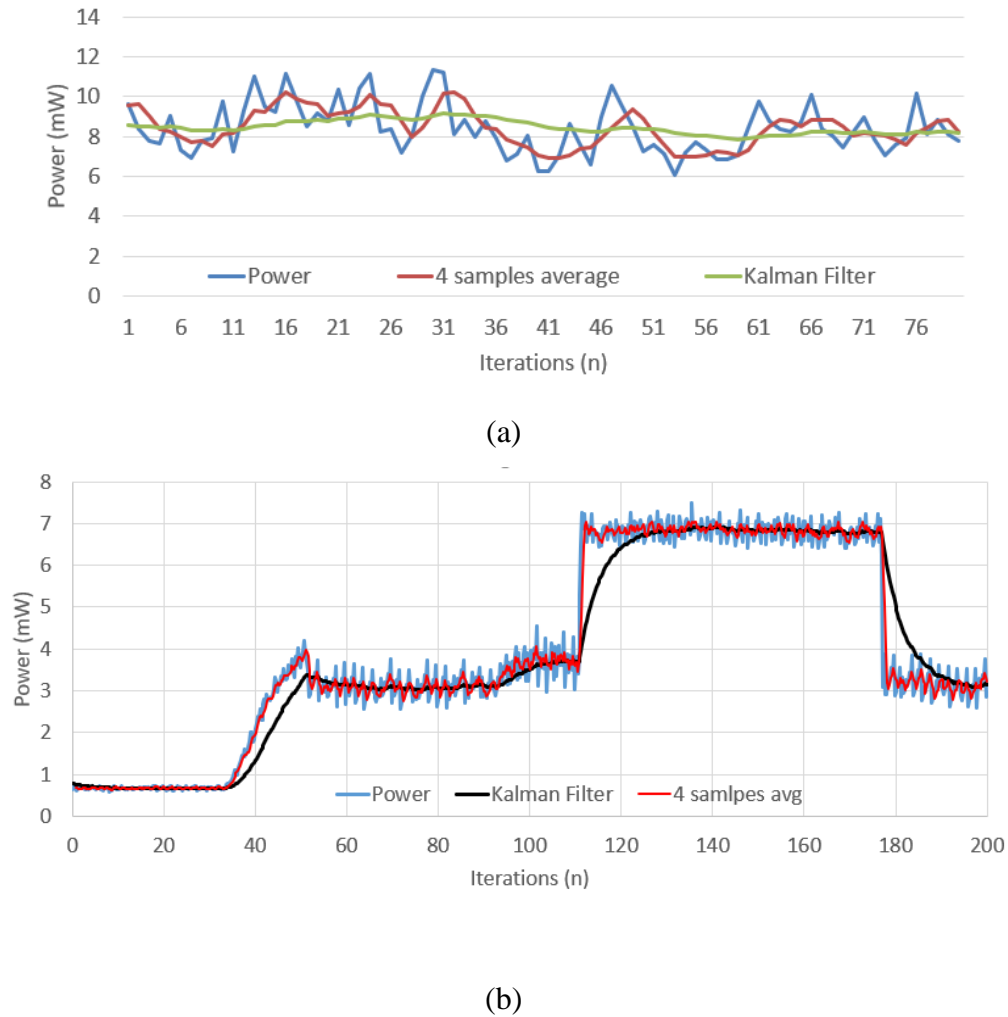
Figure 46. Plot showing the simulation results of both average and Kalman filter methods on (a) a simple power measurement, (b) power following the MPPT algorithm.

4.4. Peak power monitoring

An important remark in the power monitoring issue is that the power is being measured to feed the MPPT algorithm with the values to make the calculations. The algorithm in fact tracks the

variation of power and thus the instant value is not as important as the differential value. For this reason, it is sufficient to measure the peak AC voltage and rely on it to monitor the variation of power since the differential value of the peak power is representative of the differential value of the average power. This approach will lower the computations needed and limit the iterations duration. The peak monitoring can be done either on the hardware or the software level.

4.4.1 Software solution

To find the peak power it is sufficient to take a time window that is guaranteed to contain a voltage peak inside, and then search for the maximum voltage value in that window. That time window is the maximum possible period T_{max} that corresponds to the minimum possible frequency for the mechanical system (Figure 47), since the system's oscillation frequency is bounded due to physical constraints. This method again will limit the iteration's duration to be no equal to T_{max} at
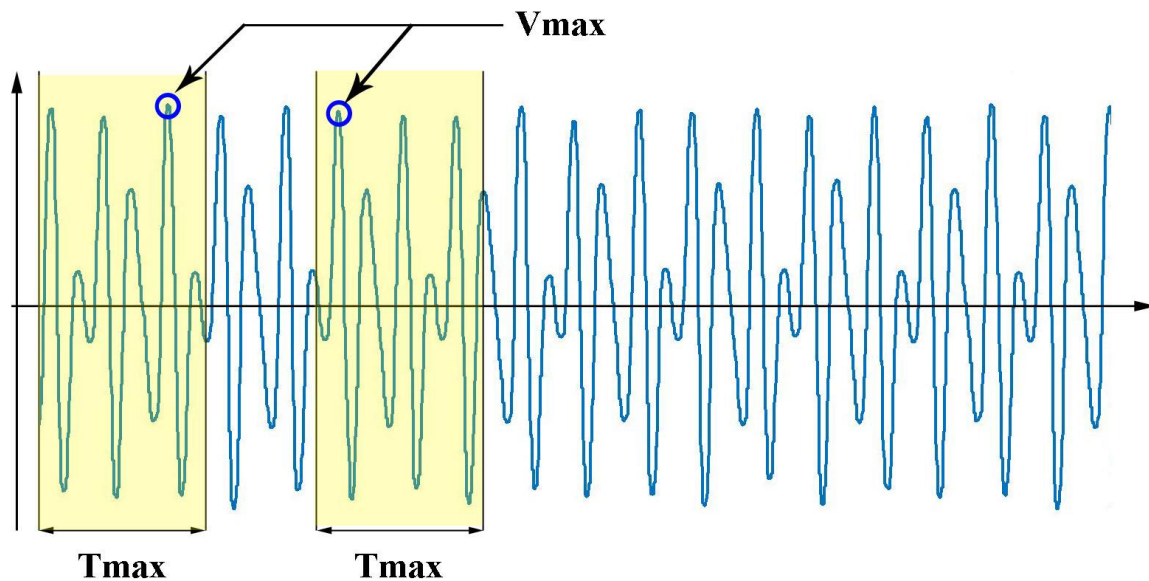
Figure 47. Visual explanation of the peak detection algorithm. The yellow zones present the zones where the algorithms searches for a peak.

minimum. Being the least demanding method in computational effort, this method was in many prototypes that were developed in the COSMIC lab, with the aim to use the hardware peak detection in the later prototypes.

4.4.2 Hardware solution

The hardware peak detector is a solution that can be used due to the passive nature of this small circuit. It consists of a diode that can be any type followed by a shunt capacitor. Figure 48 shows the configuration with an example of the input and output voltage. The components are not ideal, what will produce a voltage drop and a small delay in the output signal. However, this is not a problem since the point of interest is not the voltage value itself but the differential value between 2 consecutive readings instead. This fact negates the loss caused by the voltage drop across the diode. This peak detector was implemented in the final prototype of the system using a Schottky diode and a 1µF capacitor.
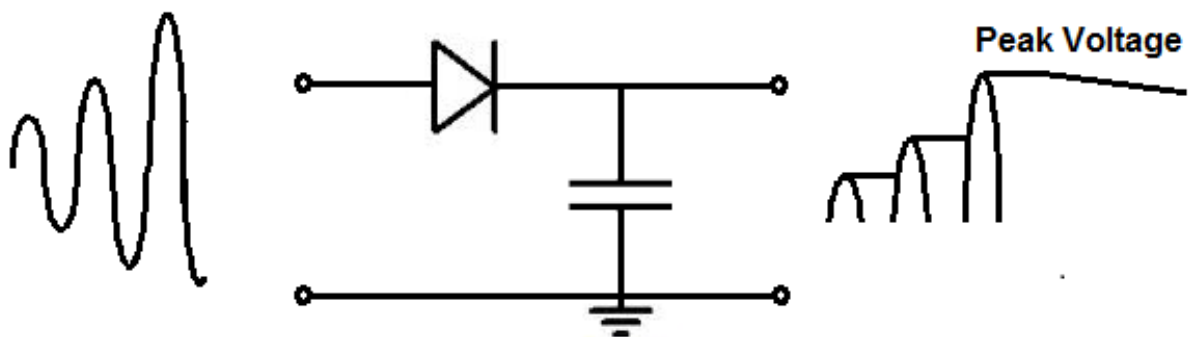
Figure 48. Peak detection circuit.

4.5.   Conclusion

In this chapter, the problem of voltage and power monitoring in the electronic interface for the energy harvester was addressed. The input voltage signal is alternative with changing frequency what requires attention in measuring and monitoring it. Different solutions were presented, first for the high frequency ripples, a synchronization with the PWM signal would make consistent readings, and for the low frequency oscillations, techniques such as mean power tracking and peak points tracking were discussed. An algorithm was used to tract the period and thus calculate the average power on each period, but some inconsistencies were present in the reading what further

requires correction. Correction methods were investigated namely average correction and Kalman filter, where the implementation relies on the knowledge of the dynamics of the system. These algorithms were simulated in MATLAB and then used in experiments in the prototypes developed in the COSMIC lab.

Chapter 5.   FLEHAP Energy Harvester

5.1. Introduction

The Fluttering Energy Harvester for Autonomous Powering FLEHAP is a novel wind energy harvester that uses the fluttering mechanism to transform the wind energy into an electrical signal. Many energy harvesting devices have been studied and deployed, and each has its own characteristics that need to be studied and understood, to correctly deal with device. The behavior of the harvester in addition of the chaotic randomness of the environment introduce many challenges when someone wants to make the best use of a certain energy harvesting technique. The state of the art shows different energy harvesters and the techniques that are usually used to deal with their problems and optimize the outcome.

This chapter presents the methods we have used to study the novel wind harvester, the methodology that is adopted to tackle the problems and the work that has been done in the lab in order to experiment and validate our approaches.

5.2. Physical device

The technologically well-developed windmills and micro turbines suffer very low efficiencies at small speeds due to laminar separation effects that subsist at low Reynolds number. An alternative method to harvest energy from a wind is based on the fluttering instability effect, in which moving bodies are typically connected to elastic materials.

The device in study, named FLEHAP (Fluttering Energy Harvester for Autonomous Powering), conceived and developed in DIFI of University of Genova, is characterized by a fully passive 'pitch and plunge' fluttering of an airfoil with any torsional spring. The mechanical system is simply composed by a semi-rigid wing (acetate airfoil of thickness of 0.2 [mm] and density of 1.4 [g/cm3]), free to rotate around an axis, intimately connected to one or more elastic elements (e.g. see Figure 49). When a fluid interacts with the structure, if the parameters are correctly set, a self-

sustained oscillation characterized by a vertical harmonic motion of the axis, and consequently, by a periodical lemniscate motion of the trailing edge of the wing, is achieved by the system in a wide range of flow speed.

The main electrical extraction strategy proposed in this work exploits an electromagnetic coupling (EMc) obtained by placing a pair of coils at the ends of the pivot axis of the wing and two series of permanent magnets in alternated polarity configuration in front of their predicted trajectories [21].
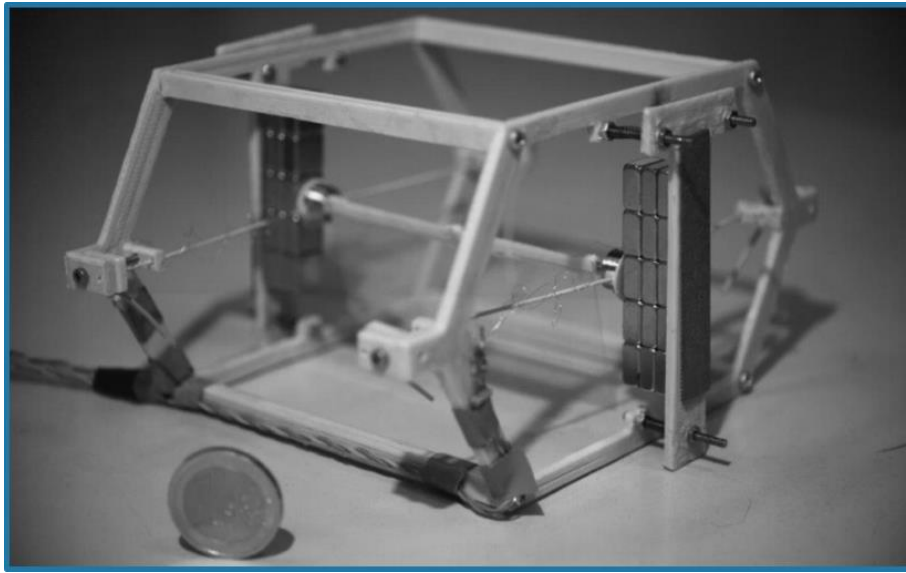
Figure 49. The FLEHAP wind energy harvesting device.

5.3.   Heuristic model

In order to better understand the behavior of the system, developing a mathematical model can be a very useful step. In addition, it helps with conducting any type of simulation to study the possible interactions between the harvester and the physical environment, alongside with the output resulting on these interactions. Taking decisions based on the simulation results is a time saving strategy that is usually adopted instead of trial and error, what can be costly and lead sometimes to waste of time, resources and effort.

For this purpose, an attempt to develop a heuristic model based on different experiments and observations from the FLEHAP harvester was done, resulting on two different models explaining

respectively the shape of the output voltage with its harmonics, and the output power variation for different loads.

5.3.1 Output voltage model

The output voltage of the harvester contains different harmonics as shown in the Figure 50, these data are collected physically through experiment. In order to use this voltage signal in simulations or any computational problem, a mathematical model is needed. It also helps predicting the form and characteristics of the voltage signal whenever a physical parameter changes in the harvester
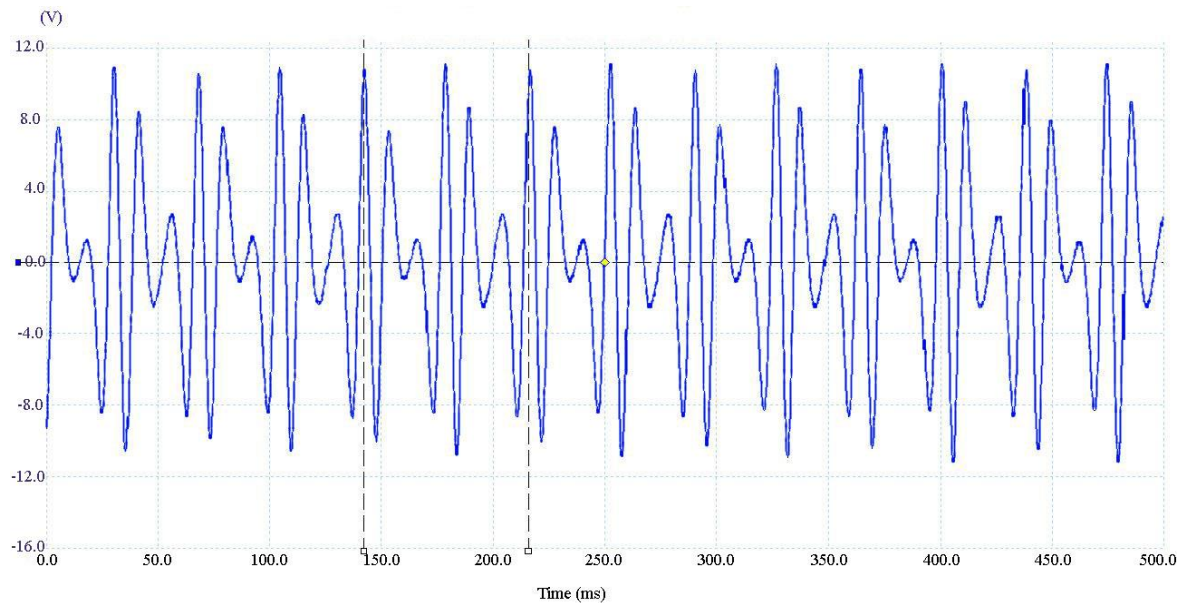
Figure 50. The output voltage extracted from the FLEHAP device.

or the energy source, or when different configuration in the harvester's coils or magnets is made for trial. In order to develop the mathematical model, it is necessary to make approximations to simplify the calculation.

Magnetic flux:

As shown in Figure 52 [24] the alternating permanent magnets are a series of magnetic dipoles and so the magnetic field can be calculated or simulated at each point of interest. One problem here is the complexity of calculation especially around the boundaries.
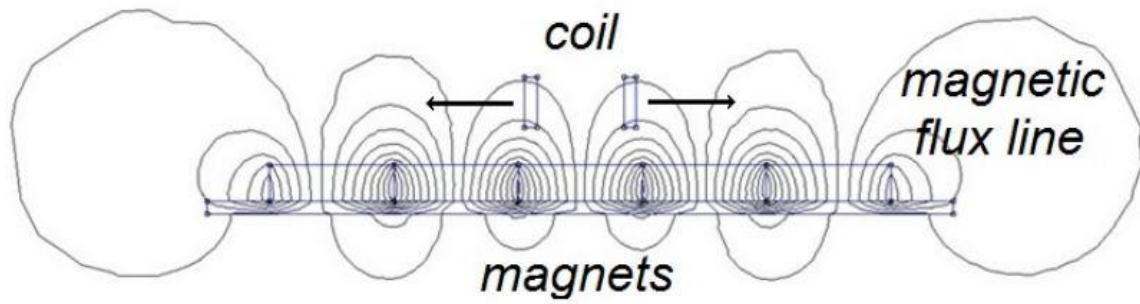
Figure 52. The magnetic field lines resulting from the alternating permanent magnets.

However, the goal is to calculate the magnetic flux density through the coil which is always on a fixed distance from the magnets and oriented normally to the dipoles direction, what nullifies the flux density as the coil approaches the boundary of each dipole. Similarly, on the boundaries of the whole coil group, the velocity of the coil will be nullifying and thus we can approximate around
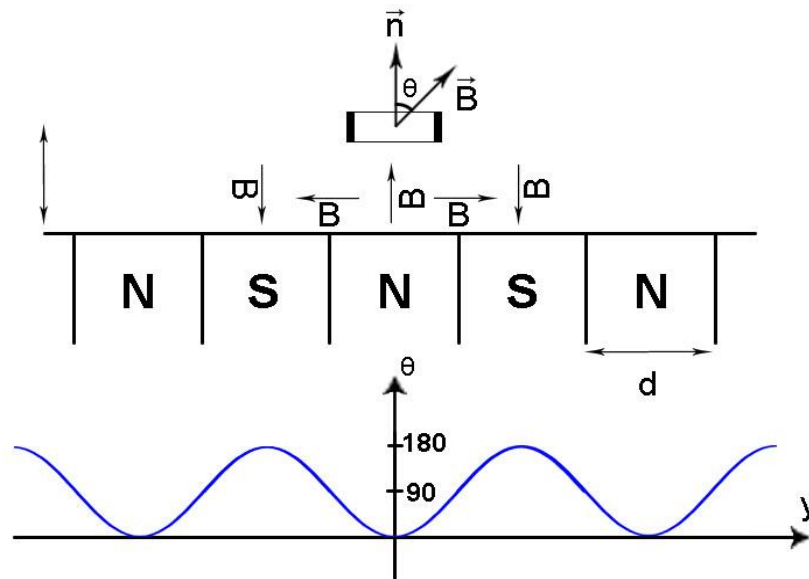
Figure 51. The angle between the normal vector of the coils and the magnetic field along the y axis.

this point by considering an infinite set of coils. An approach that we can take is to consider the magnetic field constant in value, variable in direction.

The angle between the coils surface vector and the magnetic field can be modeled as a cosine function (Figure 51) with respect to the dipoles axis (y axis) defined on $\mathbb{R}$.

$$\theta(y) = \frac{\pi}{2}\left(1 \pm \cos\left(\frac{\pi}{d}y\right)\right) \qquad (51)$$

d is the magnet's length in the y direction , and the sign depends and the N/S configuration.

A simulation that is made on FEMM shows an agreement with the above Equation (51), where Figure 53 shows the magnetic flux which is proportional to $\theta(y)$ since the magnitude of the magnetic field B is considered constant.
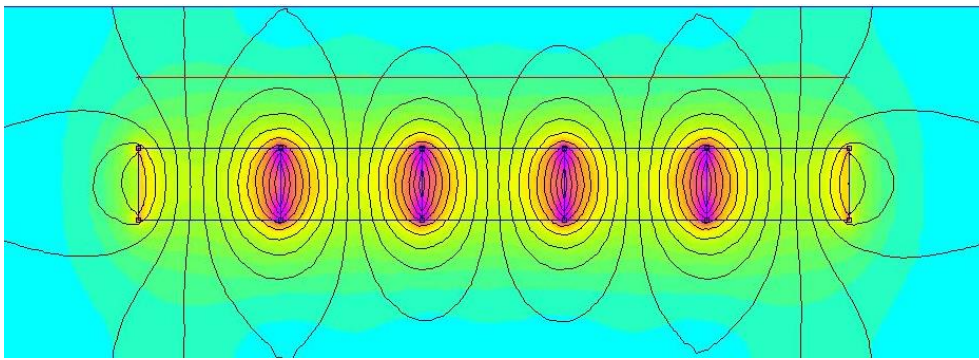
(a)
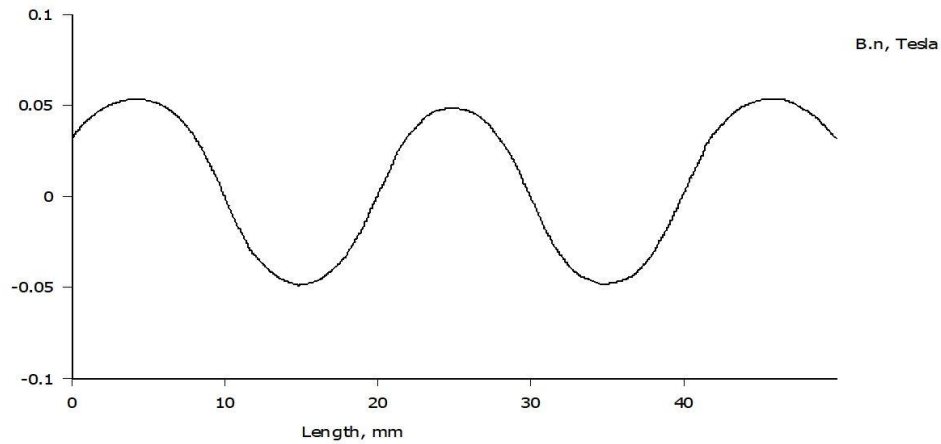
(b)

Figure 53. Simulation of the alternated magnets in FEMM showing (a) the magnetic field lines, (b) the magnetic field normal component along the y axis.

Harmonic movement:
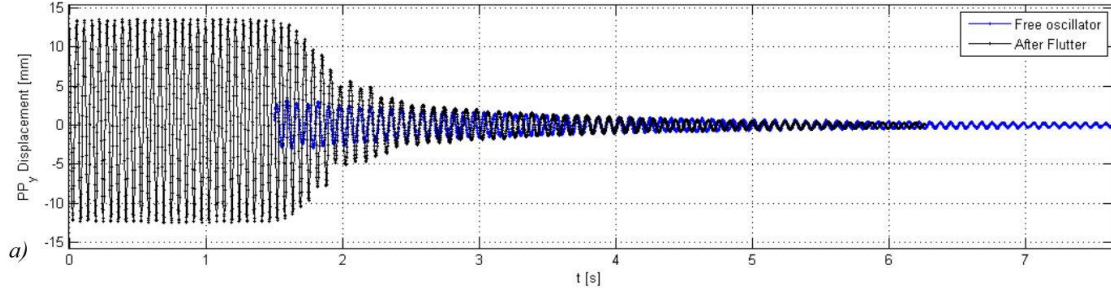
Figure 54. The dumping oscillation of the pivot point.

The coil in the simplest configuration is vertically oscillating and can be modeled as a sine function: The plot in Figure 54 is a taken from the measurements done by [24] showing the dumped oscillations of the pivot in the absence of the wind. And therefore the coils (pivot point) vertical movement can be described in the following relation:

$$y(t) = PP_{ymax} \sin(2\pi f t) \tag{52}$$

Where f is the oscillation frequency and PP_{ymax} is the highest point the pivot can reach from the central axis.

Combining equations (51) and (52) we can get the flux angle with respect to time:

$$\theta(t) = \frac{\pi}{2}\left(1 \pm \cos\left(\frac{\pi}{d}\left(PP_{ymax} \sin(2\pi f t)\right)\right)\right) \tag{53}$$

The flux density will be as follows:

$$\Phi(t) = B.S.\cos\left(\theta(t)\right) \tag{54}$$

We can then differentiate the flux density in time to calculate the induced voltage according to Faraday's Law:

$$emf = -\frac{d\Phi}{dt} \tag{55}$$

$$\frac{d\Phi(t)}{dt} = \pm\frac{B.S.PP_{ymax}.f.\pi^3}{d}cos(2\pi ft)sin\left(\frac{\pi.PP_{ymax}}{d}sin(2\pi ft)\right)sin\left(\frac{\pi}{2}\left(1\pm cos\left(\frac{\pi.PP_{ymax}}{d}sin(2\pi ft)\right)\right)\right) \tag{56}$$

The variable PPymax is directly related to wind speed, although not proportional but the relation can be developed as seen in [24] and it is highly dependent on the materials used and configuration of the harvester. Figure 55 show a plot of the emf Equation (56) with the parameters: B=S=1, f= 20Hz, d = 2mm, which are similar to the real harvester, and for Yppmax= 2,3,4,5 mm caused from different wind speeds.
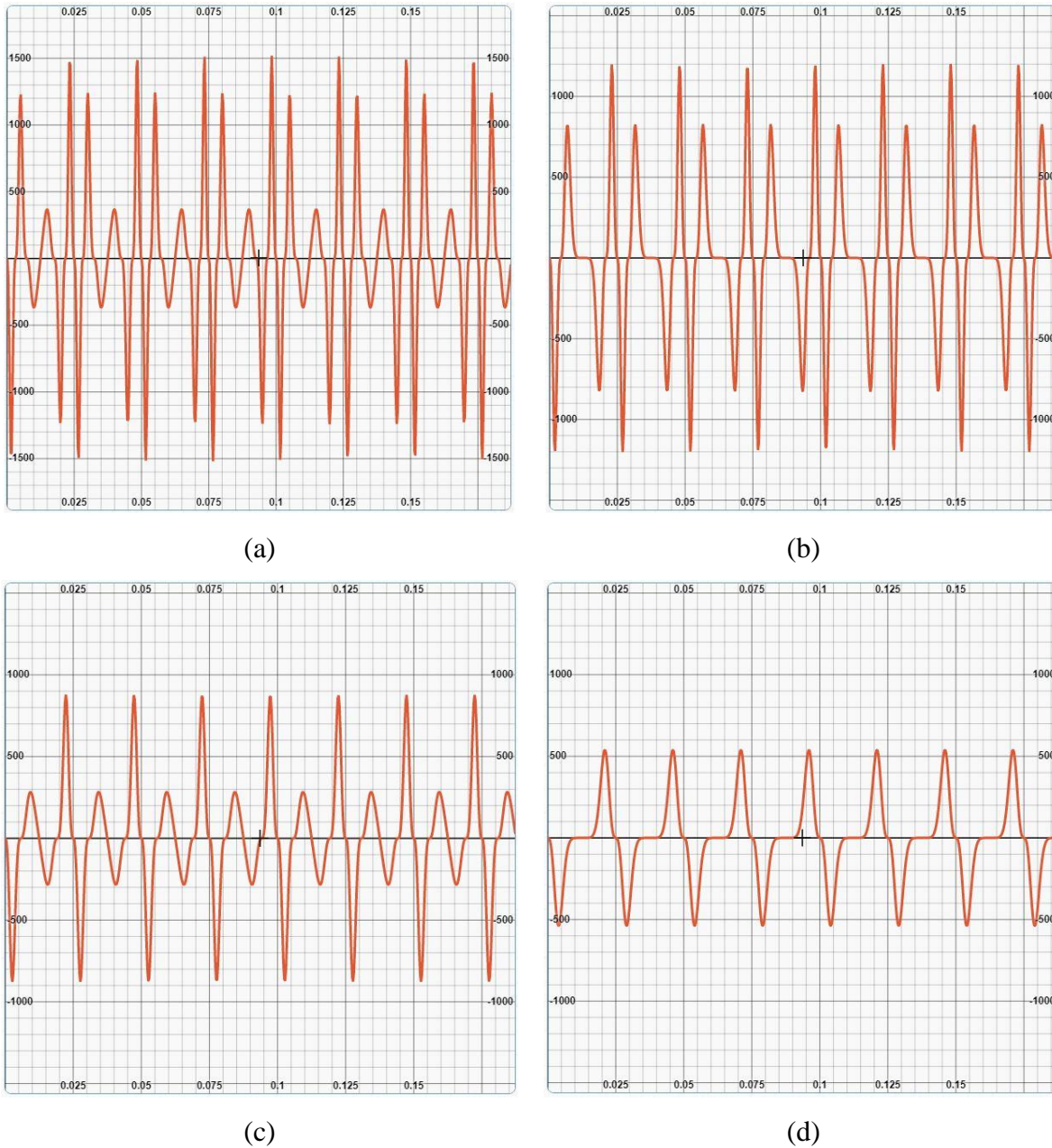
Figure 55. Plots of the voltage functions for values of PPymax respectively 5-4-3-2mm (a),(b),(c),(d) what corresponds to different wind speeds.

This relation is a model for an open circuit, and it describes the system unloaded. However, with the presence of a load and therefore a current, an induced force will be opposing the wind force acting on the wings. For future work, a closed loop model can be developed based on the feedback from the induced force. The block diagram in Figure 56 roughly describes the closed loop model, it is necessary to break the function relating wind speed and the pivot point maximum position to model the intermediate parameter which is the vertical projection of the force Fy acting on the pivot point, what allows us to subtract the forces and come up with the accurate description of the voltage signal when a load is present.
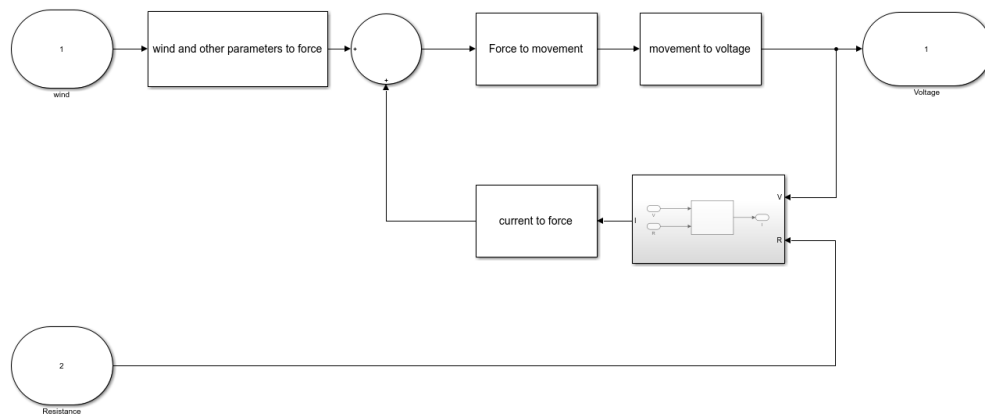
Figure 56. Block diagram showing the closed loop model for the system.

5.3.2   Electromechanical model

Another observation from [24] shows that a relation between the maximum output voltage expressed in and the maximum pivot point vertical location Yppmax can be expressed as a second degree polynomial. This can lead to a different expression of the model above (Figure 56) where the feedback point is Yppmax. Figure 57 shows the new block diagram where the feedback branch expresses the relation between the output voltage and the output load, into the pivot point displacement.
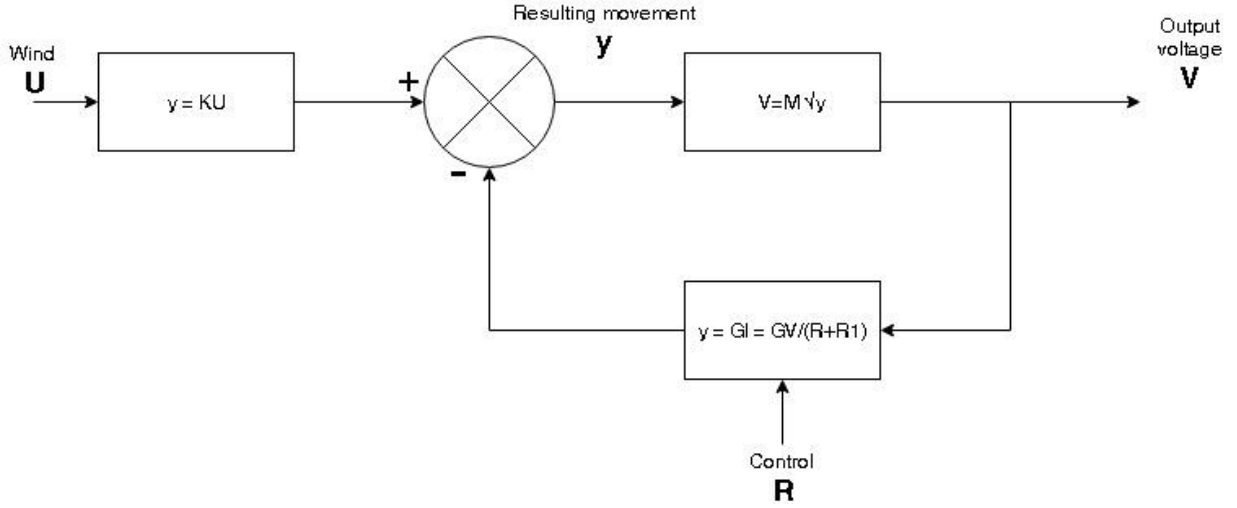
Figure 57. The block diagram for the eletromechanical model.

Assuming that we assign the following transfer functions to these blocks:

- $y = KU$ For the mechanical part transforming wind speed to movement, the y here is Yppmax of the pivot of oscillating wing, U is the wind speed and K is a constant.

- $V = M\sqrt{y}$ For the coil and magnets transforming the movement to electromotive force EMF, taking into account that the voltage is null when y is 0, V is the maximum output voltage and M is a constant.

- $y = GI = G\frac{V}{R+R_1}$ Assuming that the displacement of the pivot point as a result of an induced force is linear. R and R1 are respectively the load and the harvester's resistance, and G is a constant.

From the block diagram, we can deduce the transfer function as:

$$V(U,R) = M\sqrt{KU - \frac{G}{R + R_1}V(U,R)} \tag{57}$$

$$V(U,R) = \sqrt{M^2KU + \frac{G^2M^4}{4(R + R_1)^2} - \frac{GM^2}{2(R + R_1)}} \tag{58}$$

And then we calculate I and P the current and average power respectively

$$I = \frac{V}{R + R_1} = \frac{1}{R + R_1}\left(\sqrt{M^2 KU + \frac{G^2 M^4}{4(R + R_1)^2}} - \frac{GM^2}{2(R + R_1)}\right) \tag{59}$$

$$P_U(R) = RI^2 = \frac{R}{(R + R_1)^2}\left(\sqrt{M^2 KU + \frac{G^2 M^4}{4(R + R_1)^2}} - \frac{GM^2}{2(R + R_1)}\right)^2 \tag{60}$$

To find the maximum point of $P_U(R)$ we search for $\frac{dP_U}{dR} = 0$

$$\frac{dP}{dR} = -\frac{\left((2R + 2R_1)\sqrt{\frac{G^2 M^4}{4(R + R_1)^2} + M^2 KU} - GM^2\right)^2 \left((R^2 - R_1^2)\sqrt{\frac{G^2 M^4}{4(R + R_1)^2} + M^2 KU} - GM^2 R\right)}{4(R + R_1)^6 \sqrt{\frac{G^2 M^4}{4(R + R_1)^2} + M^2 KU}} \tag{61}$$

$$\begin{cases} \left(2(R + R_1)\sqrt{\frac{G^2 M^4}{4(R + R_1)^2} + M^2 KU} - GM^2\right) = 0 \Rightarrow M^2 KU = 0 \ incorrect \\ \\ \left((R^2 - R_1^2)\sqrt{\frac{G^2 M^4}{4(R + R_1)^2} + M^2 KU} - GM^2 R\right) = 0 \xRightarrow{R>0} \frac{1}{2}(R - R_1)\sqrt{G^2 M^4 + 4M^2 KU(R + R_1)^2} - GM^2 R = 0 \end{cases} \tag{62}$$

The plot of the Power in function of R for different wind speeds and with the approximated parameters (G=500, K=0.1, R1=300, M=1), shows a similarity with the previous experimental results made on the harvester (Figure 58). The most important highlight is that the optimal resistances have an asymptote at R=300Ω at infinite wind speed, which is equal to the internal resistance of the coils (The maximum locus was plotted using a MATLAB script).

(a)   (b)
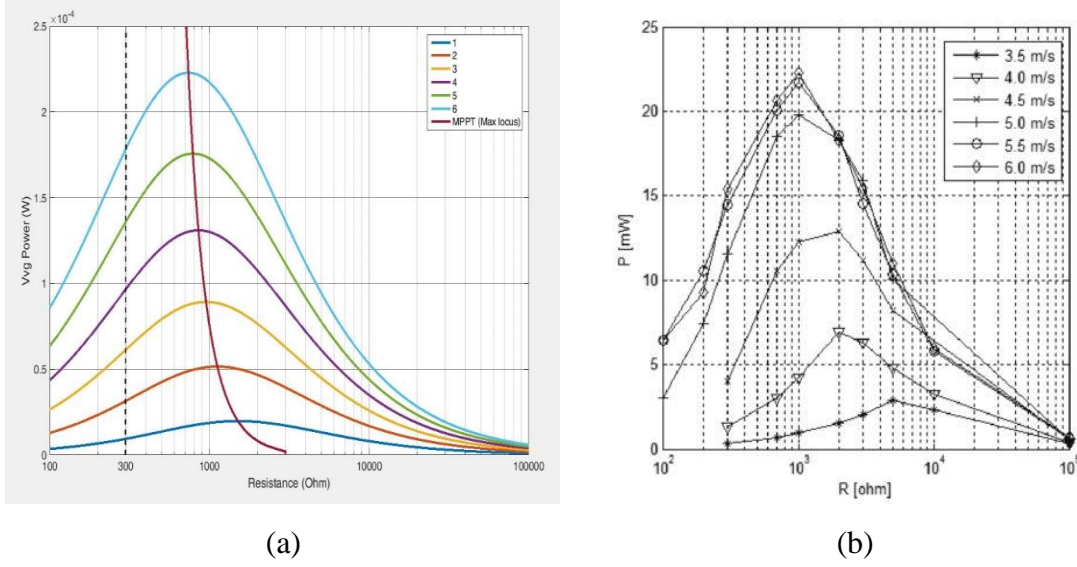
Figure 58. (a)Plot of P from eq(1) assuming the values: G=500, K=0.1, R1=300, M=1, and for different values of U(wind speed).(b) is the referenced experimental results.

From this relation we can derive the maximum power locus that describes the optimal resistance in function of the wind speed.

From the equation (62) we have to solve:

$$\frac{1}{2}(R - R_1)\sqrt{G^2 M^4 + 4M^2 KU(R + R_1)^2} - GM^2 R = 0 \tag{63}$$

The roots of this equation describe the locus of the maximum power. The equation can be solved for R by neglecting the constant $G^2 M^4$, and we can only do that when the second term is bigger by one order of magnitude, therefore when this inequality is satisfied:

$$4M^2 KU(R + R_1)^2 > 10 G^2 M^4 \tag{64}$$

We note that always $> R_1$:

$$4M^2 KU(R + R_1)^2 > 4M^2 KU(2R_1)^2 \tag{65}$$

Thus, the condition will be satisfied when:

$$4M^2 KU(2R_1)^2 > 10 G^2 M^4 \tag{66}$$

$$U > \frac{5G^2 M^2}{8KR_1^2} \tag{67}$$

When this condition is satisfied, we can find the roots as follow:

$$\frac{1}{2}(R - R_1)\sqrt{4M^2KU(R + R_1)^2} - GM^2R = 0 \tag{68}$$

$$R(U) = \sqrt{R_1{}^2 + \frac{G^2M^2}{4KU} + \frac{GM}{2\sqrt{KU}}} \tag{69}$$

The graph in Figure 59 shows a comparison between the derived equation and the locus plotted from the simulations, we note that after $U > \frac{5G^2M^2}{8KR_1^2} \approx 2$ the two plots are almost identical, therefore, this confirms that the optimal resistance has an asymptote at the value R1.
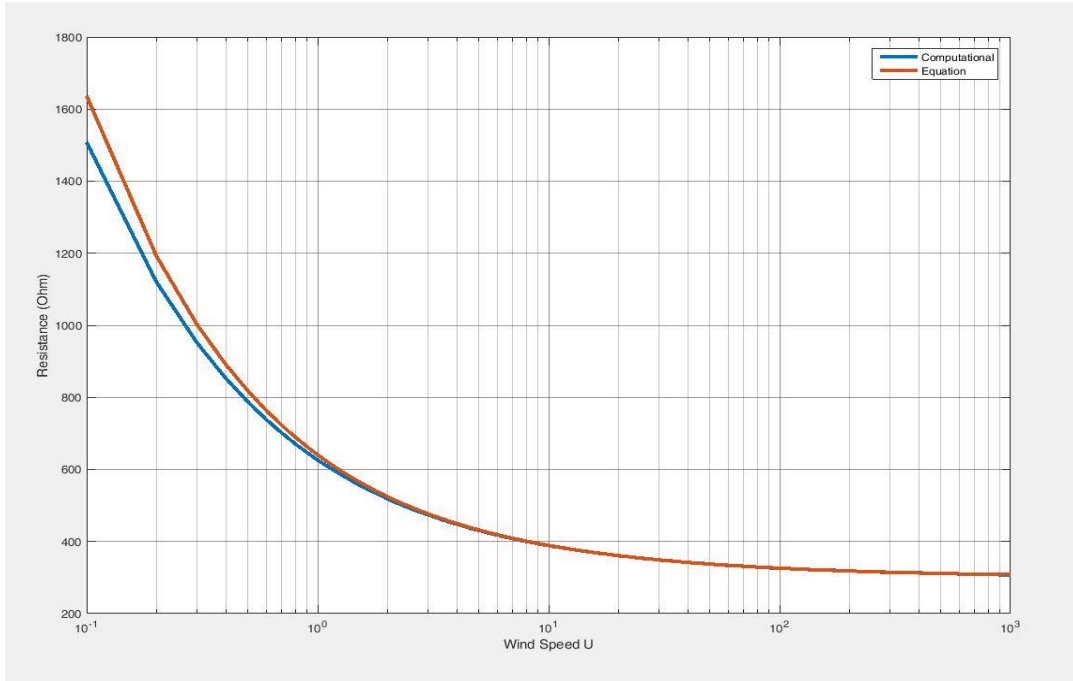
Figure 59. A comparison between the derived equation(red) and the simulated MPP locus(blue).

5.4. Voltage conditioning system

The main goal of the energy harvesting system is to deliver the sufficient power for a given sensor node, to be able to perform its task normally. This sufficient power depends on the node itself, its radio communication protocol and its scheduling. Technically speaking, the harvested signal must be transformed into a stable DC voltage, regulated to the level needed by the node. At the same time, the system has to sustain all the expected variations in the target load current, and from the input side it has to adapt to the variations of the wind speed applied to the harvester.

This goal requires the system to perform two tasks simultaneously:

- To ensure and optimize the power transfer from the harvester.
- Regulate and control the output signal to satisfy the target's needs.

The block diagram in Figure 60 describes the proposed system, showing the power flow and the function of different stages and sub circuits.

A low power microcontroller is used here for 3 purposes, first is to deliver a PWM signal to the DC/DC converter. 2nd is to monitor the input power and run an MPPT algorithm for optimization, and 3rd to communicate the power state with an external device via serial communication.
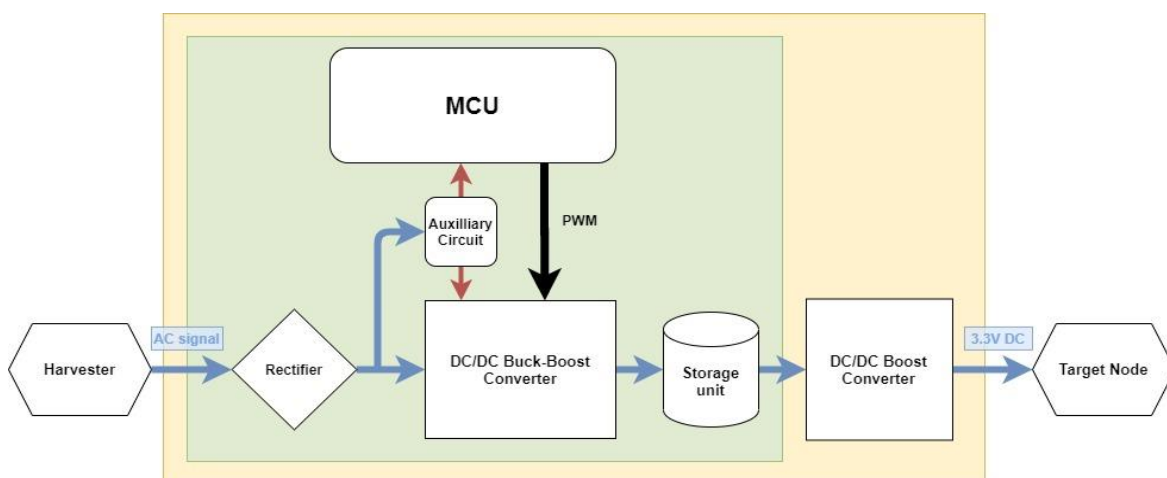
Figure 60. Block diagram of the proposed system

The input signal is split into two paths after being rectified, the auxiliary circuit consumes around 15% of the power and this value can vary depending on the consumption of the microcontroller and the different active components used in the circuit. The rest of the power goes into the main DC/DC buck-boost converter that has the main purpose of dynamically matching the input resistance to compensate for the weather conditions variation. The DC voltage is stored in the supercapacitor and then regulated to the required level using a second switching DC/DC converter. The choice of switching converters is made due to the fact that they provide high efficiency compared to passive regulators [46], [48]–[53].

Full wave rectifier: In order to transform an AC signal to DC, the first and most important stage is the signal rectification which outputs a positive voltage signal. The loss can vary depending on the type of rectifier, but this loss cannot be totally removed. The strategy used in this approach to minimize the loss is to replace the diodes with MOSFETs, a method that proved to reduce the losses caused by the voltage drop resulted from diodes to a certain extent.

A. DC/DC Buck-Boost converter: The topology in Figure 61 presents a non-inverting buck-boost DC/DC converter using 3 MOSFET switches. A 5 KHz PWM signal is applied to the switches with variable duty cycle that is controlled by the MPPT algorithm. The low switching frequency is chosen to keep the converter in DCM mode in the permanent phase, this allow the input equivalent resistance to always be expressed independently of the load, otherwise it could be problematic for the MPPT control. The reason for it is that in the CCM, the inductor current does not reach 0 during the discharge period but instead it reaches a value related to Vout, affecting the charged energy in the next cycle [54].
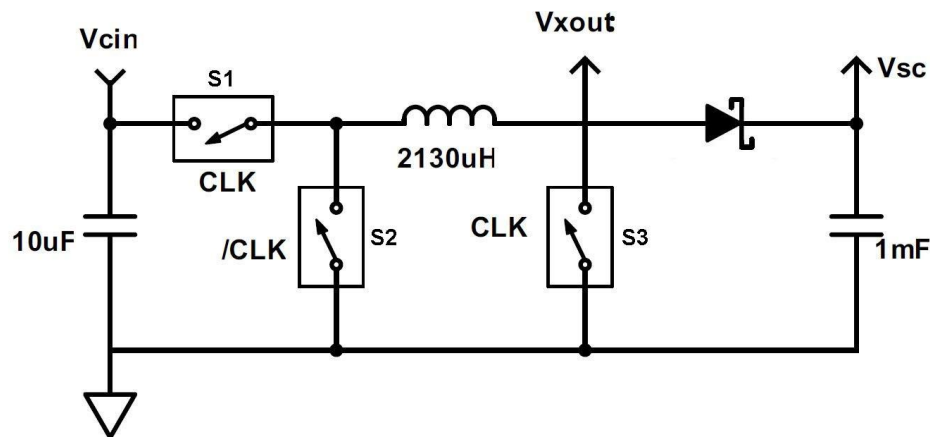
Figure 61. The proposed non-inverting DC/DC Buck-Boost converter.

$$R_{EQ} = \frac{2L}{D^2 t_{CK}} \tag{70}$$

From the model simulations we can deduce that the optimal resistance of the converter is always $> 300\Omega$, and therefore it can be deduced from the Equation (70) that the duty cycle should always be under 27%. The chosen inductor value is 2.13mH to satisfy the condition Ton $<<$ L/Rs [21] and reduce the losses inside the harvester's series resistance during Ton.
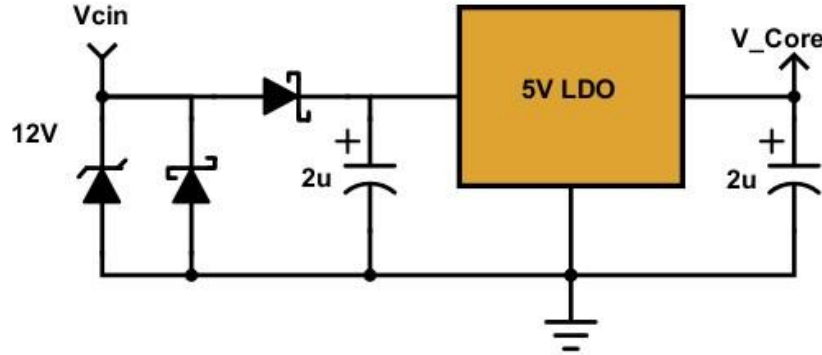
Figure 62. The auxiliary circuit used to provide a source for active components

These parameters have evolved throughout the different prototypes that were made.

B. Auxiliary circuit: This part of the system is responsible of powering all the active components in the circuit, including the MCU and MOSFETs. The rectified input signal is regulated passively with a low-dropout regulator LDO, to deliver a stable DC voltage as shown in Figure 62. Although passive regulators cannot provide a high efficiency, but it is necessary and important for the functioning of the system. For this reason the load on the auxiliary circuit must be as minimal as possible, in this case around 15% of the produced power.

C. Microcontroller: The microcontroller (MCU) is the part that monitors the voltages, runs the MPPT algorithm and controls the DC/DC converter through PWM signal. It is important for the MCU to have as low power consumption as possible, for the reason that the supply voltage is provided by the auxiliary circuit, and it consumes power through the inefficient LDO that reduces the power delivered to the super capacitor. The MCUs used are different with the different prototypes, the most recent one is the SiliconLabs

C8051F920, which contains a switching voltage regulator and can be powered with an 800mV input.

D. Super capacitor: The super capacitor is a more flexible storage unit than batteries, with a main drawback that is leakage current. In this system, the output current is not sufficient to charge commercial batteries like Li-Ion, and therefore a super capacitor can fit here. With the correct configuration, the super capacitor can charge-up during a fixed time period to store a sufficient energy that the application of interest needs. The charge and discharge follow this equation:

$$C = I_C \frac{\Delta t}{\Delta V} \tag{71}$$

This allows us to determine the value of the capacitor needed to supply a load with specific consumption profile and calculate the charging time as well.

5.5. System prototypes

Different prototypes were produced in the COSMIC lab for the purpose of testing and conducting experiments with the harvester. The experiments were made using virtual input signals produced by AC and DC signal generators, computer generated signals, as well as experiments using the
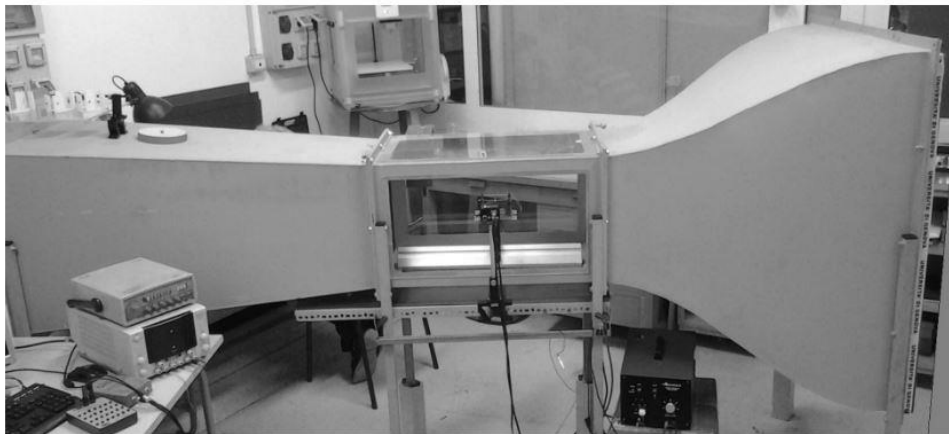
Figure 63. The controllable wind tunnel used to conduct the experiments.

wind tunnel in the department of physics DIFI (Figure 63).

These experiments proved useful during the course of research, they highlighted multiple wrong decisions and their effects on the behavior and functionality of the system. Moreover, they raised many challenges that were not existing during the design and simulation of the system. These challenges were either related to the design itself where careful attention has to be taken with all the details, the compatibility of the components used in the system, the manufacturing costs and effort, etc..

5.5.1 First version

The first prototype was made to test the main DC/DC Buck-boost converter (Figure 64). The layout is shown in Figure 65, it consists of a full wave rectifier made with BAT54S Schottky diodes. Followed by our configuration for a non-inverting buck-boost converter that contains 3 low power MOSFET switches. The input capacitor C1 acts as a low pass filter to remove the noise from the rectified signal with a capacitance of 10μF. The switches SW1 and SW2
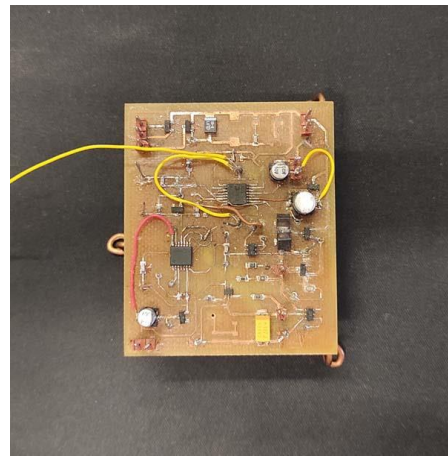
Figure 64. The first prototype.
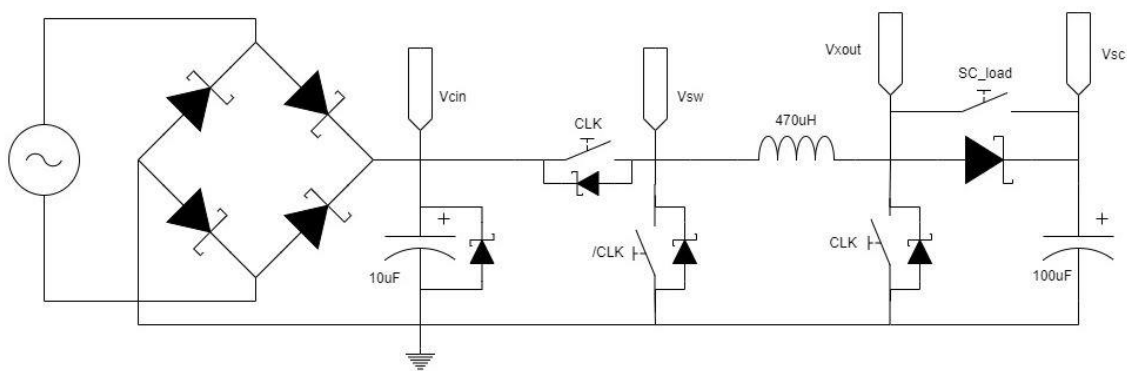
Figure 65. Circuit layout of the first prototype.

are integrated in the IC ADG1213 that contains 4 low resistance switches, while the switch SW3 uses a different IC (ADG801). The reason is that the voltage powering the ICs in this circuit is 5V,

but SW1 and SW2 might be exposed to higher voltages in the loop before the inductor. This will bias the protection diodes inside the ICs and disturb their functionality. The solution is to use ADG1213 which takes an input voltage of 12V to avoid this phenomena, assuming that the input voltage on C1 will not exceed 12V. These switches are clocked by the PWM signal CLK and its complement /CLK which are provided externally by a pic18F14K22 microcontroller.

Figure 66. The proposed current direction sensing circuit.

The diode in the output loop is a schottky diode BAT54S that is bypassed by a MOSFET switch driven by the circuit in Figure 66. This circuit is designed to function as an active diode. The anode

Figure 67. Plot of the signals from different points in the current direction sensing circuit, nodes S,R,VSCL and Vxout.

and cathode nodes Vsw and Vxout are connected to a comparator in a configuration that senses the current direction. And then a signal triggers the RS latch to send a signal SC_load that closes the switch Sw4 in synchronization with the main PWM signal CLK. Figure 67 shows the CLK signal along with the signals on the latch input R and S, and the signals SC_load and Vxout. The signal SC_load remains high for the duration Td where a current is flowing through the inductor.

A remark in this configuration is that a change in the current is detected when the difference between Vxout and Vsc becomes small, and that occurs before the current actually changes direction, what makes the switch SW4 open early and therefore the output diode is biased for a brief period, which is not the wanted behavior. To try and solve this problem, the voltage divider on the comparator's negative input can be tuned to find the sweet spot.

5.5.2 Second version

The second prototype (Figure 68) was made to study the difference between 2 types of bridge rectifiers, and the effect of including an auxiliary circuit to power up the active components. The full-wave bridge rectifier made from Schottky diodes is consuming power through the voltage drop across the diodes. Using diodes this drop can be minimized to 300mV per diode as a minimum

Figure 68. The second prototype.

value. While using MOSFET transistors instead can lead to less voltage drop and therefore a lower power consumption. Many systems have MOSFETs instead of diodes in their rectifier, with different configurations being used. Some configurations are based on comparators that sense the current direction to feed the MOSFET gates, while in this circuit another configuration is tested in parallel of a diode passive rectifier. As seen in Figure 69, each side of the input is connected to a P-channel and an N-channel MOSFETS respectively substituting the in and out diodes, and the gates are fed by the opposite polarity node.
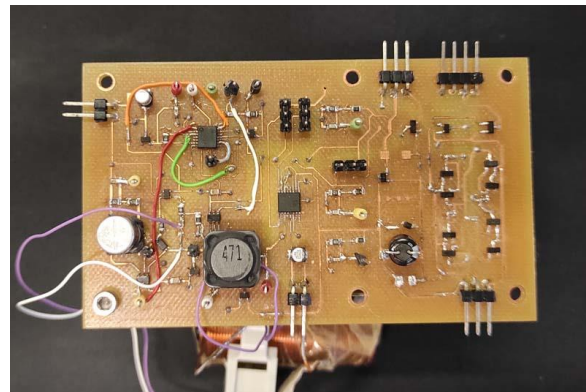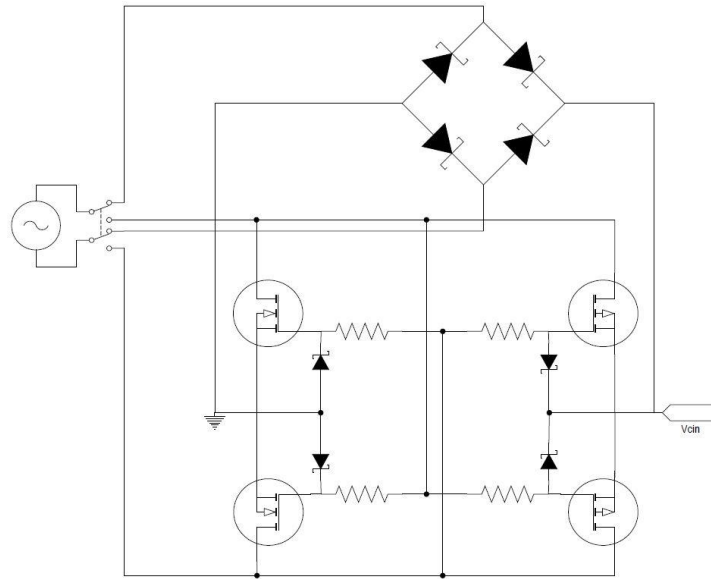
Figure 69. The proposed bridge rectifier topology in the second prototype.

The MOSFET bridge showed to have a lower power consumption that the other, but some oscillations were present with the input signal due to the internal capacitance of the combined
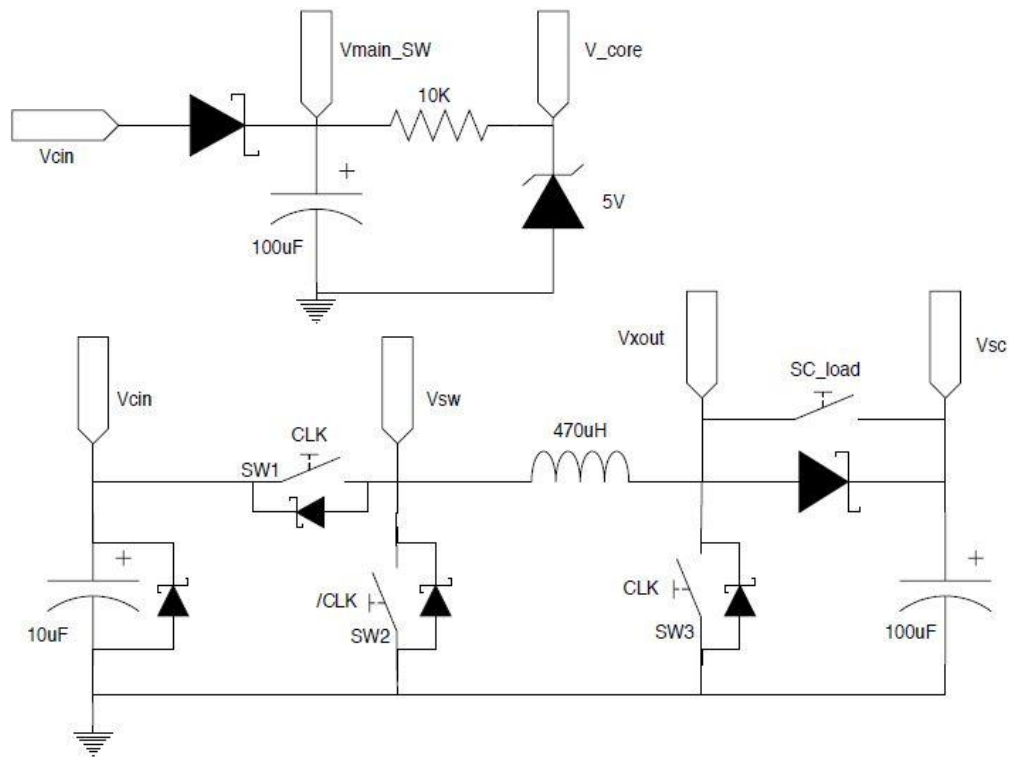

*Figure 70. Circuit layout of the second prototype.*

transistors, what required the use of a high value protection resistors at the MOSFETs gates.

The auxiliary circuit was introduced in this version, its role is to provide a voltage source (Vmain_SW and V_core) to the active components in the circuit mainly the ADG1213, ADG801 and ADG802 low power switches. The 5V zener diode regulates V_core at 5 while Vmain_SW that is powering the ADG1213 is allowed to be higher, for reason discussed above. Figure 70 shows the schematic of the circuit, where the main DC/DC converter is not changed from the first version of the circuit (see Figure 64). The current sensing circuit is not shown in the figure but it is mostly the same as in the previous circuit (Figure 66).

5.5.3 Third version

In this prototype shown in Figure 71, a lot of changes took place. The goal of this prototype is to test the ability of powering a microcontroller, and to evaluate two different active diode circuits.

A low power microcontroller pic 16F1788 was integrated in the board with a UART serial communication module, and powered from the auxiliary circuit (V_core). The
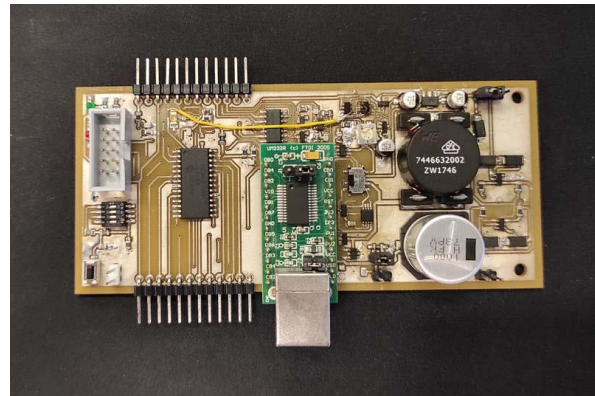
Figure 71. The third prototype.

microcontroller is programmed to read the voltage from the node Vcin, and run the MPPT algorithm to adapt the PWM duty cycle. Since the 5V zener diode was consuming a significant amount of power, and V_core is expected to draw more current after the introduction of the microcontroller, it is replaced with a 5V Low Dropout regulator LDO (Figure 72). The duty cycle is controlled by a 10 bit register, and depending on the main oscillator the quantization error can increase. While the MPPT algorithm is running, the minimum equivalent resistance that could be needed is 300Ω, which means that the duty cycle has to be below 12.5% at all times. For this reason, the value of the inductor was increased to 2.3mH so that the duty cycle can be controlled

in a wider range while maintaining the Discontinuous Conduction Mode DCM. The value of the super capacitor is increased to 1mF to match.

For the output diode, two different configurations were tested, the first is the previous current sensing circuit with a potentiometer to tune the voltage divider, and the other consists of an N-
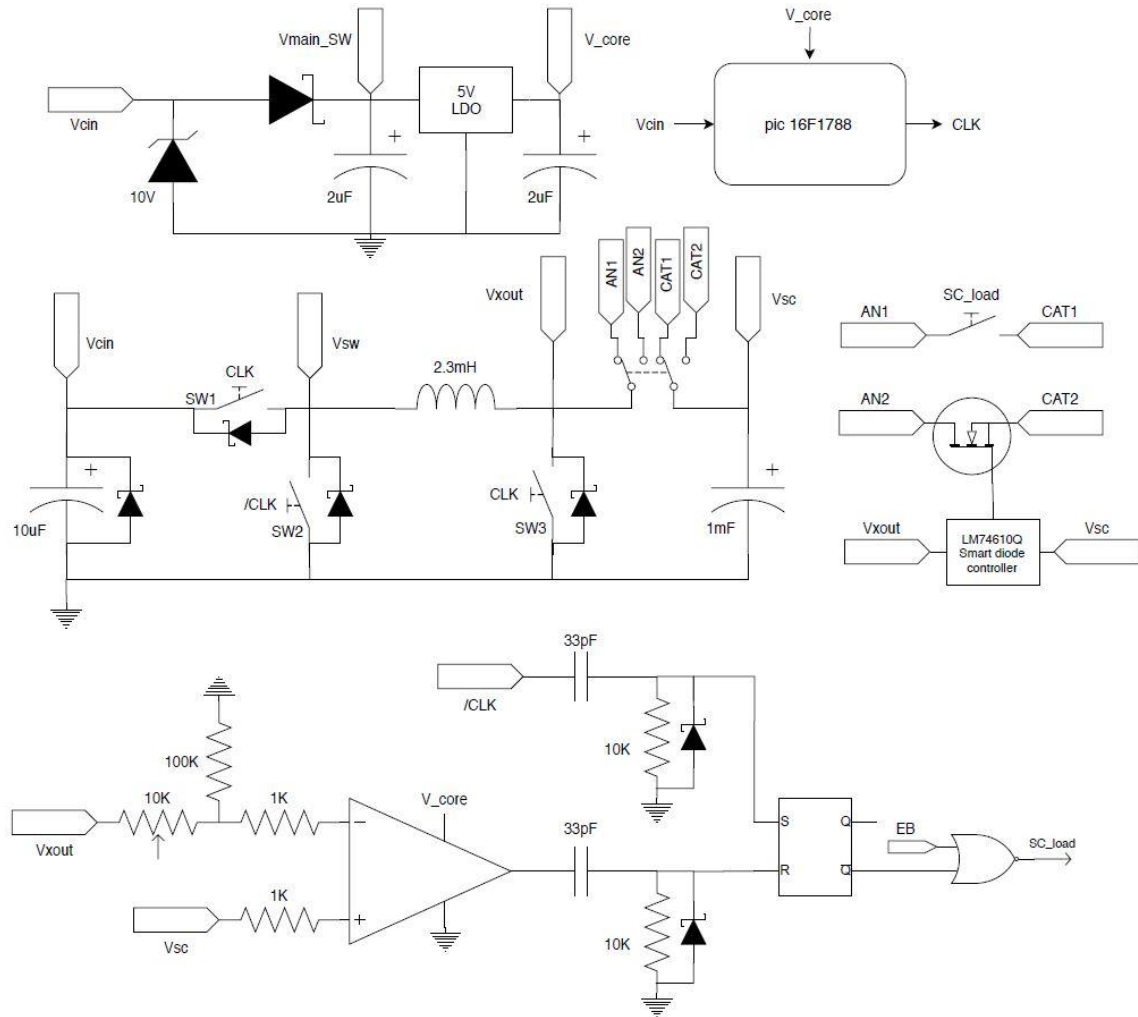
Figure 72. Circuit layout for the third prototype.

channel MOSFET with a smart diode controller IC from TI LM74810Q. The latter proven more useful due to the fact that a reverse-polarity protection function is integrated within the IC that

prevents any current from flowing backwards while the active diode is forward biased, which occurs in the case of the current sensing circuit as the inductor current goes to zero.
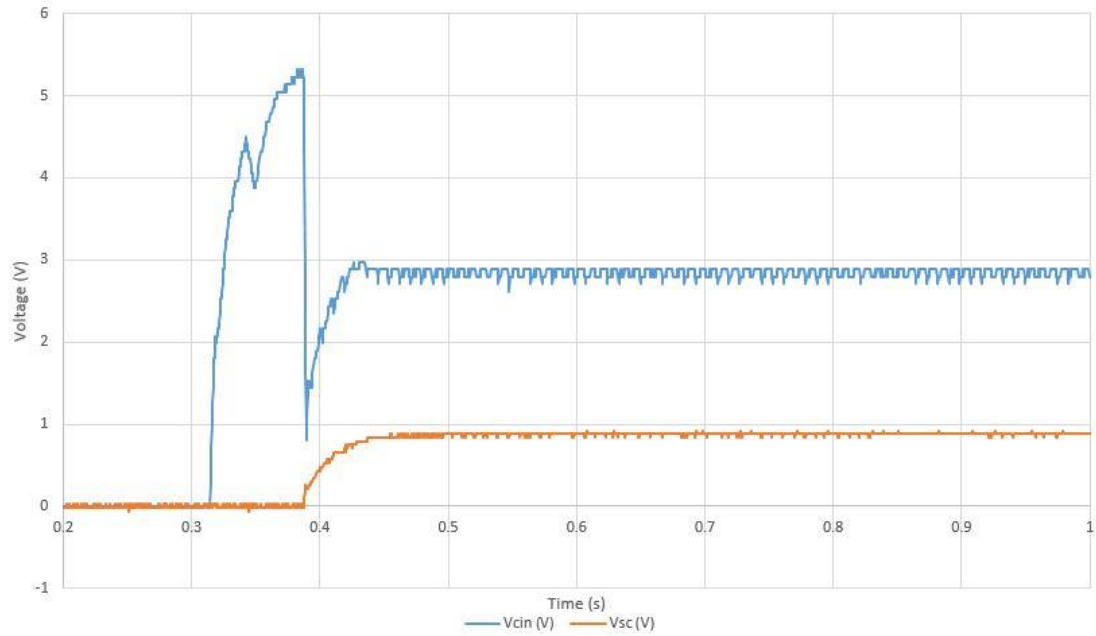
(a)
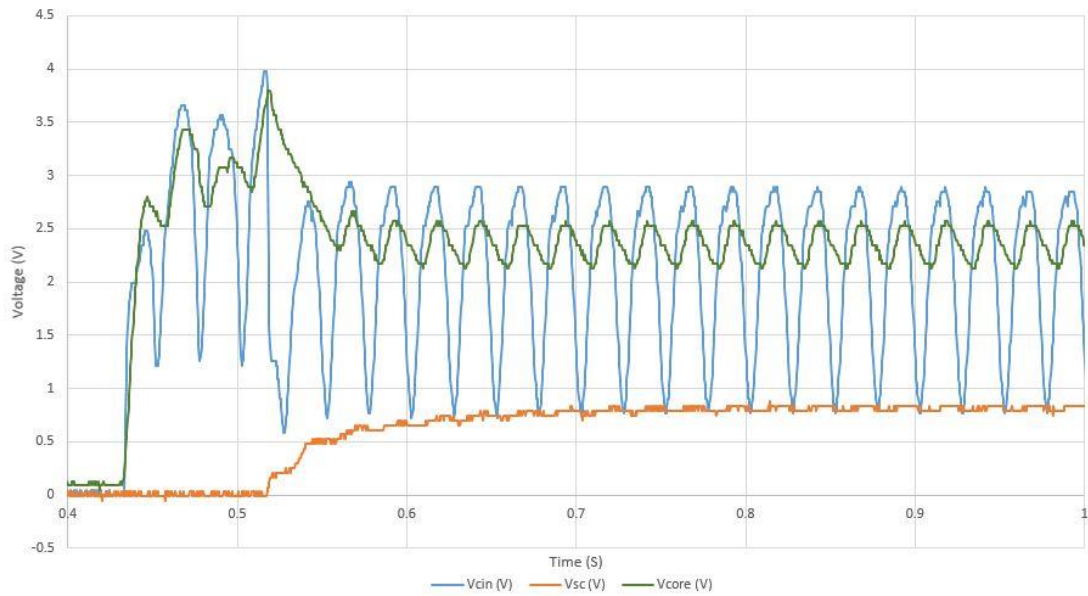
(b)

Figure 73. The transient behavior of the input and output voltges of the circuit for (a) DC input, and (b) Ac input.
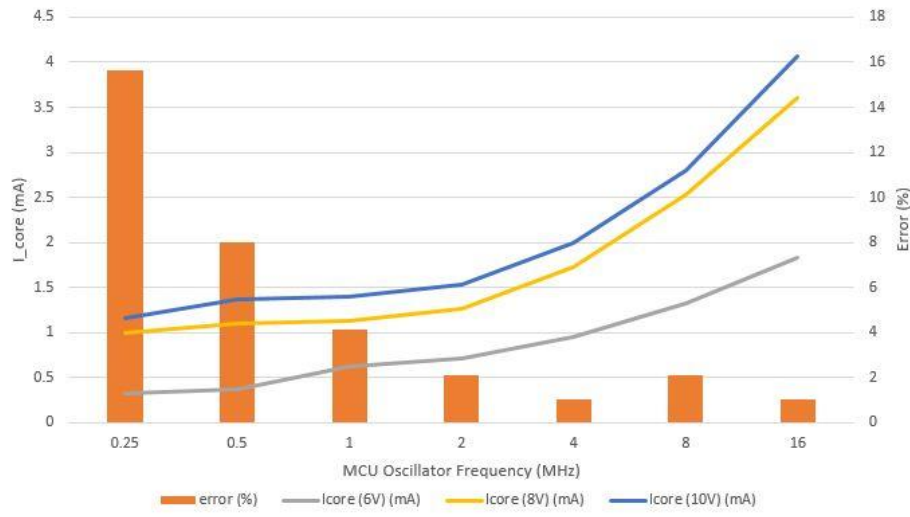
(a)
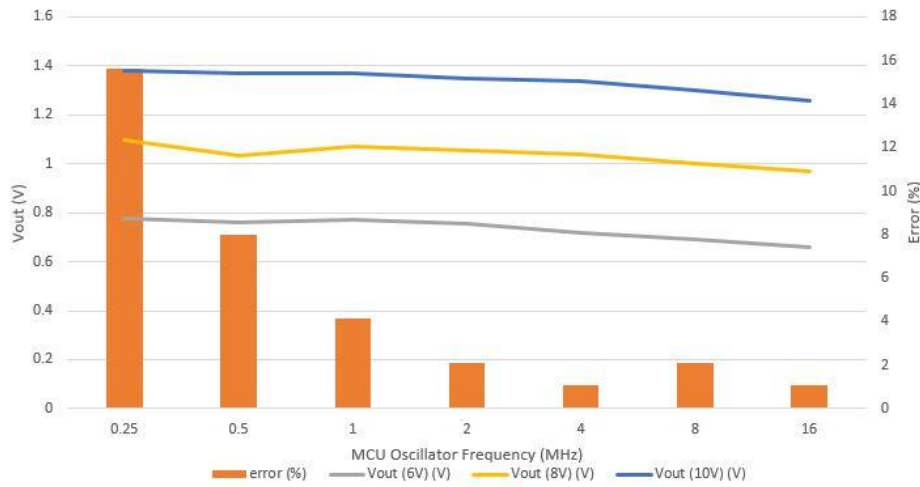
(b)

Figure 74. (a) the current consumed by the MCU versus the sampling error resulting from different oscillator frequencies. (b) The output voltages versus sampling error for different OSC frequencies.

Experiments with DC and AC inputs were made to evaluate the efficiency of the circuit, and the effect of powering the microcontroller from the auxiliary circuit. Figure 73(a) shows the transient input and output of the system for 6V DC input and 47Ω output load, while Figure 73(b) shows the transient for 6Vp-p AC input with a 120Ω load. The efficiency calculation of the DC/DC converter for both inputs can be seen in Table 3, as well as the power consumed by the microcontroller.

	Vcin_rms (V)	V_core_rms (V)	I_core (mA)	Pin (mA)	Pout (mA)	Ppic (mA)	Eff (%)	Eff_no_mcu (%)
DC	2.9	2.37	1.067	27.229091	18.253498	2.52879	67.04	76.32
AC	2.215048255	2.33	0.867	14.867996	6.473508	2.02011	43.54	57.13

Table 3. Power and efficiency calculation for DC and AC input voltges.

It is possible to further decrease the power consumption through lowering the frequency of the internal oscillator of the microcontroller. This comes with the tradeoff of increasing the quantization error on the duty cycle.

Experiments were made to show the effect of changing the frequency of oscillation Fosc in the pic16F1788. The current consumed by the MCU is recorded and shown in Figure 74(a), while the output voltage is shown in Figure 74(b), where the orange bars show the quantization error, and different curves represent different input voltages.

5.5.4 Fourth version

The goal of this prototype is to study the ability of the converter to handle a boost regulator at the output, and to deal with different load requirements (Figure 75).

The Differences between this prototype and the previous one is that the smart diode IC is adopted for the output diode, and a boost regulator MP28164 is connected to the super capacitor and

Figure 75. The fourth prototype.

configured to output a 3.3V (Figure 76). This regulator has a double threshold for the input voltage, it is able to startup at 1.8V and will shutdown at 0.8V.
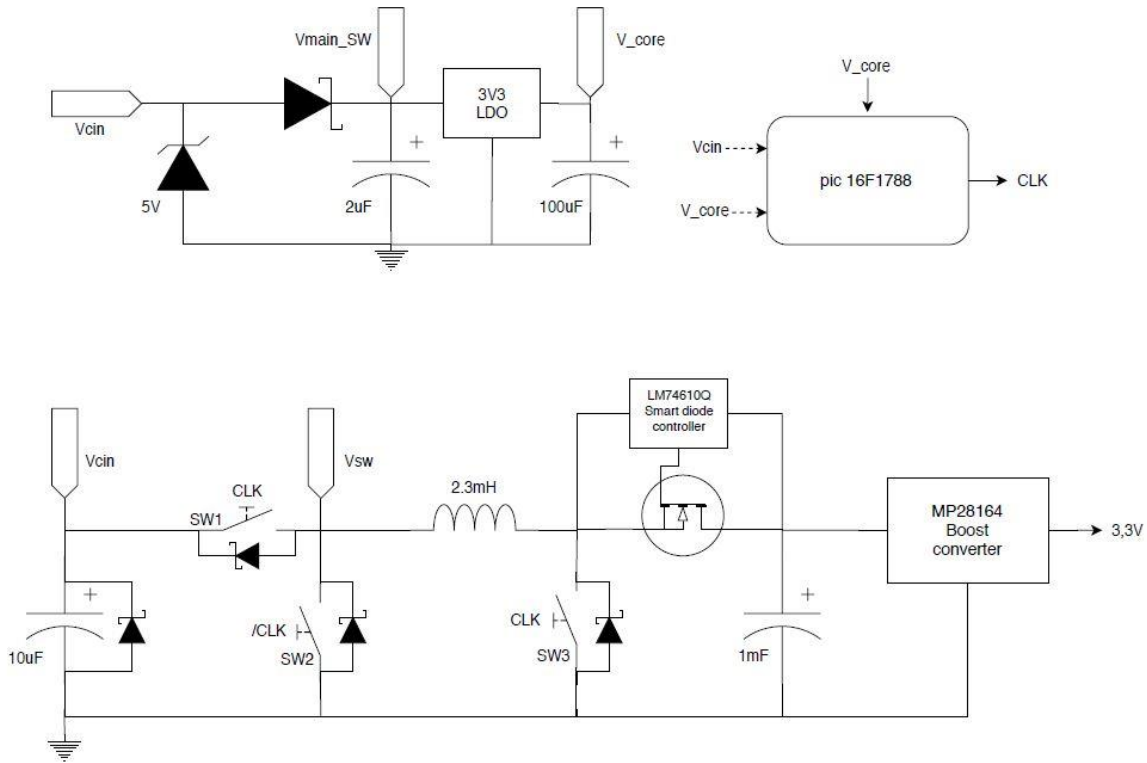
Figure 76. Circuit layout for the fourth prototype.

The microcontroller in this prototype monitors two voltage points, Vcin and V_core for the purpose of power management. Whenever the MPPT algorithm increases the duty cycle to find an optimal point, the input voltage Vcin decreases due to the decrease in the equivalent resistance value. This can lead to a situation where the voltage available for the MCU is not enough to stay
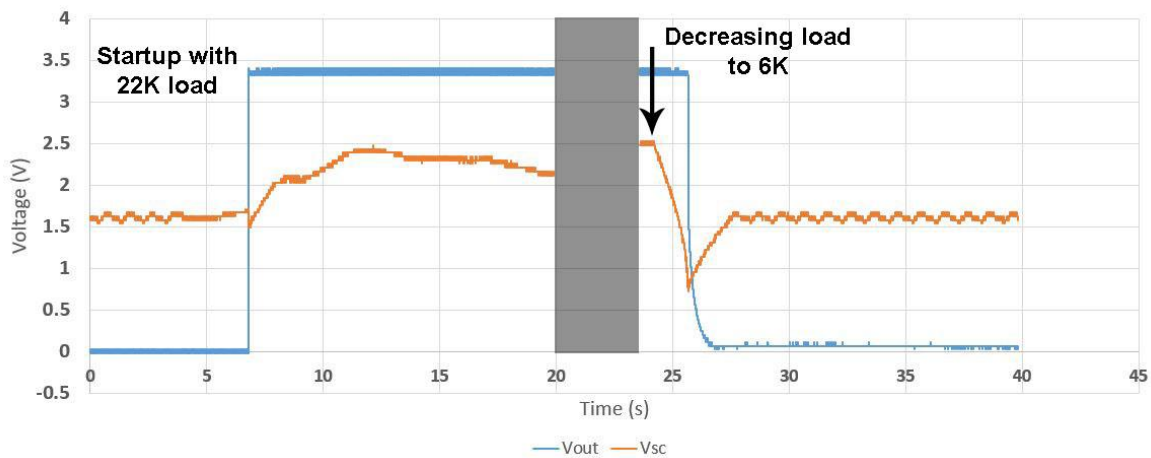
Figure 77. Plot sohowing the outpout voltage drop with the introduction of a new load..

on, and after it shuts down the equivalent resistance increases again to repeat the whole phenomena and stay in this loop. The power management algorithm can solve this problem by monitoring the microcontroller's source voltage V_core and enters a power saving state whenever the voltage passes a threshold. The power saving maintain the lowest duty cycle possible to ensure the availability of high voltage on the input. Another threshold is set to allow the transition to the normal MPPT state. Note that the power saving state does not ensure an optimal power transfer but it is mandatory to keep the system working in low input power situation.

Experiments in the wind tunnel were performed on this prototype, and the system was tested with different loads. Figure 77 shows the super capacitor voltage along with the output voltage of the system under a wind speed of 2.4m/s. The circuit is initiated with a load of 22KΩ and after the super capacitor has stored enough energy to trigger the output converter, a load of 6KΩ is introduced, representing a current consumption of 550µA. The super capacitor discharges in around 2 sec following the relation:

$$C = I_C \frac{\Delta t}{\Delta V}$$

(72)

Where Ic can be approximated from the rated efficiency of the DC/DC converter.

This experiment shows the mechanism on a small scale while in the typical application, a correct super capacitor value must be calculated to sustain the needed current for the needed duration, and the charging time can be also deduced respectively and so on.

5.5.5. Fifth version

This prototype (Figure 79) did not see changes in the main DC/DC converter, but instead a different microcontroller is used. The Silicon Labs C8051F20 is a low power microcontroller that is able to run with a voltage source of 1.8 V, and contains an internal DC/DC boost converter with the ability to output a regulated voltage signal. This is useful to replace the auxiliary circuit and provide a source for the active circuit components through the MCU.

Figure 79. The fifth prototype.

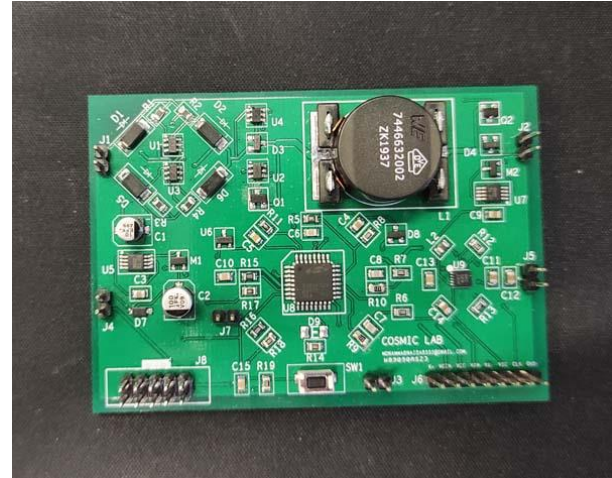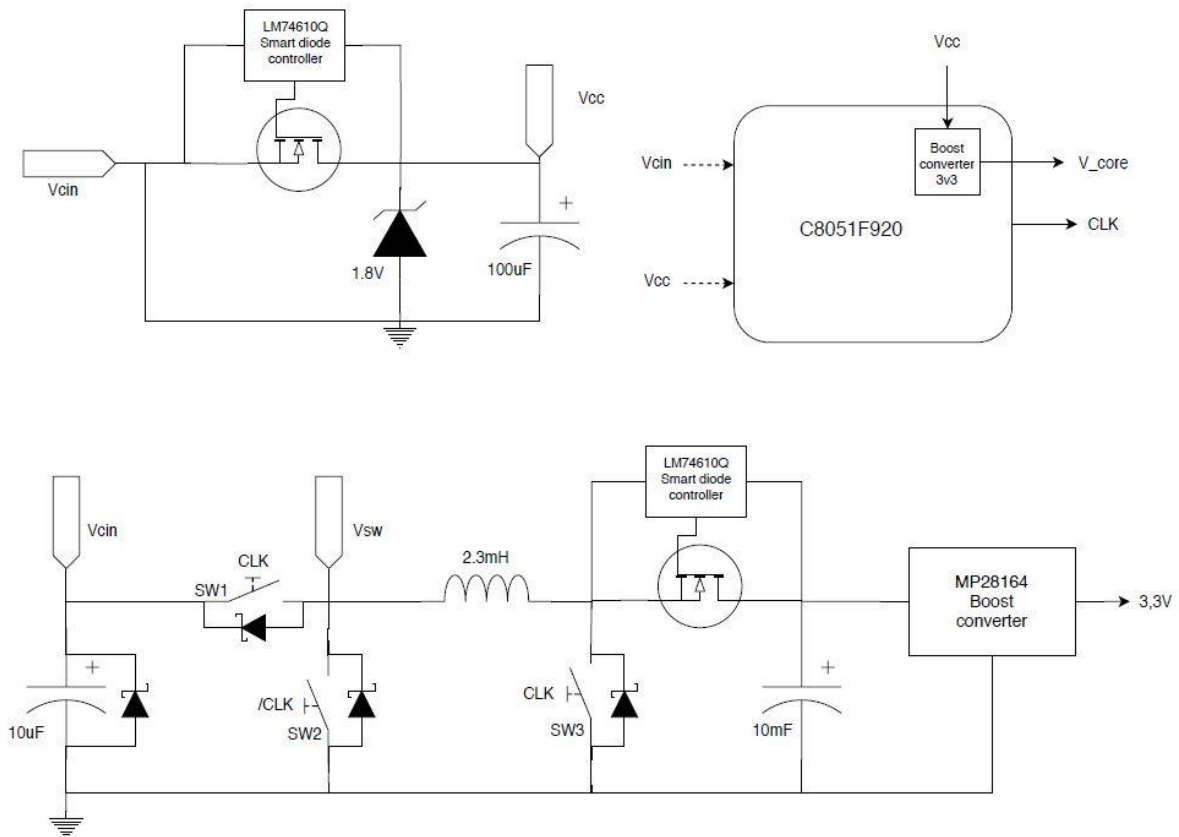*Figure 78. Circuit layout for the fifth prototype.*

The new microcontroller will be beneficial by reducing the power that was consumed by the auxiliary circuit in the previous prototypes, and by acting as a replacement to the passive voltage regulator for the reason that the integrated DC/DC boost converter is more efficient that low dropout regulators LDOs.

The small auxiliary circuit to power the MCU is designed with an active diode using the smart diode controller as it has proven useful and more efficient that a Schottky diode, along with an 1.8V Zener diode as seen in Figure 78. The super capacitor seen in the figure has a value of 10mF but it is replaceable to fulfill the needs of the load following the equation (72). This prototype is yet to be used in experiments involving real LPWAN sensor nodes for future work, and no experiments has been made yet.

5.6. Conclusion

This chapter presented a detailed description and analysis of the FLEHAP converter's electrical behavior. The voltage signal produced by this device contains multiple harmonics that depend on the wind speed applied to it. A mathematical model was derived, involving the magnetic circuit and FEMM simulator to describe the relation between different parameters and the final resulted output voltage, for the purpose of having an available model to perform simulations. Another mathematical model was derived to describe the behavior of the output power that is available with the presence of a load and inherently a feedback phenomenon. The model was useful to show that the optimal load has a minimum value, which is equal to the harvester's internal resistance.

A detailed description of the voltage conditioning system was shown. The system is necessary to convert the output voltage form the wind harvester to a useful DC voltage, and to perform the task in an efficient manner. It involves a full wave bridge rectifier, followed by a DC/DC buck-boost converter, the energy is stored in a super capacitor and regulated using a boost regulator. A low power microcontroller is powered from the same harvester is used to perform an MPPT algorithm and optimize the transferred power.

Different prototypes were made in the COSMIC lab for the purpose of experiment. Some experiments were made in a controllable wind tunnel, and other were conducted using signal generators and computer-generated signals. Five prototypes were shown with detailed description, along with the experiment results that were recorded.

Chapter 6.   Conclusion and Future Work

This research thesis dealt with the problem of providing a reliable power source for low-power sensor nodes. Analysis and description of the problem was discussed, along with the suggested solutions and the experiment conducted to validate their viability.

First, the importance of Wireless Sensor Networks was discussed from in the application and design point of view, as well as the relation to the IoT field that is growing nowadays. The main challenge in power consumption and management was highlighted. Renewable energy, being one of the most promising solutions was studied and a brief description of the different form of energy harvesters was described long with their advantages.

Digging into the power extraction, the main techniques that rely on switching power converters were investigated, the developed mathematical models allowed to simulate the behavior of different circuit components, and locate the sources of power loss allowing to find solutions and increase the overall efficiency of the system.

In order to optimize the power transfer between the harvester and the interface circuit, Maximum Power Point Tracking MPPT were investigated, and simulations of the P&O algorithm led to development of other algorithms derived from the original one, to fit our application and compensate for some weak points that were eventually discovered. The new algorithm was implemented on a low power MCU, and experiments confirmed the viability of such algorithm to meet the desired goals while maintaining speed and stability.

Following-up on the algorithm implementation, the problem of voltage and power monitoring in the electronic interface was addressed. The dynamic nature of the signal imposed some issues in power reading. Solutions were proposed and tested including the implementation of Kalman filter to predict the power reading. The solutions proved useful in the simulations and were implemented in different prototypes that were developed in the lab.

The thesis also presented a description of the system that was proposed as a power converting interface for the FLEHAP device. The wind harvester device was briefly investigated highlighting the important characteristics that carried out and influenced the electrical circuit. The dynamics

between the mechanical and electrical parts of the system were modeled to provide a basic framework allowing to perform simulations and virtually validate the proposed concepts.

Five prototypes were manufactured in the COSMIC lab for the purpose of experiment, these prototypes were built on top of each other, introducing new concepts and getting rid of power loss sources what helped improving the overall efficiency. Some experiments were made in a controllable wind tunnel, and other were conducted using signal generators and computer-generated signals. The results were described and discussed.

A lot of room for future work is open. It is noticeable that the customization of the interface circuit can further improve the performance and efficiency of the power transfer, what can be studied further in details and built upon.

Another improvement can be summarized by compensating for the inconsistency of the energy available to the harvester, and this is done with the introduction of other forms of harvesters in parallel to the existing one. Making the system a hybrid energy harvester, but imposes also additional challenges in dealing with the different produced signals, and with the physical constraints that are hard to follow.

References

[1] I. F. Akyildiz, W. Su, Y. Sankarasubramaniam, and E. Cayirci, "Wireless sensor networks: A survey," *Comput. Networks*, 2002, doi: 10.1016/S1389-1286(01)00302-4.

[2] M. Tubaishat and S. Madria, "Sensor networks: An overview," *IEEE Potentials*, vol. 22, no. 2. 2003, doi: 10.1109/MP.2003.1197877.

[3] J. Yick, B. Mukherjee, and D. Ghosal, "Wireless sensor network survey," *Comput. Networks*, 2008, doi: 10.1016/j.comnet.2008.04.002.

[4] A. Boukerche, *Algorithms and Protocols for Wireless and Mobile Ad Hoc Networks*. 2008.

[5] K. Sohraby, D. Minoli, and T. Znati, *Wireless Sensor Networks: Technology, Protocols, and Applications*. 2006.

[6] C. Buratti, A. Conti, D. Dardari, and R. Verdone, "An overview on wireless sensor networks technology and evolution," *Sensors*. 2009, doi: 10.3390/s90906869.

[7] R. Verdone, D. Dardari, G. Mazzini, and A. Conti, *Wireless Sensor and Actuator Networks*. 2008.

[8] W. R. Heinzelman, A. Chandrakasan, and H. Balakrishnan, "Energy-efficient communication protocol for wireless microsensor networks," 2000, doi: 10.1109/hicss.2000.926982.

[9] A. Manjeshwar and D. P. Agrawal, "TEEN: A routing protocol for enhanced efficiency in wireless sensor networks," 2001, doi: 10.1109/IPDPS.2001.925197.

[10] A. Manjeshwar and D. P. Agrawal, "APTEEN: A hybrid protocol for efficient routing and comprehensive information retrieval in wireless," 2002, doi: 10.1109/IPDPS.2002.1016600.

[11] S. L. Raghavendra and C., "PEGASIS: Power-Efficient Gathering in Sensor Information Systems," *IEEE Aerosp. Conf. Proc.*, 2002.

[12]   C. Intanagonwiwat, R. Govindan, D. Estrin, J. Heidemann, and F. Silva, "Directed diffusion for wireless sensor networking," *IEEE/ACM Trans. Netw.*, 2003, doi: 10.1109/TNET.2002.808417.

[13]   Y. Xu, J. Heidemann, and D. Estrin, "Geography-informed energy conservation for ad hoc routing," 2001, doi: 10.1145/381677.381685.

[14]   S. Nundrakwang, P. Yingyong, and D. Isarakorn, "Energy harvesting for self-powered systems," 2020, doi: 10.1109/ICEAST50382.2020.9165350.

[15]   R. J. M. Vullers, R. van Schaijk, I. Doms, C. Van Hoof, and R. Mertens, "Micropower energy harvesting," *Solid. State. Electron.*, 2009, doi: 10.1016/j.sse.2008.12.011.

[16]   G. D. Szarka, B. H. Stark, and S. G. Burrow, "Review of power conditioning for kinetic energy harvesting systems," *IEEE Trans. Power Electron.*, vol. 27, no. 2, pp. 803–815, 2012, doi: 10.1109/TPEL.2011.2161675.

[17]   B. H. Stark, P. D. Mitcheson, P. Miao, T. C. Green, E. M. Yeatman, and A. S. Holmes, "Converter circuit design, semiconductor device selection and analysis of parasitics for micropower electrostatic generators," *IEEE Trans. Power Electron.*, 2006, doi: 10.1109/TPEL.2005.861113.

[18]   Analog Devices, "Practical Design Techniques for Power and Thermal Management," pp. 1–21, 1998, [Online]. Available: http://www.analog.com/media/en/training-seminars/design-handbooks/ptmoutline.pdf.

[19]   M. Moallem, C.-Y. Hsieh, and F. Golnaraghi, "Bridgeless converter with input resistance control for low-power energy harvesting applications," *IET Power Electron.*, vol. 8, no. 5, pp. 822–830, 2015, doi: 10.1049/iet-pel.2014.0283.

[20]   M. J. HASAN, M. H. ISLAM, and Q. TAREQ, "High Efficiency Boost Rectifier (Bridgeless) For Energy Harvesting," *Int. J. Adv. Res. Electr. Electron. Instrum. Eng.*, 2014, doi: 10.15662/ijareeie.2014.0310041.

[21]   G. Boccalero, C. Boragno, D. D. Caviglia, and R. Morasso, "FLEHAP: A Wind Powered Supply for Autonomous Sensor Nodes," *J. Sens. Actuator Networks*, vol. 5, no. 4, p. 15, 2016, doi: 10.3390/jsan5040015.

[22] G. Boccalero, C. Boragno, R. Morasso, and D. D. Caviglia, "A Sensor Node Driven by Air Flow," 2017, pp. 65–68, doi: 10.1109/NGCAS.2017.26.

[23] S. Chamanian, U. Uluˏsan, A. Muhtaroˇ, and H. Külah, "Power-Efficient Hybrid Energy Harvesting System for Harnessing Ambient Vibrations," *IEEE Trans. CIRCUITS Syst. Regul. Pap.*, vol. 66, no. 7, 2019, doi: 10.1109/TCSI.2019.2900574.

[24] G. Boccalero and C. Boragno, "DEVELOPMENT OF A NOVEL COUPLED-MODE DEVELOP MODE FLUTTERING ENERGY HARVESTER THROUGH ELECTROMAGNETIC COUPLING AND," no. December, 2017.

[25] H. L. Dai, A. Abdelkefi, U. Javed, and L. Wang, "Modeling and performance of electromagnetic energy harvesting from galloping oscillations," *Smart Mater. Struct.*, vol. 24, no. 4, 2015, doi: 10.1088/0964-1726/24/4/045012.

[26] M. Haidar, H. Chible, E. Di Zitti, and D. D. Caviglia, "An Optimized AC/DC Buck-Boost Converter for Wind Energy Harvesting Application," in *2019 IEEE International Conference on Environment and Electrical Engineering and 2019 IEEE Industrial and Commercial Power Systems Europe (EEEIC / I&CPS Europe)*, Jun. 2019, no. August 2000, pp. 1–4, doi: 10.1109/EEEIC.2019.8783648.

[27] M. Haidar, H. Chible, R. Morasso, and D. D. Caviglia, "AC/DC Buck Boost Converter for Wind-Powered Wireless Sensors," in *2019 15th Conference on Ph.D Research in Microelectronics and Electronics (PRIME)*, Jul. 2019, pp. 41–44, doi: 10.1109/PRIME.2019.8787790.

[28] D. Maurath, C. Peters, T. Hehn, M. Ortmanns, and Y. Manoli, "Highly efficient integrated rectifier and voltage boosting circuits for energy harvesting applications," *Adv. Radio Sci.*, vol. 6, pp. 219–225, 2008, doi: 10.5194/ars-6-219-2008.

[29] Y. Tan and S. Panda, "Optimized Wind Energy Harvesting SystemUsing Resistance Emulator and Active Rectifierfor Wireless Sensor Nodes," *Power Electron. IEEE Trans.*, vol. 26, no. 1, p. 1, 2011, [Online]. Available: http://ieeexplore.ieee.org/xpls/abs_all.jsp?arnumber=5524087.

[30] D. Porcarelli, D. Spenza, D. Brunelli, A. Cammarano, C. Petrioli, and L. Benini,

"Adaptive rectifier driven by power intake predictors for wind energy harvesting sensor networks," *IEEE J. Emerg. Sel. Top. Power Electron.*, vol. 3, no. 2, pp. 471–482, 2015, doi: 10.1109/JESTPE.2014.2316527.

[31] R. Aubrée, F. Auger, M. Macé, and L. Loron, "Design of an efficient small wind-energy conversion system with an adaptive sensorless MPPT strategy," *Renew. Energy*, vol. 86, pp. 280–291, 2016, doi: 10.1016/j.renene.2015.07.091.

[32] W. Peng, L. Feng, and S. Yongduan, "A novel maximum power point tracking control method in wind turbine application," *32nd Chinese Control Conf.*, pp. 7569–7574, 2013.

[33] N. Femia, G. Petrone, G. Spagnuolo, and M. Vitelli, "Optimization of perturb and observe maximum power point tracking method," *IEEE Trans. Power Electron.*, vol. 20, no. 4, pp. 963–973, 2005, doi: 10.1109/TPEL.2005.850975.

[34] J. Yaoqin, Y. Zhongqing, and C. Binggang, "A new maximum power point tracking control scheme for wind generation," *Int. Conf. Power Syst. Technol.*, pp. 144–148, 2002, doi: 10.1109/ICPST.2002.1053521.

[35] D. Kumar and K. Chatterjee, "A review of conventional and advanced MPPT algorithms for wind energy systems," *Renew. Sustain. Energy Rev.*, vol. 55, pp. 957–970, 2016, doi: 10.1016/j.rser.2015.11.013.

[36] Q. Wang and L. Chang, "An intelligent maximum power extraction algorithm for inverter-based variable speed wind turbine systems," *Power Electron. IEEE Trans.*, vol. 19, no. 5, pp. 1242–1249, 2004, doi: 10.1109/TPEL.2004.833459.

[37] J. Singh and M. Ouhrouche, "MPPT Control Methods in Wind Energy Conversion Systems," in *Fundamental and Advanced Topics in Wind Power*, 2011.

[38] M. M. Algazar, H. Al-Monier, H. A. El-Halim, and M. E. E. K. Salem, "Maximum power point tracking using fuzzy logic control," *Int. J. Electr. Power Energy Syst.*, vol. 39, no. 1, pp. 21–28, 2012, doi: 10.1016/j.ijepes.2011.12.006.

[39] H. Li, K. L. Shi, and P. G. McLaren, "Neural-network-based sensorless maximum wind energy capture with compensated power coefficient," *IEEE Trans. Ind. Appl.*, vol. 41, no. 6, pp. 1548–1556, 2005, doi: 10.1109/TIA.2005.858282.

[40]   S. A. Kalogirou, "Artificial neural networks in renewable energy systems applications: A review," *Renewable and Sustainable Energy Reviews*. 2000, doi: 10.1016/S1364-0321(01)00006-5.

[41]   P. Flores, A. Tapia, and G. Tapia, "Application of a control algorithm for wind speed prediction and active power generation," *Renew. Energy*, 2005, doi: 10.1016/j.renene.2004.07.015.

[42]   C. Lu, C. Y. Tsui, and W. H. Ki, "Vibration energy scavenging system with maximum power tracking for micropower applications," *IEEE Trans. Very Large Scale Integr. Syst.*, vol. 19, no. 11, pp. 2109–2119, 2011, doi: 10.1109/TVLSI.2010.2069574.

[43]   Y. K. Tan and S. K. Panda, "Self-autonomous wireless sensor nodes with wind energy harvesting for remote sensing of wind-driven wildfire spread," *IEEE Trans. Instrum. Meas.*, vol. 60, no. 4, pp. 1367–1377, 2011, doi: 10.1109/TIM.2010.2101311.

[44]   E. J. Carlson, K. Strunz, and B. P. Otis, "A 20 mV input boost converter with efficient digital control for thermoelectric energy harvesting," *IEEE J. Solid-State Circuits*, vol. 45, no. 4, pp. 741–750, 2010, doi: 10.1109/JSSC.2010.2042251.

[45]   H. Kim *et al.*, "An Energy-Efficient Fast Maximum Power Point Tracking Circuit in an 800-µW Photovoltaic Energy Harvester," *IEEE Trans. POWER Electron.*, vol. 28, no. 6, 2013, doi: 10.1109/TPEL.2012.2220983.

[46]   S. H. Chen *et al.*, "A direct AC-DC and DC-DC cross-source energy harvesting circuit with analog iterating-based MPPT technique with 72.5% conversion efficiency and 94.6% tracking efficiency," *IEEE Trans. Power Electron.*, vol. 31, no. 8, pp. 5885–5899, 2016, doi: 10.1109/TPEL.2015.2489922.

[47]   M. Haidar, H. Chible, and D. D. Caviglia, "Noisy reading correction in low power MPPT using kalman filter," 2019, doi: 10.1109/ICECS46596.2019.8964635.

[48]   S. Saravanan and N. R. Babu, "Design and Development of Single Switch High Step-Up DC-DC Converter," *IEEE J. Emerg. Sel. Top. Power Electron.*, vol. 6777, no. c, 2017, doi: 10.1109/JESTPE.2017.2739819.

[49]   E. Chung, K. Lee, Y. Han, and J. Ha, "Single-Switch High-Frequency DC-DC Converter

Using Parasitic Components," vol. 32, no. 5, pp. 3651–3661, 2017, doi: 10.1109/TPEL.2016.2582831.

[50] C.-M. Lai, Y.-H. Cheng, J. Teh, and Y.-C. Lin, "A New Combined Boost Converter with Improved Voltage Gain as a Battery-Powered Front-End Interface for Automotive Audio Amplifiers," *Energies*, vol. 10, no. 8, p. 1128, 2017, doi: 10.3390/en10081128.

[51] J. Divya Navamani, K. Vijayakumar, and R. Jegatheesan, "Non-isolated high gain DC-DC converter by quadratic boost converter and voltage multiplier cell," *Ain Shams Engineering Journal*, 2016.

[52] A. S. Musale and B. T. Deshmukh, "Three level DC-DC boost converter for high conversion ratio," *Int. Conf. Electr. Electron. Optim. Tech. ICEEOT 2016*, pp. 643–647, 2016, doi: 10.1109/ICEEOT.2016.7754759.

[53] K. Kruse, M. Elbo, and Z. Zhang, "GaN-based high efficiency bidirectional DC-DC converter with 10 MHz switching frequency," in *Conference Proceedings - IEEE Applied Power Electronics Conference and Exposition - APEC*, 2017, pp. 273–278, doi: 10.1109/APEC.2017.7930705.

[54] R. W. Erickson and D. Maksimović, *Fundamentals of Power Electronics*. 2001.